# Tracking the severity of naturally developed spalls in rolling element bearings

**Author:**
Zhang, Hengcheng

**Publication Date:**
2021

**DOI:**
https://doi.org/10.26190/unsworks/1601


# Tracking the severity of naturally developed spalls in rolling element bearings

**Hengcheng Zhang**

A thesis in fulfilment of the requirements for the degree of

**Doctor of Philosophy**

School of Mechanical and Manufacturing Engineering

Faculty of Engineering

The University of New South Wales, Australia

October 2021

# Thesis Title and Abstract

**Thesis Title**

Tracking the severity of naturally developed spalls in rolling element bearings

**Thesis Abstract**

Condition monitoring of rolling element bearing is vital for condition-based maintenance (CBM) in many industries. A key obstacle at present is the ability to accurately quantify the severity of the bearing faults, which is commonly measured in terms of the bearing defect size. Limitations of previous studies in the area include: (i) most accelerometer-based approaches were developed for artificial bearing faults instead of naturally developed spalls, and (ii) a systematic comparison between accelerometers and alternative measurements is not available.

Therefore, this thesis aims at obtaining effective methods to estimate and track the growth of bearing spalls. This has been achieved by both advancing the processing of accelerometer signals and exploiting the capabilities of alternative measurements.

Firstly, a novel approach based on accelerometers is proposed, which utilises natural frequency perturbations to estimate spall size. By comparing it with the well-established existing methods, it was found that all methods are effective for artificial spalls, but only the newly proposed approach is successful for naturally developed faults.

Then, three alternative measurements (acoustic emission, instantaneous angular speed, and radial load) are investigated and benchmarked against acceleration on UNSW's bearing test rig. It was found that radial load was far superior in fault-size estimation comparing to all other sensors, and achieved more precise results than accelerometers with less complex processing. This was justified considering radial load as a proxy for radial displacement, whose potential was recently suggested by theoretical studies.

To confirm this, in the last part of this work, actual displacement sensors (proximity probes) were installed on the bearing test rig and a larger gearbox facility. Both experiments demonstrated that the proposed displacement approach can effectively estimate the size of natural spalls, with very limited signal processing required.

This thesis has therefore provided three significant novel contributions to the field of bearing fault severity assessment: (i) the development of a new acceleration-based approach, effective on natural spalls for the first time, (ii) the collection and analysis of a new and comprehensive database of alternative measurements, obtained on naturally developed spalls, (iii) the discovery of the superior effectiveness of direct displacement measurements.

# Originality, Copyright and Authenticity Statement

Thesis Title and Abstract | **Declarations** | Inclusion of Publications Statement | Corrected Thesis and Responses

ORIGINALITY STATEMENT

☑ I hereby declare that this submission is my own work and to the best of my knowledge it contains no materials previously published or written by another person, or substantial proportions of material which have been accepted for the award of any other degree or diploma at UNSW or any other educational institution, except where due acknowledgement is made in the thesis. Any contribution made to the research by others, with whom I have worked at UNSW or elsewhere, is explicitly acknowledged in the thesis. I also declare that the intellectual content of this thesis is the product of my own work, except to the extent that assistance from others in the project's design and conception or in style, presentation and linguistic expression is acknowledged.

COPYRIGHT STATEMENT

☑ I hereby grant the University of New South Wales or its agents a non-exclusive licence to archive and to make available (including to members of the public) my thesis or dissertation in whole or part in the University libraries in all forms of media, now or here after known. I acknowledge that I retain all intellectual property rights which subsist in my thesis or dissertation, such as copyright and patent rights, subject to applicable law. I also retain the right to use all or part of my thesis or dissertation in future works (such as articles or books).

For any substantial portions of copyright material used in this thesis, written permission for use has been obtained, or the copyright material is removed from the final public version of the thesis.

AUTHENTICITY STATEMENT

☑ I certify that the Library deposit digital copy is a direct equivalent of the final officially approved version of my thesis.

# Inclusion of Publication Statement

Thesis Title and Abstract | Declarations | **Inclusion of Publications Statement** | Corrected Thesis and Responses

UNSW is supportive of candidates publishing their research results during their candidature as detailed in the UNSW Thesis Examination Procedure.

Publications can be used in the candidate's thesis in lieu of a Chapter provided:

- The candidate contributed **greater than 50%** of the content in the publication and are the "primary author", i.e. they were responsible primarily for the planning, execution and preparation of the work for publication.
- The candidate has obtained approval to include the publication in their thesis in lieu of a Chapter from their Supervisor and Postgraduate Coordinator.
- The publication is not subject to any obligations or contractual agreements with a third party that would constrain its inclusion in the thesis.

☑ The candidate has declared that **some of the work described in their thesis has been published and has been documented in the relevant Chapters with acknowledgement**.

A short statement on where this work appears in the thesis and how this work is acknowledged within chapter/s:

> The main content of the published paper "Tracking the natural evolution of bearing spall size using cyclic natural frequency perturbations in vibration signals, Mechanical system and signal processing, 151: 107376, 2021", has been incorporated in Chapter 4 of this thesis. The literature review part of this paper has been merged with Section 2.4.1, and the experimental rig setup has been merged within Section 3.4.1.
> The main content of the published paper "A benchmark of measurement approaches to track the natural evolution of spall severity in rolling element bearings, Mechanical system and signal processing, 166: 108466, 2022", has been incorporated in Chapter 5 of this thesis. The literature review part of this paper was merged within Section 2.4.2 and 2.4.3, and the experimental rig setup was merged within Section 3.4.1.
> Permissions are obtained from all the co-authors, and acknowledgements have been made at the beginning of each chapter.

Candidate's Declaration

**I declare that I have complied with the Thesis Examination Procedure.**

# Acknowledgements

First and foremost, I would like to express my sincere gratitude to my supervisor, Dr. Pietro Borghesani. Thank you for providing the opportunity and guiding me through the Ph.D. study in the past three years, which gives me a challenging but fruitful journey in my life. Thank you for your patience and encouragement. I will always remember the time you spent teaching me how to think, code, and write. Thanks for your creativity, enthusiasm, and immense knowledge. I will never finish this thesis without your guidance and instructions. You set up a role model to me. I wish I can be as creative and insightful as you one day.

I would also like to thank my joint supervisor, Prof. Zhongxiao Peng. Thank you for providing me this position in the first place. I am very lucky to join this vibrant and friendly group headed by you. Thank you for your continuous support during my study. Your accurate comments and precious advice helped me a lot.

To Prof. Robert B. Randall, thank you for the tremendous help in our collaborated papers. I look up to you. I hope to be as energized and research active as you at your age.

To Dr. Wade Smith, thank you for the efforts in revising our paper, and the valuable suggestions for research.

To Dr. Md Rifat Shahriar, who was my co-supervisor for half a year. Thanks for the instructions and knowledge sharing.

Thanks to my lab manager, Mr Omear Saeed, for his induction training and help with the test rigs.

I would also like to thank my colleagues in UNSW. Thank you Siyuan Zhuang for the assistance in experiment conduction and data collection. Thank you Dikang, Ke, Peipei, and Jacky for the discussion and knowledge sharing in research. Thank you Hongkun, Yifeng, Haichuan, Runyu, Eric for sharing your happiness and stress.

Thanks to UNSW for offering me the Australian Government Research Training Program Scholarship and providing such a nice environment for research.

I would like to express my deepest gratitude to my parents and parents in law. Thank you for your unconditional support and endless love.

Finally, I want to thank my wife, Yuting Luan. Thank you for the accompany, understanding, and encouragement. I cannot finish this journey without you. I love you.

# Abstract

Condition monitoring of rolling element bearing is vital for condition-based maintenance (CBM) in many industries. A key obstacle at present is the ability to accurately quantify the severity of the bearing faults, which is commonly measured in terms of the bearing defect size. Limitations of previous studies in the area include: (i) most accelerometer-based approaches were developed for artificial bearing faults instead of naturally developed spalls, and (ii) a systematic comparison between accelerometers and alternative measurements is not available.

Therefore, this thesis aims at obtaining effective methods to estimate and track the growth of bearing spalls. This has been achieved by both advancing the processing of accelerometer signals and exploiting the capabilities of alternative measurements.

Firstly, a novel approach based on accelerometers is proposed, which utilises natural frequency perturbations to estimate spall size. By comparing it with the well-established existing methods, it was found that all methods are effective for artificial spalls, but only the newly proposed approach is successful for naturally developed faults.

Then, three alternative measurements (acoustic emission, instantaneous angular speed, and radial load) are investigated and benchmarked against acceleration on UNSW's bearing test rig. It was found that radial load was far superior in fault-size estimation comparing to all other sensors, and achieved more precise results than accelerometers with less complex processing. This was justified considering radial load as a proxy for radial displacement, whose potential was recently suggested by theoretical studies.

To confirm this, in the last part of this work, actual displacement sensors (proximity probes) were installed on the bearing test rig and a larger gearbox facility. Both experiments demonstrated that the proposed displacement approach can effectively estimate the size of natural spalls, with very limited signal processing required.

This thesis has therefore provided three significant novel contributions to the field of bearing fault severity assessment: (i) the development of a new acceleration-based approach, effective on natural spalls for the first time, (ii) the collection and analysis of a new and comprehensive

database of alternative measurements, obtained on naturally developed spalls, (iii) the discovery of the superior effectiveness of direct displacement measurements.

# List of Publications

**Journal papers:**

- *** Hengcheng Zhang**, Pietro Borghesani, Wade A. Smith, Robert B. Randall, Md Rifat Shahriar, Zhongxiao Peng. Tracking the natural evolution of bearing spall size using cyclic natural frequency perturbations in vibration signals, *Mech. Syst. Signal Process.*, 151: 107376, 2021
- *** Hengcheng Zhang**, Pietro Borghesani, Robert B. Randall, Zhongxiao Peng. A benchmark of measurement approaches to track the natural evolution of spall severity in rolling element bearings, *Mech. Syst. Signal Process.*, 166: 108466, 2022

(* Publications included in this thesis)

# Abbreviations

**AE**: Acoustic Emission

**AI**: Artificial Intelligence

**ANN**: Artificial Neural Networks

**BPFI**: Pass Frequency Inner

**BPFO**: ball bass frequency outer

**BSF**: Ball Spin Frequency

**CBM**: Condition-based Monitoring

**CS2**: Second-order Cyclostationary

**DOF**: Degree of Freedom

**DRS**: Discrete Random Separation

**EDM**: Electrical Discharge Machining

**EHL**: Elastohydrodynamic Lubrication

**EMD**: Empirical Mode Decomposition

**FEM**: Finite Element Method

**FTF**: Fundamental Train Frequency

**IAS**: Instantaneous Angular Speed

**MED**: Minimum Entropy Deconvolution

**RCF**: Rolling Contact Fatigue

**REB**: Rolling Element Bearing

**RMS**: Root Mean Square

**RUL**: Remaining Useful Life

**SANC**: Self Adaptive Noise Cancellation

**SE**: Squared Envelope

**SES**: Squared Envelope Spectrum

**STFT**: Short Time Frequency Transform

**TSA**: Time Synchronous Averaging

**TTI**: Time to Impact

**VFD**: Variable Frequency Drive

**WVS**: Wigner-Ville Spectrum

**WVD**: Wigner-Ville Distribution

# List of Tables

# List of Figures

# Table of Contents

# 1. Introduction

## 1.1 Research Background

Rolling element bearings (REB) are the most common mechanical components employed to allow the rotary motion between two machine elements [1]. Despite being manufactured in a wide variety of forms, most REBs have the following key constitutive elements:

1. An inner race, which fits tightly to the shaft
2. An outer race, which fits tightly to the housing
3. Rolling elements (usually a ball or cylindrical/conical element), which facilitate the relative motion between the inner and outer race by rolling
4. A cage to hold the angular space between rolling elements

A failure of an REB almost always results in the seizure of the corresponding shaft and a consequent catastrophic failure of the entire machine. Because of their widespread application in transportation, manufacturing, and energy production, REB failures therefore constitute a significant fraction of severe machines breakdowns, and lead to severe economic and safety losses. For example, it was reported that 25% of machine shutdowns in US Naval aircraft are due to bearing failure [2], up to 44% of failures of large induction motors is caused by bearing faults [3], and about 50 million bearings are replaced every year because they are damaged or fail [4]. To prevent bearing failures and their consequences, a large body of research has been conducted in this area, both regarding their degradation dynamics (failure modes) and their condition monitoring.

As summarized in ISO 15243 [5], the failure of an REB can be caused by many reasons, such as improper design, manufacturing errors, mishandling during transport or mounting, or incorrect maintenance. For a properly designed and operated bearing, the most common

bearing degradation mode is driven by contact fatigue, which forms 1/3 of all failures [4]. Contact fatigue usually manifests itself as a spall on the surface of a race or (more rarely) a roller. The spall grows in size as a consequence of cyclic loading and impacts between rollers and races. As the spall grows, the motion of rollers as they travel through the fault deviates more and more from their original design, and the cage is subject to increased stress to keep rollers aligned and regularly spaced. Eventually, the cyclic stress on the cage results in a cage failure and a seizure of the bearing.

These failure dynamics are unfortunately hidden within the bearing housing, and machine operators and maintainers must rely on condition monitoring technologies for fault detection, fault diagnosis and fault prognosis. Fault detection and diagnosis are respectively aimed at recognising the presence of a bearing fault and identifying its nature (i.e., inner race, outer race or roller fault). Thanks to half a century of research and technical developments, the bearing fault detection and diagnosis problem using vibration analysis have largely been solved, at least for standard applications. Randall provided an authoritative and detailed explanation of developed techniques in his famous book [6]. The next tasks of bearing condition monitoring are fault severity assessment and fault prognosis, whose purpose is to assess the current severity of the fault and how long the component can operate safely. A significant body of work on bearing prognostics only appeared in the last two decades and has so far mostly dealt with the application of statistical and artificial intelligence (AI) methods, applied to traditional vibration indices, already used for detection and diagnostics. Despite a sprawling variety of approaches, there is still no effective and dependable prognostic strategy available to engineers and widely adopted in the industry.

The fact that multiple such methods did not achieve sufficiently convincing results suggests that the main obstacle to prognostics lies in the limitations of the traditional degradation indices rather than statistical/AI methods. This problem is further evidenced by the absence of convincing and widely effective fault severity estimation methods [7]. If available, a robust and monotonic fault severity indicator would greatly reduce the requirements of the following prognostic procedure based on statistics and/or AI.

Such an indicator has two main prerequisites: (i) a sensor technology able to capture quantitative information on the degradation state of the bearing, and (ii) an effective fault-severity assessment procedure capable of extracting such information from the measured data.

In terms of sensors, the bearing condition monitoring research has so far proposed a variety of options for detection and diagnostics, but only a few can be considered for fault severity and prognostics. Some of the proposed approaches, such as those relying on temperature or performance analysis, are only effective in the very last stage of the bearing life, once the fault is so severe that it has an effect on the overall energy flow characterising the system. Other systems, such as oil analysis and ferrography, instead focus on the detection of particles generated by the bearing degradation. Despite effective, these approaches are rarely implemented online and usually require intensive laboratory work to link particles to a specific source (e.g., bearings). Therefore, only a handful of remaining sensor technologies can be considered for widespread, online and automatable prognostics.

Among them, vibration sensors are usually the first to be considered, mostly because of the fact that they are already widely deployed in the industry for detection and diagnostics [6]. The most common vibration sensor employed in industry for the diagnostics of rolling element bearings is the piezoelectric accelerometer, which measures absolute acceleration on the surface of the bearing housing. Another vibration sensor commonly found in industry is the proximity probe, which measures vibration as a relative displacement between the sensor and a target. However, this sensor is almost exclusively used on shafts supported on fluid-film bearings, and it has not been used for rolling-element bearing studies, with the exception of a few cases for model validation [8]. Vibration signals measured on faulty bearings show abnormal signatures specific to the damage type and location, providing reliable diagnostic capabilities. The extent to which vibration-based indices can be effective in prognostics is part of ongoing research.

A sensor technology similar to accelerometers is based on acoustic emission (AE). Like accelerometers, AE sensors are piezoelectric transducers, usually installed at the bearing housing [6]. However, rather than acceleration, they measure solid-borne acoustic signals (stress-waves) generated by the bearing fault and travelling throughout the machine structure.

The use of AE for bearing diagnostics has so far been limited to academic research, and there is yet no evidence of successful implementation of AE-based bearing prognostics.

Another option explored in research work is the measurement of instantaneous angular speed (IAS) of the bearing shaft, which is either measured directly by means of encoders or obtained by processing electric signals coming from generators or motors installed on the shaft. Perturbations of IAS signals reflect torque fluctuations caused by bearing faults. It has been suggested that IAS has the advantage of reducing the influence of the transfer path from the bearing fault to the sensor location, which is known to affect vibration and AE sensors [9].

Vibration, AE, and IAS measurements all result in signals which require processing to extract fault-severity indicators. Among the indicators used in prognostics studies, it is possible to draw two broad classes.

The first and by far most common in literature is composed of traditional detection and diagnostic indices, whose time-evolution is used to capture general bearing degradation trends. The main issues observed in this class are a strong dependency on operating conditions, often non-monotonic trends, and the difficulty to relate them to specific physical properties of the fault. The second class, limited to a very small number of studies on artificial faults, is instead aimed at the direct estimation of the bearing spall size, quantified in terms of length in mm along the race. The handful techniques which have been proposed mostly rely on the spacing between events detected in the measured signals, which are converted into spall-sizes using the known speed of the bearing shaft and the bearing dimensions. They have the advantage of a sound physical relationship with the fault geometry but rely on the identification of low energy events, which are only clear when the spall is artificially designed with sharp edges.

For naturally extended spalls, the entry/exit events are often too weak to be detected, and therefore none of the existing methods can guarantee high levels of effectiveness. Some recent modelling works by Petersen et al. [10], [11] indicated that when a rolling element is in the spalling area, the bearing stiffness will decrease due to the destress of the roller. This novel theoretical perspective on the dynamics of faulty bearings opens a series of new opportunities to develop new approaches using both accelerometers and other sensor technologies.

Regarding the latter in particular, limited work has shown how different sensor technologies and techniques benchmark in terms of severity assessment and prognostics, especially in the case of naturally developing spalls, and there is significant space for further developments in the field.

## 1.2 Research Objectives

The aim of this research is to provide effective and reliable methods to assess fault severity in rolling element bearings. Although many investigations have been conducted in this area, there remain several key research gaps. First, almost all the existing spall size estimation methods are based on artificially seeded defects on the test bearings, there is quite limited empirical research on naturally extended spalls, and no indicators were proved effective on them. Moreover, the few available studies on naturally evolving spalls provide at most a single spall size validation (actual observation) at the end of the run-to-failure test. Finally, the existing researches are mostly based on a single measurement technology (usually accelerometers), and there is no available benchmark of the effectiveness of different sensors in tracking fault-severity in naturally evolving spalls.

To bridge these research gaps, three objectives were identified as follows.

**Objective 1: Extend the use of accelerometers to the estimation of spall size in naturally growing faults.** Existing methods for fault severity estimation were developed based on bearings with artificial spalls, and rely on sharp signal features generated when the roller interacts with the entry and exit edges of the spall. In order to extend the applicability of accelerometers to natural spalls with irregular and smooth profiles, a new technique must be developed able to extract fault symptoms that do not rely on strong entry/exit events.

**Objective 2: Investigate the capabilities of other measurements for fault severity assessment in naturally growing faults.** Most public bearing datasets, such as those by IMS [12] and FEMTO [13], only provide accelerometer measurements. Moreover, they did not collect information on the spall size growth during the run-to-failure process. This study aims at providing a comparison of the effectiveness of different measurements in tracking the evolution of bearing faults. In order to achieve this, it will be necessary to obtain new bearing

run-to-failure data on a test rig equipped with multiple sensors. Moreover, to provide a reference for benchmarking, the faulty bearing will have to be regularly disassembled and inspected.

**Objective 3: Further investigate and refine the most promising approach and related technology.** Once the most suitable measurement is identified on a single test rig, a suitable measurement technology must be identified, able to capture the correct measurements across the most common machine configurations. The proposed approach must be validated on different test rigs.

## 1.3 Thesis Structure

The outline of this thesis is presented in this section. It is organised into nine chapters, among which two published journal papers [14], [15] are incorporated in Chapter 4 and Chapter 5, respectively. The other chapters are unpublished contributions, except that the literature review and experimental description part of the two papers [14], [15] are reproduced in Chapter 2 and Chapter 3. The contents of the following chapters are introduced below.

**Chapter 2**. In this chapter, a systematic literature review on bearing condition monitoring is presented. The literature review has the purpose of providing the necessary background information, in terms of physical, mathematical and signal processing, in order to justify and explain the choices, observations and conclusions of this thesis work. The review begins with a survey of the commonly occurring bearing fault mechanisms, and then covers the modelling of the defective bearing signals, often forming the rationale behind the most popular diagnostic strategies. Then, the three main components of bearing condition monitoring are discussed: detection/diagnostics, severity assessment, and prognostics. Despite the main focus of this thesis being severity assessment, the main literature covering the other two components is also summarised to clarify its links with bearing fault severity assessment.

**Chapter 3**. This chapter outlines the overall research methodology of this thesis. According to the three research objectives set in Section 1.2, the methodology contains three main parts, which briefly introduce the approaches for the developments and results presented in chapters

4, 5, 6, and 7. The experimental setup and test plans of this research are also provided in this section.

**Chapter 4**. A published journal paper titled "Tracking the natural evolution of bearing spall size using cyclic natural frequency perturbations in vibration signals" is presented in this chapter with modifications to fit into the thesis. This chapter mainly addresses Objective 1, proposing a novel accelerometer-based method able to estimate spall size in naturally evolving faults accurately. The method is inspired by a theoretical analysis of modelling studies published recently [11], and relies on the effect of spalls on the bearing's instantaneous stiffness and, subsequently on the natural frequencies of the system. By comparing the newly proposed method to those available in literature, it was found that only the proposed approach is effective on experimental data measured with naturally extended spalls.

**Chapter 5**. A published journal paper titled "A benchmark of measurement approaches to track the natural evolution of spall severity in rolling element bearings" forms the majority of this chapter, with minor modifications and the addition of results at different speeds. The chapter addresses Objective 2, and compares the performance of different measurements (acceleration, displacement, AE, and IAS) on four new bearing run-to-failure tests with naturally evolving faults on the inner and outer race. The estimations obtained with the different measurements are compared to regular inspections of the bearings. It was found that an indirect measure of radial displacement (a load sensor) had the best performance and allowed a reliable and precise estimation of bearing spall sizes, with very limited processing required.

**Chapter 6**. This chapter mainly addresses Objective 3. Given the excellent results obtained with the load sensor, acting as a proxy for radial displacement, the effectiveness of an actual displacement sensor was tested. A proximity probe was installed on two test rigs to directly measure radial displacement. In addition to confirming the results obtained with the floating-housing bearing test-rig of Chapters 4-6, the approach was proved effective on a larger gearbox test-rig, with a more traditional fixed-housing configuration. The chapter also formalised an automated procedure for fault-severity estimation using this sensor technology.

**Chapter 7**. This chapter offers an in-depth discussion of the advantages and shortcomings of the approaches proposed in this thesis.

**Chapter 8**. The conclusion and the key contribution of this thesis are summarised in this chapter, and the potential research directions following this study are indicated.

# 2. Literature Review

This Chapter includes modified excerpts (mostly literature-review parts) from the following papers: part of the paper titled "*Tracking the natural evolution of bearing spall size using cyclic natural frequency perturbations in vibration signals"* is included in section 2.4.1, and part of the paper titled "*A benchmark of measurement approaches to track the natural evolution of spall severity in rolling element bearings"* is included in section 2.4.2 and 2.4.3 [1].

Bearing condition monitoring aims at identifying the current status and predict the future condition of a bearing. Generally, the measured signals firstly go through the diagnostic process to determine whether there is a fault and to what class it belongs. Then fault severity assessment methods are undertaken to estimate the current degradation level. At last, prognostics models are used to predict the bearing failure time or its remaining useful life. A diagram of this process is presented in Fig. 2-1.

This literature review chapter offers a summary of the relevant knowledge accumulated thanks to decades of research in the field and is organised as follows. Section 2.1 provides a review covering the typical bearings failure mechanisms and the nucleation and evolution of the most common degradation mode, namely rolling contact fatigue (RCF). Section 2.2 discusses the most important contributions in terms of modelling such bearing faults, in order to highlight the causal links between faults and their symptoms in diagnostic signals. Section 2.3 briefly summarises the most established vibration-based techniques for diagnostics, nowadays commonly found in industrial applications, and often considered as a starting point for severity assessment. In line with the core objective of this thesis, Section 2.4 focuses on the techniques

[1] Permission has been granted from co-authors.

specific to fault-severity estimation. Finally, Section 2.5 provides an overview of how the results of severity estimation can inform prognostics. This last section deals with a step beyond the objectives of this thesis, but has been nonetheless included to enable to fully represent the value unlocked by high-quality severity assessment.

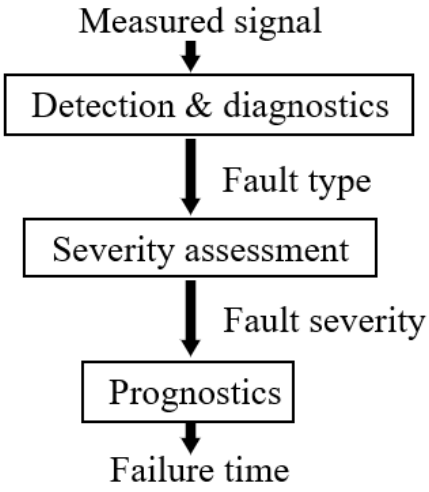


Fig. 2-1. Diagram of bearing condition monitoring

## 2.1 Bearing fault mechanism

The first step for conducting this research of bearing fault severity assessment is to understand the formation and degradation process of these failures. ISO 15243-2017 [5] classified the failure modes of the rolling element bearings based on the visible characteristic appearance on the contact surface as follows:

- Rolling contact fatigue
- Wear
- Corrosion
- Electrical erosion
- Plastic deformation
- Cracking/fracture

Another classification was presented by Neale [16] according to when the final failure occurs, compared to the expected bearing life, computed for instance with the typical L10 index [17]. If the bearing fails very early, then it is more likely to be caused by reasons such as

inappropriate design, faulty installation, overload, or misalignment. If a failure occurs after the initial stage but still before the expected end-of-life, the most likely failure modes include contamination, corrosion, lubrication problems and overheating. Finally, if bearings survive further, they will eventually fail due to material fatigue.

Both references support the concept that rolling contact fatigue (RCF) is the most common reason for bearing failure, and in fact, typical bearing life indices are computed based on this assumption. RCF-induced bearing failures can be divided into two main phases: (i) hidden fatigue accumulation, and (ii) manifest spall growth. A catastrophic and rapid failure follows the last phase, when the spall size is so large that the stress induced on the bearing cage results in its rupture. These two phases will be discussed separately in the following subsections.

### 2.1.1 Hidden fatigue accumulation

This phase can be further classified into two sub-classes based on the origin of the fault: subsurface- and surface-initiated fatigue.

**Subsurface**. According to Hertzian contact theory, the maximum shear stress generated in the race by the cyclic contact with the rollers appears beneath its surface, particularly at a depth of about 0.1 to 0.5 mm. The exact value depends on load, material, cleanliness, microstructure, and operating temperature [18]. As a result, microcracks in a uniform material structure initiate below the surface, as proven by experimental works [19], [20]. After initiation, the microcracks continue to grow in size and branch out. When one branch reaches the surface, a spalling appears in the surface [21].

**Surface.** In actual operation, another possible mechanism for the initiation of a fatigue crack is the unexpected indentation of the race surface. This can happen due to inadequate lubrication, which can lead to plastic deformation of the surface asperities, and thus trigger microcracks and microspalls. Other possible drivers of such a mechanism are hard exogenous particles (contaminants) entering the bearing and directly generating indentations on the surface when trapped between rollers and races. Either way, these unexpected geometric alterations of the surface give rise to a stress-raiser, leading to accelerated fatigue and, ultimately, the formation of a larger spall.

Despite being only the first phase of a bearing's life, hidden fatigue accumulation is often used alone for the definition of bearing life, which is assumed to terminate at the first appearance of a spall [17], [22]. The fatigue model of Lundberg and Palmgren [23] is the most traditional and well-known bearing-life model using this assumption, and formed the basis for a series of works (e.g. [24], [25]) and the ISO standards [17]. For radially loaded bearings, the basic rating life of the bearing associated with 10% chance of failure is given by:

$$L_{10} = \left(\frac{C_r}{P_r}\right)^m \tag{2-1}$$

where $L_{10}$ is in the unit of million revolutions, $C_r$ is the basic dynamic radial load rating, $P_r$ is the dynamic equivalent radial load, and $m$ is the load-life exponent, which is 3 for ball bearings and 10/3 for roller bearings.

It needs to be noted that the basic rating life ($L_{10}$) is developed for the subsurface-initiated fatigue, where bearings are operated under conventional conditions. However, the theory is simply extended to the case of insufficient lubrication or contamination (i.e., possible surface-initiated fatigue) by the inclusion of modification factors [17].

### 2.1.2 Manifest spall growth

The bearing life $L_{10}$ ends at the first appearance of spall, but it does not mean the bearing must be replaced immediately. In the following stage, the cracks continue to spread underneath the contact surface, and the spall grows in size, but reaching a critical size and actual bearing failure requires additional operation cycles. The main purpose of bearing prognostics is to predict the remaining life of a bearing in this phase, and the target of this thesis is to track the spall growth.

Modelling works dominate the literature on the topic of spall growth. An example of bearing spall progression models is that of Kotzalas et al. [26], based on crack-propagation laws derived from the original work of Paris et al. [27]. More complex models (e.g. [28]) use the finite element method (FEM) to evaluate stress distributions on the contact surface and consider elastohydrodynamic lubrication (EHL). Experimental studies are much less common, likely due to the complexity of disassembling and inspecting bearing surfaces as damage progresses. A very interesting example is provided in ref. [29], which studied not only the speed of the

propagation but also found that the spall grows in a V-shape manner from an originally seeded dent.

Similar spall-growth tests were developed within this thesis, and the surface observations were reported in a recently completed Masters' Thesis [30]. Relevant observations will be discussed in the following chapters, along with the analysis of the corresponding diagnostic signals.

## 2.2 Modelling of defective bearings

Known the formation and development mechanism of the localised spalling on the bearing contact surface, the next step is to understand how this defect would manifest in the vibration signal. Modelling or simulation of the defective bearing is an effective tool for this purpose since it can produce signals for bearings with defined defect characteristics on them. Moreover, well-established models are helpful to guide the development of signal processing approaches for bearing condition monitoring, and their output signals can also be used to evaluate the effectiveness of the developed methods.

The models of bearings with localised defects can be divided into two groups: the mathematical models and the dynamic models [31]. The mathematical models see the signals of the defective bearing as a combination of mathematical functions qualitatively representing physical events, for instance the impact signal, the background noise etc. The different mathematical terms are added, multiplied or convolved together to form the desired signal. It is found that the mathematical models are easy to be implemented and they have been valuable tools for justifying diagnostic approaches. This topic will be further discussed in Section 2.3.

Dynamic models instead simulate the bearing as a proper mechanical system with physical elements such as masses, flexible and damping components, etc. Contrarily to what happens in mathematical models, which derive from strong assumptions, physical models are more likely to provide insights on the links between physical phenomena and measured signals, albeit still strongly dependent on approximations and modelling choices. A key advantage of the physical models for severity assessment is the fact that the interaction between spall geometry and rollers is represented in detail, allowing for correspondingly detailed insight on the effect of spall size and shape on measurements.

### 2.2.1 Mathematical models

Most literature regards McFadden and Smith's work [32], [33] as the first mathematical model in this area, which simulated the vibration response of a rolling element bearing with a single point defect on its inner race. In this model, the impacts caused by the point defect are regarded as an infinite series of periodic impulses expressed by the Dirac delta function, which can be modulated by the shaft rotation if the damage is on the inner race. Each impulsive event triggers an impulse response decay, which is convoluted to the pulse-train in the time domain.

Although McFadden's model [32], [33] was presented for bearing with inner race defect, it can be easily modified for outer race and rolling element defective bearings [34]. In addition, this model was adjusted to bearing with multiple point defects on the raceway by adding phase-shifted impact signals [35]. Later Su et al. [36] refined this model by investigating the influence of variable load caused by shaft unbalance and roller errors. These variations were found affective on the amplitude of characteristic frequencies and their side bands.

A key innovation to this model was clearly formulated by Randall et al. [37], who analysed the effects of random fluctuations in the spacing between pulses due to the slip of the rolling elements. The proposed model is reported in the following equation

$$x(t) = \sum_i A_i s(t - iT - \tau_i) + n(t) \tag{2-2}$$

where $s(t)$ is the unit-amplitude oscillating waveform generated by a single impact, $T$ is the average time between impacts, $\tau_i$ is a random time lag due to slip, $A_i$ is the amplitude of the $i$th impact force, and $n(t)$ is background noise. The model was instrumental in showing the second-order cyclostationary nature of bearing signals, which were shown to possess a periodic autocorrelation function. This formed the fundamental theory for decades of developments in cyclostationary signal processing of bearing signals, as will be shown in section 2.3. Further developments and more sophisticated timing models were proposed by Antoni and Randall [38], [39]. The same type of model was also extended to the angular domain to consider variable speed cases [40].

An alternative interpretation of bearing faults was proposed by Behzad et al. [41], which rather than impulsive events, used the concept of rough elastic contact to describe the interaction between raceways and rolling elements. In this model, the rougher surface in the defective area results in a signal portion with higher energy than that corresponding to a non-defective surface. Bastami et al. in [42] adopted this model to investigate the influence of defect sizes on some commonly used statistical features such as RMS and kurtosis, which will be discussed for both detection and severity assessment in sections 2.3 and 2.4.

Yet another family of models, which can be seen as an extension of the pulse-train family, is derived from the experimental observations of Epps and Dowling [43], [44]. In an investigation of experimental bearing signals obtained with slot-like artificial defects, it was found that the ball-passing-spall signal included entry and exit events. The entry was shown to be a low-frequency event, caused by the rolling element entering the spall and rolling over the leading edge in a curved path. The exit event was instead found to be a high-frequency impulse response, resulting from the rolling element impact on the trailing edge of the spall. Based on this observation, models with double impulses were established [45], and spall size estimation methods were constructed by identifying the entry and exit events and measuring the distance between them [45]–[51], which will be further discussed in Section 2.4.

### 2.2.2 Dynamic models

The mathematical models are helpful for understanding the constituent parts of the bearing vibration signal and can effectively imitate the statistical characteristics of the actual signal, but they are not detailed in terms of physical phenomena. Therefore, dynamic models were proposed, which treated the rolling element bearing as a mechanical system with simplified masses, springs, and dampers [8], [10], [11], [52]–[70].

The dynamic behaviour of healthy rolling element bearings are presented in detail by Harris [1], and a dynamic model was built by Gupta accordingly [71]. In their analysis, the REB was disassembled to its constitutional parts: inner race, outer race, cage, and rolling elements, and the interactions between them were described by equations of motions.

Based on the non-defective bearing model, a 2 degree of freedom (DOF) dynamic model of bearing with localised spall on the raceway was developed by Fukata [64], and later it was

extended to a 4 DOF model by Feng et al [65]. In Feng's model [65], the four DOFs are made up of two radial direction motions of the bearing inner race and outer race respectively, and the rolling elements were simplified as springs, ignoring their mass and momentum. Moreover, the slippage of rolling elements relative to the average cage speed and the bearing clearance was also considered in this model. The defective area was regarded as a depth increment on the raceway, and its length could be adjusted to generate corresponding vibration signals.

Sawalhi [52], [70] improved Feng's model by adding a vertical mass-spring component on the outer race to produce the high-frequency resonance. Then Peterson et al. [10], [11], [72] modified it into a 6 DOF model by integrating another horizontal mass-spring system. By investigating this model, it was found that the rolling element would destress in the spalling area, and which led to bearing stiffness reduction in this process. This model is fundamental to understand the physical justifications of the natural-frequency-perturbation method for fault severity assessment developed in this thesis and discussed in Section 4.

Further improvements were undertaken by the following studies. The waviness of the raceway surface and EHL were simulated in Sopanen's 6 DOF model [66]. The mass of the rolling elements was considered in Harsha's model [73], and the finite sizes of the rolling elements were also taken into account in Moazen Ahmadi's model [59], which produced a signal more realistic when compared to experimental data. Inertial and centrifugal effects of rolling elements were considered in Nakhaeiejad's model [55], and a model of bearing with multiple line spalls on the raceway was presented by Patel et al. [54]. The importance of applied load and defect-edge angle were addressed in the modelling work by Larizza et al. [60], [61].

The above-mentioned dynamic models are all lumped parameter models or multi-body dynamic models, which means that several assumptions and simplifications such as rigid connections and point masses are used in their construction. The FEM method can effectively minimize these simplifications. FEM models [74]–[76] are mostly built-in commercial software packages such as ANSYS, Abaqus and I-DEAS. The advantage is that they are regarded as more accurate, while the main disadvantage is that they are much more complicated and harder to be constructed.

Having these dynamic models, the next step is to integrate them into machines with other parts, such as rotor, pedestal, and gears, thus more realistic vibration signals of the mechanical system could be generated. One example was given by [77].

Overall, the models reviewed in this section represented how researchers recognise the vibration signals produced by defective bearings. These different recognitions guided the development of different fault severity estimation methods in Section 2.4.

## 2.3 Bearing fault detection and diagnostics

Before investigating the fault severity of rolling element bearings, fault detection and diagnostics are first introduced. It is important to highlight that this topic is outside the main scope of this thesis, and as such, this review will be brief and by no means exhaustive. Nonetheless, it was deemed relevant to report a brief overview of a few typical diagnostics approaches for three reasons. Firstly, the detection of a fault and its diagnostics are natural precursors of severity assessment and should be used to trigger it. Secondly, it is important to understand the different aims of these two complementary steps in condition monitoring, and explore the possibility and past attempts to integrate the two or use similar indices for both aims. Finally, the two steps share a series of common signal processing tools.

**RMS**. The most traditional criterion for machine fault detection using vibration signals is the root-mean-square (RMS). ISO 10816 [78] is based mainly on this index and defines condition thresholds for different machines according to their types and sizes. Machines exceeding certain thresholds are thus identified as faulty. The rationale for the use of RMS, an energy measure, is that a fault would produce unwanted components in the signal, which would increase its overall energy. This conceptually applies to bearings as well, and both pulse-train and rough-elastic-contact models can be used to justify an increase in RMS. Many studies investigate RMS as a detection feature [79]–[85], even if it is widely accepted that RMS alone carries little diagnostic information, and faulty bearings are only one of the possible causes of an increase in energy in the signal.

**Kurtosis**. Referring to the models described in Section 2.2 again, a bearing fault is also expected to increase the impulsiveness of the signal, either because of the impacts

characterising the pulse-train-model or the irregular rolling in the rough-elastic-contact model. A robust and widely used indicator is kurtosis, which is defined as the normalized fourth central moment of the signal. Larger kurtosis indicates more impulsive signals, i.e. signals with a distribution characterised by fat tails (outliers). Kurtosis is more sensitive than RMS at the beginning of the defect formation due to the fact that the impacts caused by small spalls are often low in energy but can still affect the impulsiveness of the signal [86]–[91]. Recent developments [89] have however shown that the success of kurtosis in bearing fault detection could also be explained by its sensitivity to cyclostationarity rather than impulsiveness. Yet, kurtosis, like RMS, is hardly a good diagnostic feature, since it is affected by a variety of vibration sources.

**Cyclostationarity and envelope.** Since the repetitive impacts on the bearing defect excite high-frequency resonances, the defective bearing signal can be regarded as being amplitude modulated in a high-frequency range. Therefore, envelope analysis is probably the most commonly used tools for detecting this signal. The usual procedure for envelope analysis includes: band pass filtering the signal (usually retaining a relatively high-frequency band); applying a Hilbert transform to extract instantaneous amplitude and phase of the signal (represented as a complex quantity); and then analysing the spectrum of the squared value of the amplitude only [33]. As discussed in the pulse-train-modelling literature review of Section 2.2, another interpretation of the bearing signal is that it is second order cyclostationary (CS2), and therefore characterised by periodic second order statistics (variance, autocorrelation and autocovariance). In recent years, more complex cyclostationary indicators have attracted more interest, including bi-spectral quantities such as the spectral-correlation-density and time-frequency indicators such as the Wigner-Ville Spectrum [92], [93].

These three categories are by no means covering the large literature exhaustively on this subject, and do not mention indicators considering more than one of those signal features, examples of which are available in the following references [94]–[96], yet beyond the scope of this thesis.

As an example of many effective bearing diagnostics methods developed in the past few decades [88], [97]–[108], the semi-automatic procedure provided in [103] is adopted here to explain the general organisation of the bearing diagnosis process, which will also be used as a

starting point in subsequent parts of this thesis dealing with severity assessment. Most approaches contain three steps: order tracking, signal enhancement, and envelope analysis, as shown in Fig. 2-2. The last step can be followed or substituted by the calculation of a single index aimed at detecting one or more properties of a faulty-bearing signal, examples of which are available in many of the references cited in this section.

1) **Order tracking** – Remove speed fluctuation
2) **Signal enhancement** – Remove unrelated part and enhance the fault related signal
3) **Envelope analysis** – Determine fault characteristic frequencies

Fig. 2-2. General procedure for bearing diagnostics

Order tracking is used in many applications for both bearing diagnostics and prognostics, since it removes the speed fluctuation from the measured vibration signal. The main concept of order tracking is to transform a signal sampled at regular time intervals into a signal sampled at regular angular intervals [109], [110]. An angle-time map is obtained from a tacho or (preferably) encoder signal, providing a higher number of reference pulses per shaft revolution. Otherwise, it can be extracted from shaft harmonics in the vibration signal itself, most commonly from strong gear mesh harmonics [111]. For bearing diagnostics, order tracking was reported effective to correct speed fluctuations and even large speed transients [104].

The correction of speed fluctuations is not the only advantage of order tracking. Order tracking is often a prerequisite for the removal of strong masking components. Since bearing signals are often weak compared to those of other components such as gears, enhancement of the bearing related signal component is often implemented as a second step. Time synchronous averaging (TSA) [112] is the most common method, which allows to remove all shaft harmonics if the signal has been order-tracked. Other options are available, for instance linear prediction [113], self-adaptive noise cancellation (SANC) [97], and discrete random separation (DRS) [101]. After removing the deterministic part, the bearing signal may still be masked by other non-deterministic sources. The simplest and probably most common signal enhancement methods

used to address this issue are a series of optimal-demodulation-band selection techniques. As discussed before, the envelope spectrum is usually obtained after band-pass filtering the signal retaining a band where the bearing signal components are dominant. The selection of such a band can be driven by different criteria, often referring to the properties of the models seen in Section 2.2.1. Since the defect-related signals are impulse responses, one option is to select the band with the highest kurtosis (Kurtogram [98], [114], [115] and Fast Kurtogram [108]). Other options include the Protrugram [116] and a series of methods reviewed in [117]. Alternative filtering approaches, based on more complex and adaptive filters, rather than candidate bands, were proposed, the most common probably being the minimum entropy deconvolution (MED) [102].

The last step of the procedure is the envelope analysis, used to obtain the squared envelop spectrum (SES). Specific frequency components: ball pass frequency inner (BPFI), ball bass frequency outer (BPFO), ball spin frequency (BSF), and fundamental train frequency (FTF) are searched for in the SES to identify a bearing fault.

## 2.4 Bearing fault severity assessment methods

Spalling or other defects on the bearing are expected to introduce abnormal fault signatures in bearing signals. The essence of fault severity assessment is to extract these fault signatures and build indicators to reflect the degradation level of the bearing.

Spall-symptomatic signatures are different for different sensors, and hence the corresponding signal processing and feature extraction methods are not the same. State-of-the-art techniques for different signals are reviewed respectively in the remaining part of this section.

### 2.4.1 Vibration based

Vibration analysis by means of accelerometers is the most common and widely applied condition monitoring technique. The different techniques for severity estimation can be classified as either based on diagnostic or physical indicators.

**Diagnostic indicators**. The most common diagnostic indicators have already been discussed in Section 2.3 for detection and diagnostics. Their use in fault severity assessment and prognostics is quite widespread, but has not yet provided widely established results. Most

diagnostic indicators used in tracking fault severity can be classified into the three large classes already discussed in the previous section: 1) energy, 2) impulsiveness, and 3) cyclostationarity. Review papers [7], [118]–[120] summarised the usage of these indicators for trending the bearing degradation level and prognostics. Some researchers used a single indicator to track the bearing fault severity, while others combined several ones to increase the robustness, monotonicity, and trendability [3], [81], [82], [94], [118], [121]–[148]. For example, the performance of some commonly used indicators (e.g. RMS, kurtosis, skewness, crest factor, amplitude of bearing spectral components) were compared in [130], [135], [138], [143], [147], and these typical indicators were fused to better predict the residual life using different methods, such as neural networks in [121], [125], Gaussian mixture model in [126], and support vector machine in [129], [131].

**Physical indicators.** Physical indicators were developed based on observations on experimental signals and/or in accordance with defective bearing signal models as those presented in Section 2.2. Based on Epps' observations and related models (see Section 2.2.1), Sawalhi and Randall [45] proposed identifying and using the roller's entry/exit events to estimate the size of the spall. The interval between the two events, named Time to Impact (TTI), was identified with the following procedure. The linear prediction was used to remove the deterministic part of the signal (such as gear components) so that the entry and exit events become more pronounced. Then, pre-whitening by an autoregressive (AR) model was performed to increase the energy of the entry event relative to the impact, which is usually much stronger in the raw signal. A filter bank based on complex Morlet wavelets [98] is then used to split the signal in candidate bands, among which the optimal is selected manually as that which enhances the two events. Finally, the squared envelope is obtained and subject to a further step of MED filtering to sharpen the entry/exit events, essentially giving two clear pulses whose separation in time gives the TTI. The estimated spall size corresponds to double the TTI, assuming that the spall is small enough for the rolling element to bridge across it, contacting the leading and trailing edges simultaneously (first equation in Table 2-1).

Sawalhi and Randall's method (hereafter referred to as Sawalhi's method for brevity) is illustrated in Fig. 2-3, where it was implemented on a bearing with a 1.6 mm notch on the outer

race [149] (the same data is used in Section 4.3 of this thesis and labelled as "Test 1"). Because of the clear edges of the notch and the high signal-to-noise ratio of the experimental data, the entry and impact events are already quite clear in the raw vibration signal, as shown in Fig. 2-3 (a). The processed results after pre-whitening (the cepstrum pre-whitening technique [150] was used in this case) and filtering based on complex Morlet wavelets are shown in Fig. 2-3 (b) and (c). Finally, the entry and impact events are revealed as two peaks in the squared envelope signal as shown in Fig. 2-3 (d).

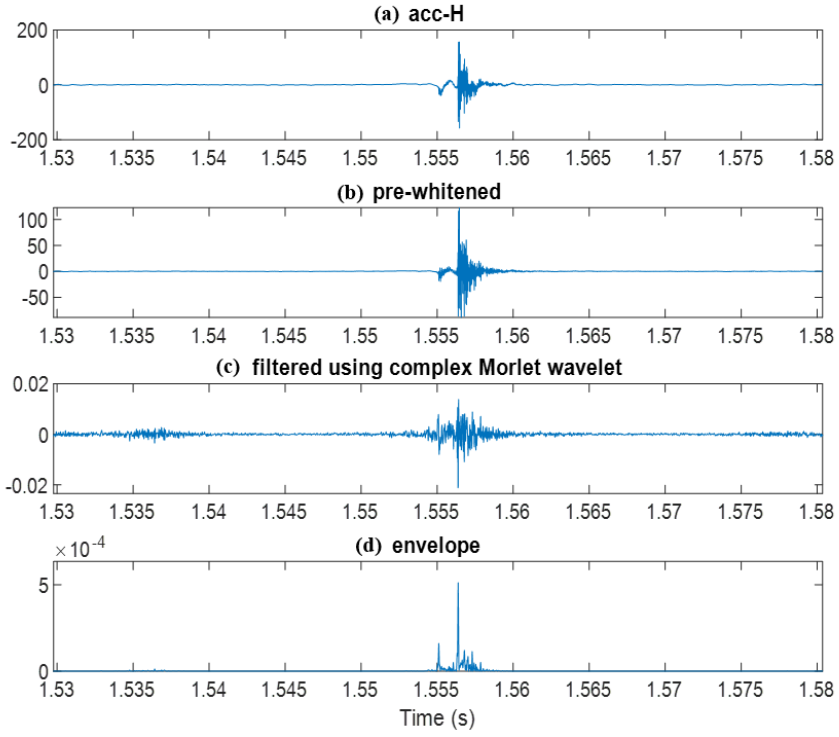


Fig. 2-3. Process of Sawalhi's method applied on bearing with notch defect: (a) raw signal, (b) pre-whitened signal, (c) filtered using complex Morlet wavelet, (d) squared envelope signal

Two limitations of Sawalhi's method were pointed out by Smith et al. in [149]: one is that the low-frequency entry event is not always prominent, and is very likely to be masked by noise or other signals, and the second is that the size estimation results were found by experiment to be speed dependent. To overcome these two limitations, Smith et al. suggested recognising the entry event not as a low-frequency step effect, but a steep roll-off which was supposed to be caused by the rapid unloading of the roller. Based on this understanding, two ways were

proposed to identify the roll-off. The first one is to find the peak point of the low-pass filtered acceleration signal, and the second one is to identify the zero-crossing point of the gradient function of the low-pass filtered acceleration signal. Smith et al. also suggested the use of envelope analysis to recognise impacts, and they built 'event windows' as a visual tool to study the rolling element/spall interaction in more detail. These windows were built by using impacts as centre points and half of the fault pass period as the window length. The average value of the entry-impact time differences from many, usually hundreds of, rolling element/spall interaction events were used to calculate the spall size.

The implementation of Smith's method on the same data is shown in Fig. 2-4. The black line is the collected acceleration signal, and the red dotted line is the impact point captured from the impulse response identified in the squared envelope signal of the high pass filtered (cut-off frequency of 10 kHz in this case) acceleration. The green dotted line is the theoretical entry point calculated from the impact point and the (known) spall size, and the blue line is the gradient signal of the low pass filtered (cut-off frequency of 1500 Hz in this case) acceleration. The gradient function is only applied on the signal before the impact point, while its value after that is set to zero. The roll-off effect can be identified by its first decrease to another user-set threshold, which is about -30 units in this figure, and the zero-crossing point before the roll-off is the estimated entry point. Thus, the TTI is determined, and the spall size can be calculated accordingly.

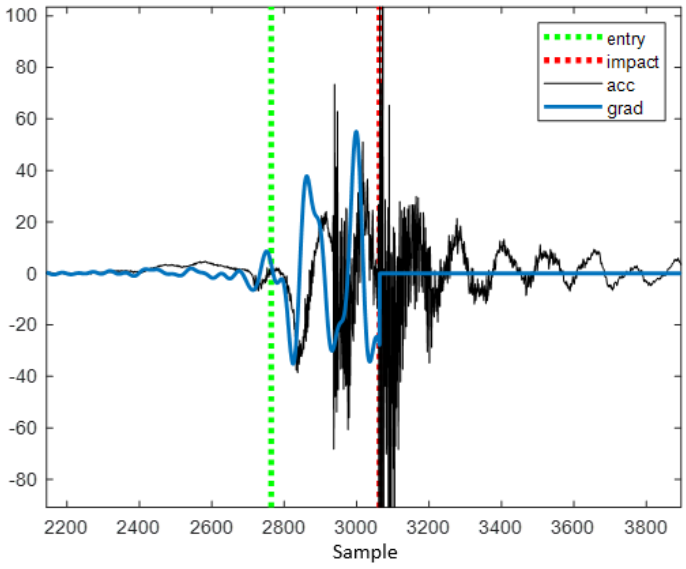


Fig. 2-4. Spall size estimation of Smith's method applied on bearing with notch defect

Moazen Ahmadi et al. expressed a similar yet slightly different understanding of the rolling element's defect passing process [8]. By using a proximity probe together with an accelerometer signal to reveal the relationship between the relative displacement of inner/outer raceways and the corresponding vibration responses, it was reported in [8] that the whole process contains a low-frequency entry event, a high-frequency impact and a low-frequency exit event which partly overlaps with the previous high-frequency impact event. Based on this understanding, they suggested the use of pre-whitening, low pass filtration and envelope analysis to determine the time span between the low-frequency entry and exit events. It was also reported that the de-stressing process before the entry and re-stressing process after the exit point should also be accounted for when calculating the total spall size.

As for the previous two methods, this approach (later referred to as Moazen's method) has been implemented on the same data, as illustrated in Fig. 2-5, which clearly shows that the main difference with this method is that the low-frequency exit event is utilised to estimate the spall size instead of the high-frequency impact event. As seen from Fig. 2-5 (a), the exit event is masked by the high-frequency impact event and is hard to detect from the raw vibration signal, while after low-pass filtering (cut-off frequency of 1500 Hz in this case) and envelope analysis, it is clearly revealed. It should be noted that the interval between entry and exit events is

correlated to the full spall size, rather than half the size as with the TTI in the previous two methods.

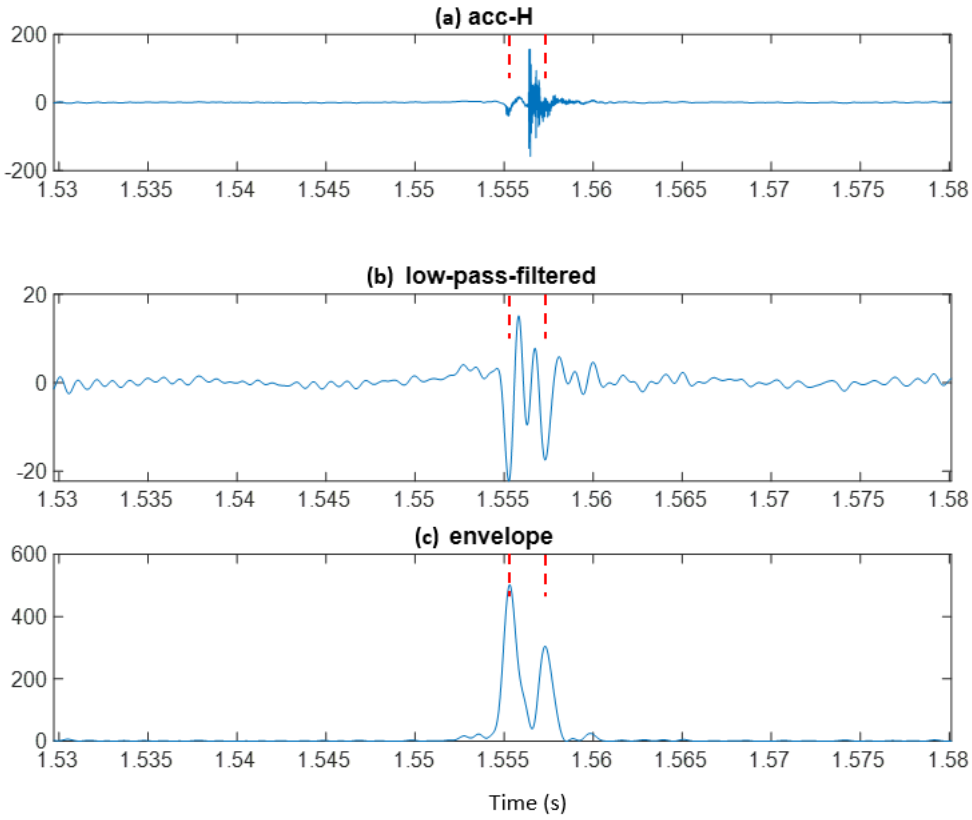


Fig. 2-5. Spall size estimation of Moazen's method applied on bearing with notch defect

In summary, the spall size estimation process, as described in the above-mentioned methods, can be divided into four major components, as illustrated in Fig. 2-6. In the first step, each approach applies a suitable pre-processing method according to the considered hypothetical model of the roller-passing-spall signal. This commonly includes processing of the raw acceleration signal to remove the periodic components and enhance the spall excited signatures, which is like the order tracking and signal enhancement steps in bearing diagnosis. The enhanced signal is further processed for clear identification of the entry and exit points, and the entry-exit time separation (or time to impact in some cases) is determined. In the final step, the spall size is calculated based on the bearing dimensions, running conditions and the previously determined spall passage time. In Fig. 2-6, the white arrows pointing from the model box to

the three signal processing steps represent the unique understanding of roller-passing-spall signal in different methods, while the black arrows indicate the transfer of the unprocessed or processed signal.

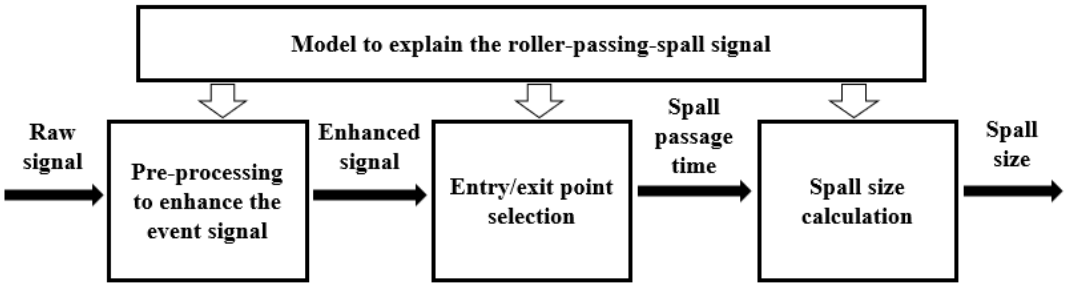


Fig. 2-6. Physical spall size estimation procedure for REBs. (White arrows represent guidelines for signal processing steps, and black arrows indicate data transfer.)

Table 2-1 provides a summary of the existing spall-size estimation approaches. Most of the approaches demonstrate their novelties in the improvement of one or more of the above-mentioned four components: roller-passing-spall model [8], [151], [152], pre-processing [46], [56], [153], entry/exit point selection [47], [149], [154], and spall size calculation [48], [155]. For example, several methods have been developed to enhance the weak entry event signature. Chen et al. [46] proposed the use of Variational Mode Decomposition (VMD) at first to separate the entry/exit events, and then the use of cross-correlation to find their time separation more accurately. A similar approach was suggested by Zhao et al. [56], who used Empirical Mode Decomposition (EMD) to separate the entry and exit events, and then Approximate Entropy (ApEn) to increase the precision of selection. Cepstrum editing as a pre-processing technique was proposed by Sawalhi et al. in [153] for the same purpose.

For the entry/exit point selection, most methods used the peaks of envelope signals, while Ismail et al. [154], [156] suggested using peaks of the jerk signal, which was calculated using limited bandwidth Savitzky-Golay differentiators (LBSGD). Cui et al. [47] used the matching pursuit method to locate entry/exit points by creating a step-impulse dictionary.

The size calculation is directly related to the descriptive model of the spall excited signal. More precise and detailed analytical models have been reported recently to improve the accuracy of the size calculation algorithm. Relevant works can be found in [151], [48], [152], [157].

Given that only physical indicators provide a direct quantitative assessment of spall size, they will be in general considered in the rest of this thesis the 'state of the art' in terms of bearing fault severity assessment. Diagnostic indices will be also considered in Chapter 5, but have the obvious drawback of relying on a scale factor to be determined using data-driven methods (training), which is often not possible in many real-life scenarios.

Table 2-1. Existing spall size estimation methods for REBs

| **Literature** | **Size range (mm)** | **Model to explain the spall excited events** | **Pre-processing method to enhance the event signal** | **Entry/exit time point selection** | **Size calculation** |
|---|---|---|---|---|---|
| Sawalhi [45] | 0.6, 1.2 | Low frequency entry; High frequency impact | Pre-whitening (AR) Filtered (Wavelet filter bank) MED | Max envelope Cepstrum | $l = \frac{\pi f_r (D_p^2 - d^2)}{D_p} t_{imp}$ |
| Zhao [56] | 0.6, 2.4 | Low frequency entry; High frequency impact | Empirical mode decomposition (EMD) Approximate entropy (ApEn) | Max envelope | $l = \frac{\pi f_r (D_p^2 - d^2)}{D_p} t_{imp}$ |
| Cui [47] | 0.6, 1.2 | Low frequency entry; High frequency impact | Not addressed | Matching pursuit | $l = \frac{\pi f_r (D_p^2 - d^2)}{D_p} t_{imp}$ |

| | | | | | |
|---|---|---|---|---|---|
| Smith [149] | 1.6 | Steep roll off after entry; High frequency impact | No need because of high SNR of experiment data | Impact: Trigger for squared envelope Entry: Low pass filtered gradient zero crossing | $l = \frac{\pi f_r (D_p^2 - d^2)}{D_p} t_{imp}$ |
| Moazen [8] [51] | 1.48 – 3.11 | Low frequency entry; High frequency impact; Low frequency exit | Pre-whitening Low pass filter | Max envelope | $l = \frac{D_p + d}{2} \sin(2\beta_2 + \beta_1)$ |
| Ismail [156] [154] | 2.6 – 6.8 | Low frequency entry; High frequency impact | Limited bandwidth Savitzky-Golay differentiator | Max of jerk (differentiation) | $l = \frac{\pi f_r (D_p^2 - d^2)}{2D_p} t_{exit}$ |
| Kogan [152] [157] | 0.39 – 2.61 | Low frequency entry; High frequency impact; Rattling after impact | Entry: Band pass filter Impact: high pass filter | Max of acc | $l = l_{dis} + l_{imp} + l_{TE}$ |
| Chen [151] [46] | 0.8 – 1.5 | A: Start of destressing; B: End of destressing; C: start of restressing | Variational mode decomposition (VMD) | A: Minimum acc after empirical model B: Max of cross correlation C: Threshold for impact | $l = (D_p + d) sin \frac{\phi_{spall}}{2}$ |

| | | | | | |
|---|---|---|---|---|---|
| Luo [48] | 0.81 – 1.54 | Low frequency entry; High frequency impact; Refined entry and exit stage | Pre-whitening (AR) | Not addressed | $l = \frac{\sqrt{2(1-cos\phi_{spall})}}{2}(D_p + d)$ |
| Wang [155] [153] | 4.2 – 6.2 | Low frequency entry; High frequency impact; | Synchronous averaging; Cepstrum editing | Max envelope | $l = \frac{\pi f_r (D_p^2 - d^2)}{D_p} t_{imp} + \zeta$ |

Displacement is also a form of vibration and could be detected by sensors such as proximity probes, however it is usually used for journal bearings rather than REBs. Moazen Ahmadi et al. [8] utilized an eddy current proximity probe to detect the relative displacement between inner and outer races of a ball bearing with an artificial notch seeded on its outer race, and it was found that the relative displacement is related to the spall size. and the entry and exit points of the spalling zone could be seen clearly from the signal. It will be seen in Section 4.1 that these observations on artificial spall geometries were confirmed for the first time in our experiments for naturally evolving spalls.

### 2.4.2 Acoustic emission based

Acoustic emission (AE) sensors measure the solid-borne transient elastic waves caused by the rapid release of localised stress energy, such as from crack growth and friction. In recent years, AE has received more attention on its application to bearing diagnostics and prognostics, as it is believed to be more sensitive to incipient defects and surface roughness change [158]. The main difference between AE and vibration signals is that the frequency range of the former is typically 100 kHz to 1 MHz, which is much higher than the vibration signal. Other than that, the signal processing techniques usually implemented are similar.

As for vibration signals, the bearing severity studies using AE signals can be categorised as spall duration estimation and fault degradation estimation, although their number is much smaller. In [159]–[161], Mba and Elforjani et al. suggested that the size of spall on the bearing raceway could be estimated by the duration of the individual corresponding AE bursts. In [87], [162], [163], it is proposed that AE also has double spikes caused by entry and exit events, just like vibration signals. Time domain indicators, such as RMS, kurtosis etc. were tested by Al-Ghamd et al. in [164], and it was concluded that these indicators were sensitive to both the length and the width of the defect area on the raceway of a roller bearing. Frequency domain analyses, for example of the Squared Envelope (SE), were also applied by Ming et al. [165]. Caesarendra et al. [166] provided a review paper on the AE based bearing condition monitoring methods.

### 2.4.3 Instantaneous angular speed based

The instantaneous angular speed (IAS) variation of the shaft is due to the torque fluctuation, and bearing faults can be one of its causes. IAS is expected to overcome the influence of the transfer paths from the defects to the vibration and AE sensors [9]. Therefore, IAS has attracted more and more interest recently for its application to bearing fault severity analysis. The calculation methods of IAS were reviewed by Li et al. in [167] with the elapsed time method. Feldman [168] suggested deriving the instantaneous frequency from the analytic signal as shown in Eq. (2-3), where $x_a(t)$ is the analytic signal obtained by bandpass filtering the encoder signal around its first shaft speed harmonic. This approach was thought to be the most accurate [169], and is therefore adopted in this research.

$$\omega(t) = \mathrm{Im}\left[\frac{\dot{x}_a(t)}{x_a(t)}\right] \tag{2-3}$$

In order to estimate spall size, Bourdon et al. [170], [171] suggested to narrow bandpass filter the signal by its first few harmonics of ball pass frequency, and then observe the duration of filtered IAS fluctuation. Moustafa et al. adopted a similar approach in [9], and this technique was further supported by the work of Gomez et al. which validated it on a dynamic model [172]. Renaudin et al. [173] also observed that the amplitude of BPFO harmonics increased as the spall grew larger, and that hence they can be used as fault severity trending indicators. The IAS

was thought to be able to detect spalls earlier than vibration since it is less dependent on the transfer path and on the noise generated by other mechanical components [9].

Since IAS is coupled with the shaft torque, the current and voltage can also reflect its change. Some researches [174], [175] suggested that the bearing defect would affect the side-bands of the electric supply frequency in the spectrum, and severity indicators could be based on that.

## 2.5 Bearing prognostics

Bearing prognostic is beyond the topic of this thesis, but it is still reviewed here to present the value of dependable fault severity assessment. The key point of prognostics is to build models to predict the fault progression speed and construct the relationship between the current status and the remaining useful life (RUL) of the bearing. The prognostics models can be separated into two groups: the physics-based model and the data-driven model [176], [177], and they both rely on high-quality fault severity indicators.

### 2.5.1 Physics-based models

Paris' law is the most widely used physical crack growth model in bearing prognostic studies [178]–[180]. It built a relationship between crack length and the life of material. It has the formula [27]:

$$\frac{dL}{dN} = C_0(\Delta k)^n \tag{2-4}$$

Where $L$ is the crack length, $N$ is the number of cycles of load applied, $\Delta k$ is the stress intensity factor (SIF), while $C_0$ and $n$ are coefficients depending on the material.

If a threshold number of load cycles is defined as $N_{thr}$, then the RUL could be calculated as:

$$N_{RUL} = N_{thr} - N_i = \int_{L_i}^{L_{thr}} \frac{dL}{C_0(\Delta K)^n} \tag{2-5}$$

Where $N_i$, $L_i$ are the current cycle number and crack length, $L_{thr}$ is the threshold crack length. The SIF in [181] is estimated as:

$$\Delta K = \tau_{max}\sqrt{\pi L}Y \tag{2-6}$$

Where $\tau_{max}$ is maximum shear stress, and Y is the geometric correction factor related to the shape of crack.

Put SIF in and take all the constant out as D then:

$$N_{RUL} = D \int_{L_i}^{L_{thr}} \frac{dL}{L} \tag{2-7}$$

Constant $n$ is 2 for REB material. Thus:

$$D = \frac{1}{C_0 \tau_{max}^2 Y^2 \pi} \tag{2-8}$$

And

$$N_{RUL} = D \int_{L_i}^{L_{thr}} \frac{dL}{L} = D ln \frac{L_{thr}}{L_i} \tag{2-9}$$

Now the task has changed to finding the parameter $D$ and the threshold crack length. Normally, $D$ is estimated by history data. In [181], the bearing degradation process is divided into two stages: the slow, stable degradation and the fast, unstable degradation, which means the parameter $D$ for each stage are different. If the crack extension speed (spall propagation rate) is known, the parameter $D$ can be derived accordingly.

### 2.5.2 Data-driven models

Instead of trying to understand the degradation process and explain the system physically, the data-driven methods attempt to find a pattern from the historical data and utilize it in predicting future events. In the past, this used to be done by simple trending strategies such as exponential smoothing or autoregressive modelling [120], [182], which however proved highly susceptible to the stability (e.g. monotonicity) of the chosen severity indicator.

In recent years, artificial intelligence (AI) methods have attracted the interest of researchers in this area. AI is known to be able to recognize complex, non-linear relationships between several parameters, and researchers attempted to use this capability in tracking the bearing degradation state or predicting its remaining useful life. The most common approach is to feed a series of diagnostic indices to artificial neural networks (ANN) ([148], [183]–[185]). Given a training

set of bearing signals with a known condition, the complex and non-linear network structure automatically learns the relationship between input (indices) and output (fault state or RUL). The benefit of this kind of AI method is that it does not require complex signal processing methods, but its obvious limitation is that it requires large amounts of training faulty-bearing data, which needs to be specific to each machine, cover multiple operating conditions and is often difficult to obtain in normal industrial settings.

In addition to this data requirement, a prerequisite for these networks to provide acceptable results is that the fault-severity information is actually present in the features used as input for the network itself. In other words, they require good severity-assessment pre-processing of the data.

Aside from ANN, there are other AI techniques applied for bearing prognostics. Examples include: the Bayesian networks [186], the support vector machine (SVM) method [187], Hidden Markov models (HMM) [188] and deep learning [189]. The latter has shown particular interest, as it promises to extract information from the raw diagnostic signal as an input, seemingly bypassing the severity-assessment step [190]. Despite true in principle, the complexity of such AI methods results in them being even more data-greedy, and therefore often not applicable.

# 3. Methodology

As indicated in Section 1, this research project aims to develop effective and reliable methods to assess fault severity in rolling element bearings. A list of sensors is available for bearing condition monitoring: accelerometers, acoustic emission sensors, encoders, displacement sensors, etc.

Among them, accelerometers are the most widely used for bearing fault detection as well as severity assessment. Therefore, the first objective of this thesis is to fully exploit the potential of this measurement technology and overcome its issues in the tracking of naturally evolving spalls. The novel acceleration-based method should overcome the limitation of existing methods mostly developed for artificially manufactured defects. An introduction of this approach is presented in Section 3.1, and the full procedure and findings are discussed in detail in Chapter 4.

After having dealt with accelerometers, the second sub-objective of the thesis is the investigation of alternative measurement options for tracking naturally evolving spalls. The main methodological plan of this work is introduced in Section 3.2, while detailed results and a thorough discussion on their performance are compared in Chapter 5.

The comparison study of Chapter 5 found that an indirect measurement of relative radial displacement between bearing inner and outer race gave the best result of spall size tracking. Therefore, in the last part of this thesis work, a further study was undertaken for the analysis of a more direct relative displacement sensor: proximity probes. The analysis of its effectiveness was also extended to a more complex and common machine configuration, with additional experimental tests on a gearbox test rig. This part of the work is briefly introduced in Section 3.3 and thoroughly discussed in Chapter 6

In order to support all these findings, a significant set of measurement campaigns were conducted at UNSW in the years 2018-2020. The experimental setups and the test plans are discussed in Section 3.4.

Before entering into the specifics of each objective and related methodology, it should be noted that all new developments were based on the physical understanding of the effect of bearing faults on measured signals, which are described by models reviewed in Section 2.2.

Firstly, the interpretation of the dynamic modelling provided by the group of University of Adelaide [10], [11] was an important resource in developing the natural-frequency-perturbation method for accelerometer-based severity assessment of Chapter 5. In particular, the observation that bearing stiffness decreases when the rolling element falls into the spalling area led to the idea of using stiffness-variation-induced natural frequency perturbation to estimate the spall size.

Similarly, a variable-stiffness bearing was behind the interpretation of the load measurements in Chapter 6, which were therefore recognised as a proxy for relative displacement between inner and out race [8]. This physical interpretation was extended to all other sensors. AE was deemed sensitive to the surface roughness change of the contact surface [158], hence the burst duration was supposed to be correlated with the length of the rougher spall area. For angular speed, a bearing spall is expected to generate torque disturbance, which in turn would trigger speed fluctuation or torsional vibration of the shaft [191].

The relationships between measurement approaches, physical interpretation and models, and the methodologies implemented and tested in this thesis are summarised in Table 3-1.

Table 3-1. Methodologies for measurement approaches based on their models

| Measurement | Physical interpretation | Methodology |
|---|---|---|
| **Acceleration** | Stiffness of bearing decreases when rolling elements fall into the spall | Time-frequency analysis to measure the duration of natural frequency perturbation |
| **AE** | AE is sensitive to the roughness change of contact surface | Measure the AE burst duration |
| **IAS** | Spall induces speed fluctuation of the shaft | Measure amplitude of defect frequencies |
| **Displacement** | Relative deflection of inner-outer races changes when rolling elements fall into the spall | Measure the duration of displacement perturbation |

## 3.1 Acceleration-based spall size estimation approach (Objective 1)

The first objective of this study is to propose novel reliable acceleration-based bearing fault severity indicators. As reviewed in Section 2, there are two paths for severity estimation, the first is diagnostic indicators of the degradation level, and the second is direct size estimation of the spall. Because of the apparent physical meaning and monotonicity, the latter is considered more reliable and thus adopted in this study.

Most of the existing spall-size estimation methods are built on bearings with artificial defects [8], [45]. Signal processing techniques are adopted to extract the entry and exit signatures caused by the sharp edges. However, the entry/exit feature signals are often very weak and inconsistent for naturally extended spalls because of the irregular and ever-changing spall edges, which limited the effectiveness of existing methods.

Therefore, a novel approach is expected to be proposed to overcome this shortcoming. Petersen et al.'s recent works [10], [11] indicated that the bearing stiffness would decrease when a

rolling element is in the spalling area due to the destress of this element. Inspired by this finding, an approach of using the natural frequency perturbation of the signal caused by the stiffness to represent the length of the spall is brought up in this thesis. Instead of searching for the weak entry/exit points from the signal, this approach seeks effects on the signal that lasts during the whole spall-roller interaction period.

To identify the short duration of the natural frequency perturbation caused by bearing spall, a time-frequency analysis technique with high resolution in both time and frequency domains is required. The Wigner-Ville spectrum (WVS) method proposed for the analysis of mechanical signals by Antoni et al. [192], [193] is a good option, which has the advantage of overcoming the interference terms between frequency components.

A flowchart of this proposed approach is shown in Fig. 3-1, which illustrates its development process. The full construction of this approach is presented in Section 4, which is adapted from the published journal paper [14].

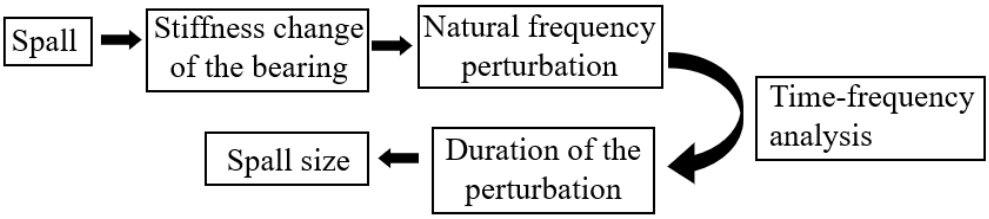


Fig. 3-1. Development process of the proposed acceleration-based approach

## 3.2 Spall size trending by multiple sensors (Objective 2)

In addition to developing an approach for acceleration-based fault severity assessment, this study investigated the abilities of other measurement approaches such as AE, IAS, and displacement. These new approaches are attracting more and more attention in recent years due to the fast development of IoT and the availability and affordability of different sensor technologies. As discussed in Section 2.4 and the beginning of Section 3, the establishment of severity assessment approaches for all measurements are based on the explanatory models of signals induced by the bearing defect. The relationships of measurements, signal models, and the methodologies for fault severity assessment were already presented in Table 3-1.

Some recent studies investigated these alternative measurements, but most of them only focused on one. In this research, four types of sensors (accelerometer, AE sensor, encoder, and load cell) will be applied simultaneously in the same bearing run-to-failure experiment, and their individual analysis results are compared with actual geometric measurement of the spall size. It needs to be noted that the encoder provides instantaneous angular speed (IAS) signal of the shaft, and the load cell gives the radial load applied on the test bearing, which could be seen as a proxy of the bearing housing displacement. The relationship between load and displacement is due to the floating bearing housing in the test rig, which is loaded horizontally by a hydraulic system. Change of the bearing inner-outer race deflection will therefore release the push rod slightly, which results in a fluctuation of the load signal. Further explanation of this relationship will be given in Section 5.

The study is firstly conducted under a relatively low shaft speed (6 Hz) and then extended to higher speeds for further validation.

## 3.3 Proximity probe-based approach (Objective 3)

During the comparison study of the four measurement approaches (acceleration, AE, IAS, and displacement), displacement estimates obtained from the load signal were found the best to track the spall size evolution. However, the relationship between load and displacement only works for the specific floating housing setup. Therefore, the third objective of this thesis was set to the investigation and validation of proximity probes as sensors measuring the relative displacement between the bearing inner race and outer race.

As will be seen in the experiment setup of Section 3.4, proximity probes were mounted on the same bearing rig and on a larger gearbox facility. For the bearing rig, the shaft is deemed almost rigid to radial deflection, and the displacement of the floating housing is measured by the proximity probe. In the gearbox facility, the bearing pedestal instead is rigidly installed in the machine structure. Therefore, the shaft displacement is measured to represent the relative deflection between bearing inner and out races. Based on these experiments, an automated fault-size estimation method by extracting the duration of displacement perturbation is proposed in Section 6.

## 3.4 Experimental testing and data collection

Reliable experimental data is the foundation to achieve the research objectives mentioned above. There are publicly available bearing run-to-failure experimental data sets, but they have some significant shortcomings for the purposes of this work: 1) they provide at most the spall size at the end of the bearing run-to-failure process, and the growing spall sizes are not measured during the experiment, 2) only a single measurement technology, mostly acceleration, is used. Therefore, new bearing run-to-failure experiments are planned and conducted in this research project to overcome these limitations. During our experiments, the test bearing is regularly disassembled to measure the growing spall size. Data of four types of sensors: accelerometer, AE sensor, encoder, and load cell (found to be a proxy of displacement), are collected simultaneously for each test.

As discussed in Section 3.3, the displacement measurement is found the best for spall size estimation. Therefore, experiments using proximity probes to directly measure the relative displacement between bearing inner race and outer race are designed. One is on the same bearing rig, and another is on a large gearbox facility.

In this section, the bearing run-to-failure experiments and the proximity probes-based experiments are presented separately. Some of the run-to-failure experiments are reproduced from the experimental sections of published journal papers of the author [14], [15]. All the experimental test rigs are owned by the UNSW Tribology and Machine Condition Monitoring Group.

### 3.4.1 Bearing run to failure experiments

The bearing run-to-failure experiments are performed on the bearing rig in UNSW, which is a SpectraQuest Bearing Prognostics Simulator (BPS). The structure of the bearing rig is shown in Fig. 3-2.

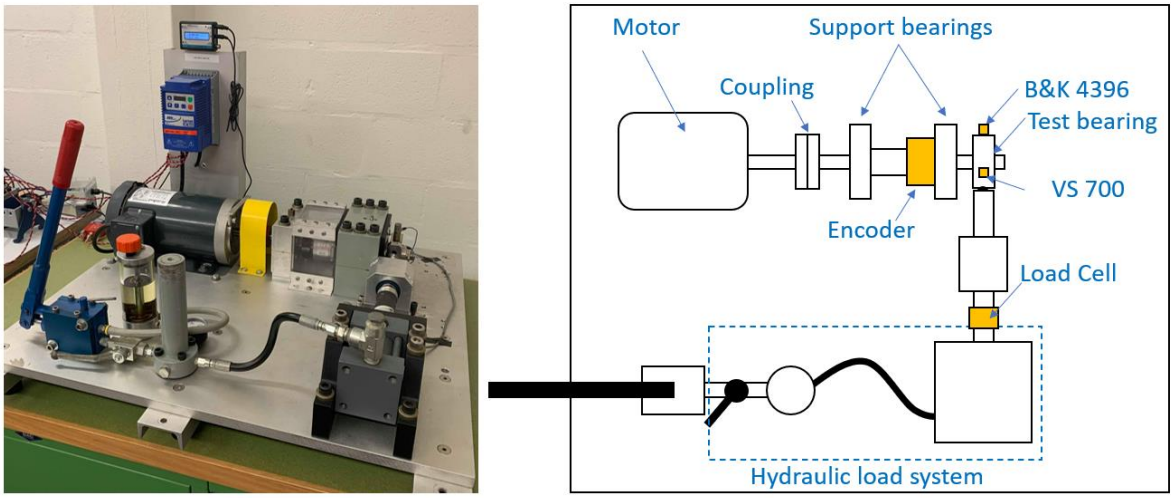


Fig. 3-2. SpectraQuest Bearing Prognostics Simulator. (Left) general view; (Right) plan view

The power source is a 3 phase AC motor (Marathon electric G590), which is controlled by the Lenze SMVector variable frequency drive (VFD). The shaft rotor is linked to the motor by a jaw type coupling (Lovejoy L090.750), and support bearings were mounted on both end of the shaft. A SKF N210 ECP cylindrical roller bearing is located at the drive end, and a couple of NSK 7011AW angular contact bearings are mounted at the non-drive end. The shaft extends out from the non-drive end support bearing, where the test bearing enclosed by a floating bearing case is installed and fastened on the shaft by two lock nuts. The hydraulic system is used to provide load in the horizontal direction to the test bearing through a loading rod, which has two-point connections with the case of the test bearing.

The model type of the test bearing is Nachi 6205-2NSE9 deep grove ball bearing, and its properties are shown in Table 3-2. The test bearings were manufactured to seed initial defects on the raceways to speed up the run-to-failure process. More details are provided in the following section of the test plan.

Table 3-2. Specification of test bearings

| Parameter | Value |
|---|---|
| Model | Nachi 6205-2NSE9 |
| Type | Single-row deep groove ball bearing |
| Number of balls | 9 |
| Ball diameter | 7.94 mm |
| Bearing pitch diameter | 39.04 mm |
| Contact angle | 0° |
| BPFO order | 3.58 |
| BPFI order | 5.42 |

As to the sensors, two accelerometers (Brüel & Kjær 4396) are installed on the horizontal and vertical direction of the test bearing to measure its vibration. An acoustic emission sensor (Vallen Systeme GmbH 700-D) is also designed to be installed on the vertical direction of the test bearing. The specifications of the accelerometers and the AE sensor are summarized in Table 3-3.

A Heidenhain ERN 120 rotary encoder is installed on the shaft between the two support bearings. It will give out a reference tacho signal and a 1024 per revolution encoder signal. A load cell (strain gauge bridge) was mounted on the push rod to measure the applied load and the temperature of the test bearing was also measured by a thermocouple to avoid overheating.

Table 3-3. Specification of sensors

| Sensor type | Sensor model | Sensitivity |
|---|---|---|
| Accelerometer | B&K 4396 | 10 $mV/ms^{-2}$ |
| AE sensor | VS 700-D | 1V/μbar |

Acceleration, encoder, and load signals are sampled at 51.2 kHz using a National Instruments NI9234 module, and AE signal is sampled with 1 MHz rate through National Instruments NI9223 module.

The purpose of the bearing run-to-failure test is to collect signals generated by naturally extending spall. To speed up this process, the test bearing is disassembled firstly, and an initial defect is seeded on the raceway. The initial defects varied in geometry: in the sample shown in Fig. 3-3. The first seeded defect is a small conical dimple of about 0.6 mm diameter and 0.1 mm depth, which was manufactured in our workshop by a hand-held high-speed drill with a small sanding tip. The others are round defects as that in the left picture of Fig. 3-4, which were manufactured externally by electro-discharge machining (EDM). Seven run-to-failure experiments were conducted in this project, and their key parameters are summarised in Table 3-4. For test number one, until a sudden RMS increase (from 1.2 to 3.5 mm/s) was observed at 620 thousand cycles, the applied load was then decreased from 14 kN load (100% of the dynamic load rating) to 11 kN, and the bearing was run for another 270 thousand cycles. The measured spall size at the end is about 8.5 mm in length. The other tests were conducted under constant load. Their running cycles and ending spall sizes are presented in Table 3-4 as well.

Table 3-4. Test plan of the run-to-failure experiments

| No. | Defect | | Initial size (μm) | Load (kN) | End cycles (k) | End spall size (mm) |
|---|---|---|---|---|---|---|
| 1 | Drill | | 640 | 11 | 890 | 8.5 |
| 2 | EDM | Round shape Outer race | 1000 | 14 | 200 | 6.5 |
| 3 | | | 1000 | 10.5 | 350 | 6.7 |
| 4 | | | 1000 | 7 | 2000 | 6.3 |
| 5 | | | 500 | 10.5 | 600 | 8.6 |
| 6 | | | 250 | 10.5 | 1000 | 6.1 |
| 7 | | Round shape Inner race | 500 | 10.5 | 1670 | 6.3 |

After initial defect manufacturing, the balls and the cages were recovered, and grease lubricant was applied. Nine pairs of 1.4 mm small screws and nuts were used to replace the formerly removed rivets. At last, enclosing the seals, the test bearing was placed into the bearing case and then mounted on the shaft, making sure that the seeded defect on the outer race was located

at the centre of the loading zone. During the experiment, the motor shaft was run at a constant speed of 30 Hz, and every 20-50 kilo cycles, the shaft speed was decreased to 20, 15, 12, and 6 Hz for 12 seconds of data acquisition at each speed. Moreover, the rig was stopped periodically during the test to disassemble the bearing and measure the spall size. Then the bearing was reassembled to continue the test.

During each stop, not only the size of the spall on the disassembled bearing race is measured, but also its topography is replicated by using a moulding technique and observed under laser scanning microscopes, as did for gear tooth surfaces in [194]. More detailed descriptions of this method and the analysis results of the spalling surface morphologies are provided by S. Zhuang in his recently published Master thesis [30]. It needs to be noted that the moulding technique requires a clean surface. Therefore, the grease of the test bearing was removed at each disassembly, and new grease was added when reassembling.

To present some examples, images of test 1, where spall growing from a small dip to the length of 8.5 mm, is shown in Fig. 3-3. Moreover, the mould image of the spall at the end of test number 3 is shown in Fig. 3-5 (a), where the circular feature centred at 2.3 mm from the left end of the figure is the seeded defect. To present a clearer look at the spall depth, a narrow strip between the red lines in Fig. 3-5 (a) was selected and averaged in the width direction, which brought the blue curve in Fig. 3-5 (b). Then the first and last few points of the curve were used to fit a circular arc, which is shown in orange line and represents the unmodified bearing raceway. The depth of the spall shown in Fig. 3-5 (c) was therefore obtained by subtracting the arc from averaged height curve. Since the ball diameter is 7.94 mm, it would not fall into the narrow deep holes in the latter half of the damaged area. Thus the average (effective) depth of the spall could be deemed to be about 50 μm.

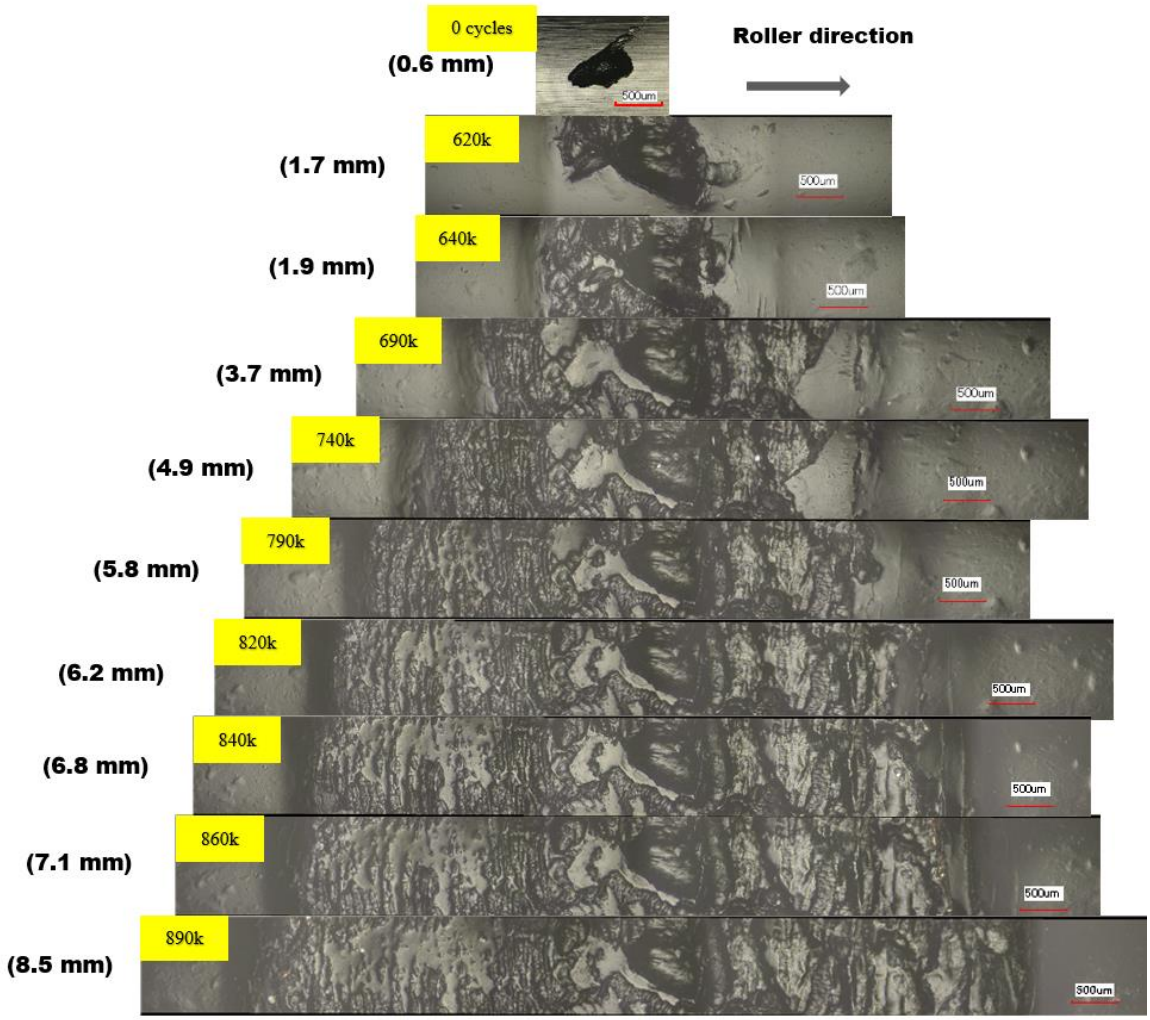


Fig. 3-3. Images of the spalling area replicated by the mould and captured by the laser microscope [30].

Fig. 3-4. Defect on the bearing outer race of test 3: (left) Seeded round defect manufactured by EDM, (right) Extended spall after 350k cycles

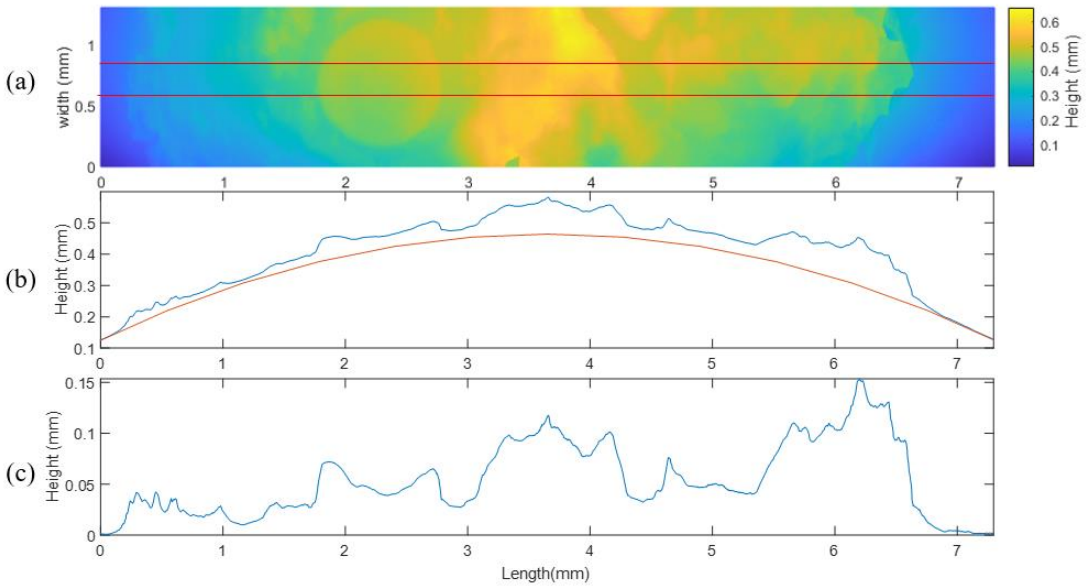


Fig. 3-5. Image of the extended spall at the end of test 3: (a) the spall replicated by mould, (b) the average height of the selected strip, (c) the spall depth

### 3.4.2 Experiments based on proximity probes

In addition to the four types of sensors applied in the bearing run-to-failure experiments, a proximity probe (Bently Nevada 3300) was utilised to directly measure radial displacement in experiments conducted on the same bearing rig and another larger gearbox rig.

The installation of the additional sensor on the bearing rig is illustrated in Fig. 3-6.

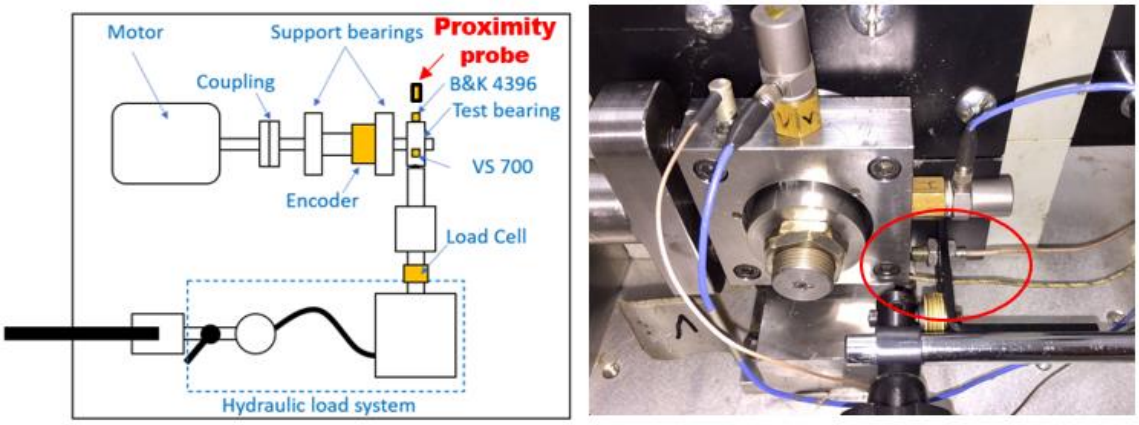


Fig. 3-6. Layout of the bearing test rig with a proximity probe installed

The bearing after the third run-to-failure experiment from Table 3-4 was adopted as the test bearing in this experiment, which has a 6.7 mm length spall on its outer race, and its mould image is shown in Fig. 3-7, which is another form of Fig. 3-5 (a). The bearing was installed with the fault in the centre of the load zone, i.e., in line with the loading rod. A load of 7 kN was applied, and the motor speed was set to 6 Hz.

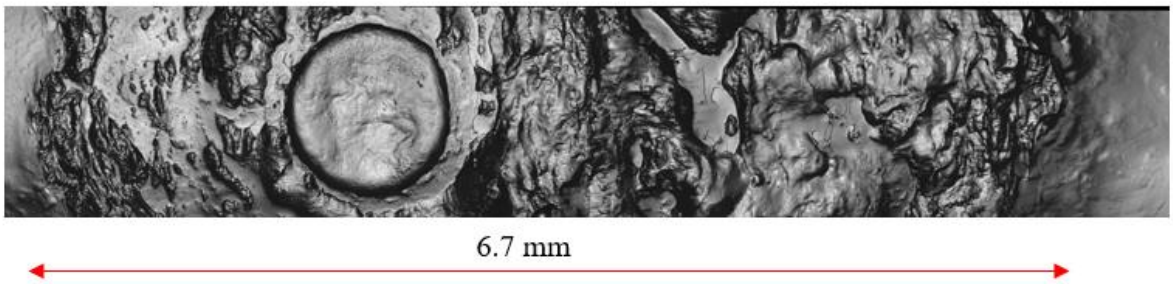


Fig. 3-7. Mould image of the spalling area captured from the test bearing of run-to-failure experiment no. 3 [30]

For the bearing rig, the outer race of the test bearing is mounted on a floating case, and the load is applied to the bearing case. This configuration is similar to the wheel hub bearing loaded by the vehicle weight through the suspension spring, but more common cases are that bearings are mounted on a solid base like in motors and gearboxes. To prove the applicability of the proximity probe-based approach on those cases, an experiment was conducted on the UNSW planetary gearbox facility, which is shown in Fig. 3-8.

The input shaft of the gearbox is seen at the upper side of Fig. 3-8, which is driven by an electric motor on the right outside the picture. After two gear stages, one parallel and one planetary, the power is transmitted to the output shaft, which is loaded by a hydraulic pump on the left.

As indicated in Fig. 3-8, the test bearing is mounted on the drive end of the pinion gear shaft, and the spalling area is placed on the bottom so that the weight of the shaft results in a load of the fault. The proximity probe was fastened to the foundation of the machine, where the bearing housing is installed. The sensor was pointed at the input shaft coupling of the first gear-stage (parallel) to measure radial shaft displacement in the vertical radial direction. The coupling was chosen due to the sensor requirement of a shaft diameter greater than 50 mm. Two encoders are installed on the input shaft and output shaft, respectively. The speed of the input shaft is set as 1.5 Hz during the test.

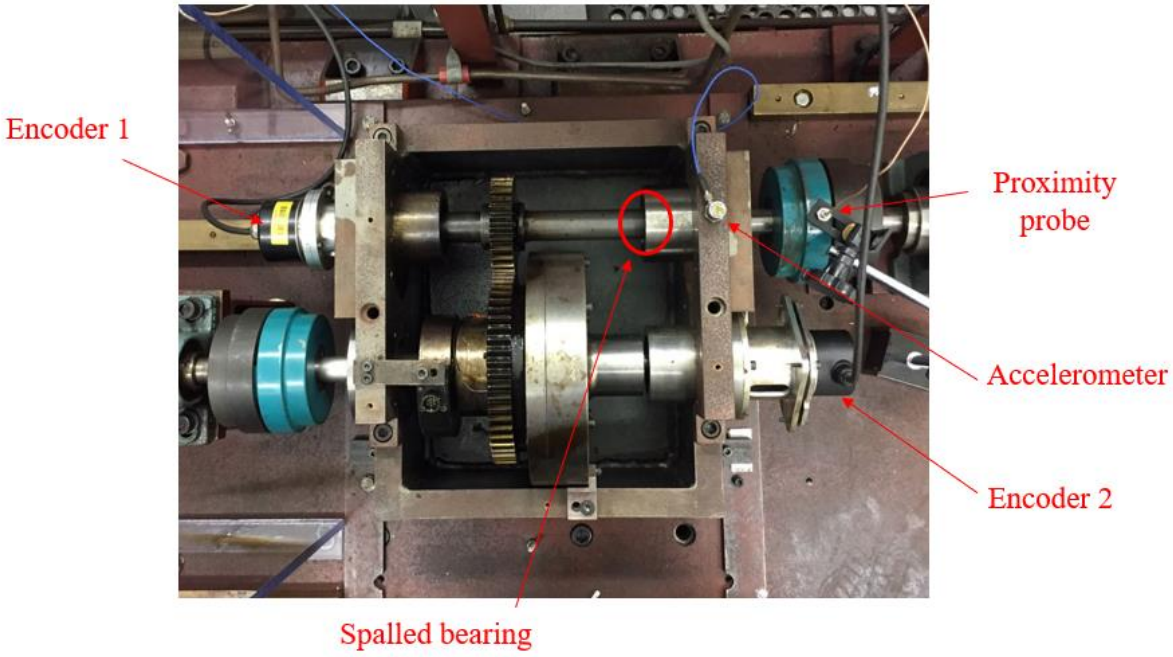


Fig. 3-8. Layout of the planetary gearbox and sensors

# 4. Tracking the natural evolution of bearing spall size using cyclic natural frequency perturbations in vibration signals

In Chapter 2, a systematic review has been conducted on the health condition monitoring of rolling element bearings, which demonstrated that the main obstacle to bearing prognostics is the lack of dependable severity estimation methods, especially for naturally developed bearing defects. Therefore, a series of bearing run-to-failure experiments have been designed and conducted, as presented in Chapter 3. Building upon the systematic review and the experimental data, a novel spall size estimation approach based on acceleration signal is proposed in this chapter to fulfil **Objective 1**. It is by extracting the natural frequency perturbation caused by the raceway spalling and is proved to be much more effective than the existing methods for naturally extended spalls.

This chapter is a modified version of the published paper "*Hengcheng Zhang, Pietro Borghesani, Wade A. Smith, Robert B. Randall, Md Rifat Shahriar, Zhongxiao Peng. Tracking the natural evolution of bearing spall size using cyclic natural frequency perturbations in vibration signals, Mech. Syst. Signal Process., 151: 107376, 2021"*.[2] I contributed more than 80% of the methodology development and manuscript writing. The paper was rearranged to fit

[2] Permission has been granted from co-authors.

the structure of the thesis. The literature review part was merged with Section 2.4.1, and the experimental rig setup was merged within Section 3.4.1.

## 4.1 Introduction

Because of the wide application of REBs in rotating machines and the fact that their failure is often the main reason for machine breakdown [176], condition monitoring of REBs has experienced growing interest in both academia and industry in recent times. Bearing faults can be classified into localised and distributed defects caused by many reasons, such as faulty installation, overload, and contamination. For properly designed, installed, and operated bearings, the most common failure type is spalling caused by fatigue.

Thanks to researchers' efforts and the technical development in the last decades, methods for fault detection and diagnosis of REBs using vibration analysis [103], [176] have been well developed in most aspects. Bearing prognostics, which aims to predict how much longer the investigated bearing could operate reliably, can be carried out in three steps [120]: (i) finding dependable indicators to reveal the fault severity of the bearing, (ii) building predictive degradation models for the bearing to show the progression of the fault, and (iii) predicting the failure time of the bearing based on the developed indicators and degradation models. Up to the present, however, bearing prognostics has been much less explored than other areas, and there is still no dependable prognostic strategy available for maintenance managers and engineers.

Since the first step of fault severity estimation, is a prerequisite for successful prognostics approaches, selecting effective and dependable indicators to identify and track the progression of bearing defects is critical. Many condition indicators have been developed by scientists and researchers for different purposes and different kinds of failure modes in the past. In general, they can be grouped into two different categories [7], [119], [120]: the first is to estimate the degradation level by trend indicators, and the second is to estimate the physical size of the spall directly. Because of the clearer physical meaning and its monotonic property, the latter is thought to be more reliable as a basis for successful prognostics and hence is of more interest in the present investigation. Although review papers [7], [119] have summarised these indicators, their performance has not been evaluated in respect to bearing prognostics.

Therefore, one purpose and contribution of this chapter is to compare the effectiveness of the developed spall size estimation methods.

The existing physical spall size estimation methods for REBs are based on the recognition that when a rolling element enters or exits the spall zone, a unique signal event is induced [195], and it can be identified by signal processing techniques. By knowing the time difference of the entry/exit points, bearing parameters and the shaft speed, the spall size can be calculated. Among the available studies reviewed in Chapter 2, Sawalhi's, Smith's and Moazen-Ahmadi's methods are probably the most popular and will be used in this chapter as a reference for comparison. All these methods were validated using vibration signals from bearings with artificial defects [8], [45], which have clear entry/exit signals caused by the sharp edge of the seeded spall. But when it comes to naturally extended spalls, the entry/exit feature signals induced by the sometimes-rough and sometimes-smoothed edges are inconsistent and often weak and thus likely to be masked by noise. In such cases these existing methods, which are reviewed in detail in Section 2, will lose effectiveness.

To overcome this shortcoming, a novel approach is proposed in this chapter based on detecting the signal differences during passage of the rolling element through the spall zone instead of at the entry/exit points. Inspired by Petersen et al. [10], [11], who demonstrated that the rolling element would destress in the spall zone, which would result in stiffness variation of the bearing and hence the natural frequency variation of the system, our idea is to use the duration of the natural frequency perturbation in the spall zone to represent the spall size. To detect the quick natural frequency perturbation during the roller-spall interaction, a time-frequency analysis method having high resolution in both the time and frequency domains is required. The Wigner-Ville spectrum (WVS) method [192], [193] is suggested in this chapter. While a time-frequency map has been used recently [60], [196], [197] to further detail entry and exit vibration-events in artificial spalls with sloped entry-exit, the proposed use of WVS is aimed at measuring spall-size based on the duration of the natural frequency perturbation, because of its much superior resolution. This is expected to be more reliable in case of natural faults where entry and exit events are often not so clearly distinguishable.

It should be noted that Ref. [198] also stated that bearing stiffness would decrease as a fault developed, and that the 'natural frequency of the bearing signal' could therefore be used for bearing prognostics. However, in [198] no information was given as to what was meant by the concept of a signal's natural frequency, or about how it could be measured. The currently proposed approach, on the other hand, recognises the existence of multiple resonance frequencies in the system and works by identifying a relevant local natural frequency and investigating its perturbation as the rolling element passes the spalled area. Moreover, our investigation does not find a monotonic change in frequency deviation with increasing fault size, as was implied in Ref. [198].

## 4.2 The natural frequency perturbation method

According to the discussion presented in previous sections, there are two ways of modelling the effects of a roller passing through a race fault. The first approach focussed directly on acceleration measurements, expecting a low frequency entry burst, a high frequency central impact and a low frequency exit burst. The second approach models the perturbation of natural frequencies of the system due to stiffness variation that occurs during the roller-fault interaction, as proposed by Petersen et al. [10], [11] in their numerical studies.

The effectiveness of the existing spall-size estimation methods (using the first approach) depends entirely on the accurate identification of the entry and impact/exit signatures, as presented in Table 1. However, the identification of these events is often challenging even in artificial faults due to their low energy (especially relative to the dominant central impact). This problem becomes even more critical in the case of naturally developed spalls.

Therefore, the methodology proposed in this study adopts the second modelling approach and focusses on the perturbation of an identified natural frequency in the system throughout the entire angular span in which the ball is travelling through the fault. A time-frequency analysis tool is employed to identify the length in time of the perturbation and determine the size of the spall accordingly.

It should be noted that publications [10], [11], [59], [72], [199] from Howard's team at the University of Adelaide show that they were more interested in dynamic modelling of the

bearing and did not apply this finding to size estimation of naturally extended bearing spalls. Within the same research group, other studies by Larizza et al. [60], [196], [197] also applied time-frequency analysis (STFT), but still focussing on entry and exit events rather than extended natural frequency perturbations, and are therefore still sensitive to the drawback of low-energy entry/exit events. In their studies, highly interesting phenomenological insights are found by means of time-frequency analysis, but still require the presence of clearly separable entry/impact/exit events in time.

The proposed work will instead apply WVS on full-length ball-pass periods, which are automatically obtained by order tracking the original signal using its BPFO/BPFI first harmonic (from squared envelope spectra) as a virtual tachometer. This removes the effect of the random variation in the period. An averaged WVS is then obtained combining all ball-pass periods for outer race faults. For inner race faults, due to the fact that they are strongly amplitude modulated at shaft frequency, only periods with high energy are selected for the average, which is the case in Section 5.2. The evolution of the natural frequency along a ball-pass period is then calculated thanks to the well-behaved properties of the time and frequency marginals of the WVS [200]. Finally, the spall-size is estimated based on the duration of the natural frequency perturbation over a ball-pass cycle. Considering this, the proposed method differs from previous approaches in the sense that it focusses on gradual and cyclic changes in the parameters of the structural transfer function (natural frequencies), rather than instantaneous excitations (parametric or otherwise). The procedure is summarised in

Fig. 4-1, and each step will be detailed in the following subsections, and applied on Test 1 data (1.6 mm rectangular notch on the outer race) as an illustrative example in Fig. 4-2.

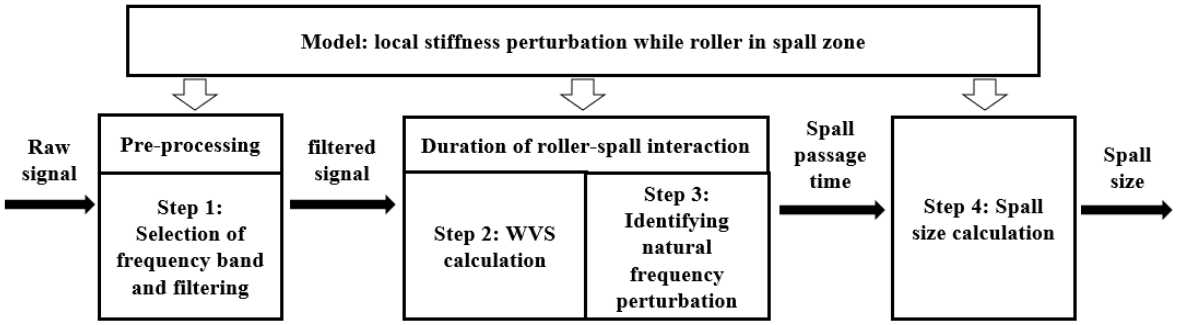

Fig. 4-1. Procedures of the proposed approach for bearing spall size estimation. (White arrows represent guidelines for signal processing steps, and black arrows indicate data transfer.)

Before discussing the details of each step, it is important to justify the choice of WVS as time-frequency indicator. The competing challenges of applying time-frequency analysis in this particular context are the short spall-passage time, defined by the usual small size of a spall, and the small variation in the natural frequency, as expected from a very small variation in stiffness due to the unloading of a single rolling element. As a result, good resolution in both the time and frequency domains is required simultaneously to efficiently identify the natural frequency perturbation region. The Wigner-Ville distribution (WVD) [200] was chosen for this purpose, since it exhibits superior time-frequency resolution and unbiased time and frequency marginals compared to other time-frequency indicators (e.g. the short time Fourier transform (STFT) or wavelet analysis).

The WVD of a signal $x(t)$ is defined as:

$$WVD_x(t,f) = \int_{-\infty}^{+\infty} x\left(t-\frac{\tau}{2}\right) x^*\left(t+\frac{\tau}{2}\right) e^{-j2\pi f\tau} d\tau \tag{4-1}$$

However, the WVD has the inherent limitation of spurious interference terms or cross terms, which result in smearing of different components. To eliminate the interference terms, many smoothing and kernel methods have been developed. However, Antoni in [192] suggested using the Wigner-Ville Spectrum (WVS), which can average out the interference terms for second order cyclostationary signals, and would therefore be suitable for our proposed approach.

The WVS of a signal $x(t)$ can be calculated as:

$$WVS_x(t,f) = \int_{-\infty}^{+\infty} R_x(t,\tau) e^{-j2\pi f\tau} d\tau \tag{4-2}$$

where $R_x(t,\tau)$ is the autocorrelation function:

$$R_x(t,\tau) = E\left[x\left(t-\frac{\tau}{2}\right) x\left(t+\frac{\tau}{2}\right)\right] \tag{4-3}$$

The WVS calculates the Fourier transform of the autocorrelation with respect to the time lag ($\tau$) and thus can be considered as the expected value of the WVD. If the signal under consideration is a second order cyclostationary signal, then the instantaneous autocorrelation is periodic, and it can be consistently estimated by synchronously averaging over many cycles, as presented in Eq. (4-3).

In [193], [201], a practical WVS algorithm based on spectral correlation is provided and applied on cyclostationary signals obtained from different machine phenomena.

**Step 1: Selection of frequency band and filtering**

The first step of the proposed approach is to identify two frequency bands, a wide band ($f_1, f_2$) and a narrow band ($f_3, f_4$), around a natural frequency of the system from the power spectral density (PSD) of the signal (usually identified as a high magnitude peak). The wide frequency band is utilised to band-pass filter and down sample the raw acceleration signal to reduce the computational requirement and processing time. The narrow frequency band, which is within the wide band, is used in the following step to calculate the average frequency. The reason for using two different frequency bands is that the wide band (10 – 5000 Hz in this case) ensures high resolution in the time domain, and then the small perturbation of natural frequency can be detected from the narrow band (700 – 1200 Hz) in the following steps. The bands were manually selected around high magnitude peaks observed from the PSD in this chapter, and their bandwidths (especially for the narrow band) were adjusted to provide a good result. A more robust and ideally automated band selection step is suggested for future work. Since the experimental data has very high signal-to-noise ratio, the pre-whitening process was deemed optional.

**Step 2: Order tracking and WVS calculation**

Since the WVS is based on the cyclostationarity of the faulty bearing signal and, due to random slip, bearing fault signals are strictly pseudo-cyclostationary [103], order tracking according to the ball pass frequency of the outer/inner race (BPFO/BPFI) would overcome the fluctuation in rotational speed and instability due to ball slippage, thus helping to restore cyclostationarity to the signal and hence to reveal the periodicity of the instantaneous autocorrelation. A

tachometer-less order tracking technique proposed by Bonnardot et al. [202] is applied in this chapter to obviate the requirement of an encoder and expand its application scope. The technique employs the unwrapped instantaneous phase of the envelope signal band-pass filtered around ball pass frequency with a tolerance of ±10% as a reference to interpolate the acceleration signal at equal steps in phase angle.

After order tracking, each signal segment of ball pass occurrence should have the same number of samples. The WVS can then be computed by averaging over all these segments (selected ones for inner race fault), giving the result shown in Fig. 4-2 (a). But as our aim is to investigate the local natural frequency perturbation, only the WVS within the narrow frequency band selected in the previous step (700 – 1200 Hz in this case) is plotted and will be computed in the following steps.

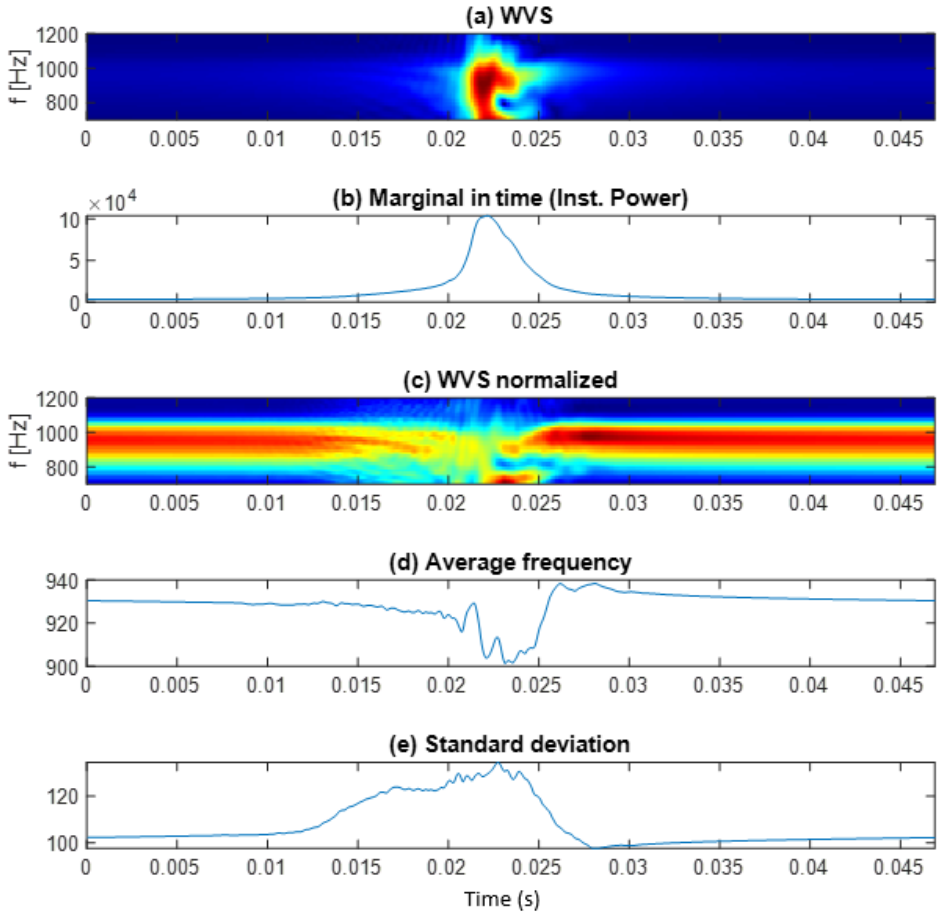


Fig. 4-2. The proposed approach applied on Test 1 data (spall size 1.6 mm, or 0.0045 s in time for this case): (a) Wigner-Ville Spectrum in the length of one ball pass occurrence; (b) instantaneous power calculated by integrating WVS in the frequency domain; (c) normalised WVS calculated by dividing WVS to its instantaneous power; (d) average frequency of the normalized WVS; (e) standard deviation of the normalized WVS

### Step 3: Identifying natural frequency perturbation

Seen from the WVS presented in Fig. 4-2 (a), it is obvious that the impact event in the middle has the highest instantaneous power, which prevented the observation of the remaining (non-impact) part. Therefore, the WVS is normalised by dividing its instantaneous power (Fig. 4-2 (b)) as:

$$WVS_{norm} = \frac{WVS_{x_w}(t,f)}{|x_w(t)|^2} \tag{4-4}$$

where $|x_w(t)|^2$ is the instantaneous power, and can be calculated from its time marginal by integrating the WVS in the frequency domain:

$$|x_w(t)|^2 = \int_{f_3}^{f_4} WVS_{x_w}(t,f)df \tag{4-5}$$

The normalised WVS is presented in Fig. 4-2 (c) from which it is easy to observe that this natural frequency decreased in the middle of the window, during the interaction between the rolling element and the spall. To demonstrate this more clearly, the average frequency, shown in Fig. 4-2 (d), is calculated from the un-normalised WVS by:

$$\langle f_n \rangle_t = \frac{1}{|x_w(t)|^2}\int_{f_3}^{f_4} f \cdot WVS_{x_w}(t,f)df \tag{4-6}$$

The average frequency can be calculated from the normalised WVS as well; the only difference is that the instantaneous power of the normalised WVS is always 1 in time.

The standard deviation, shown in Fig. 4-2 (e), can also be analysed to determine the local spread of the frequency by:

$$\sigma_{f|t} = \sqrt{\langle f_n^2 \rangle_t - \langle f_n \rangle_t^2} \tag{4-7}$$

where $\langle f_n^2 \rangle_t$ is the second conditional moment in frequency:

$$\langle f_n^2 \rangle_t = \frac{1}{|x_w(t)|^2}\int_{f_1}^{f_2} f^2 WVS_{x_w}(t,f)df \tag{4-8}$$

The performance of the standard deviation was found to be weaker than the average frequency in representing the spall size; therefore, the latter is mainly used in the following discussion.

**Step 4: Spall size calculation**

Seen from Fig. 4-2 (d), the natural frequency decreased from 930 Hz to 900 Hz in the spall zone, and the duration of the perturbation region should be representative of the spall size (1.6 mm, or 0.0045 s in this case). It is easy to manually select a threshold (e.g. 910 Hz in this case) as a trigger whereby the crossings of the trigger by the average frequency represent the entry

and exit points of the spall, and their interval the entry to exit time. The spall size can then be calculated accordingly by:

$$l = \frac{\pi f_r \left(D_p^2 - d^2\right)}{2D_p} t_{exit} \tag{4-9}$$

To avoid the arbitrariness of the manual threshold selection for different cases and different frequency bands, it is recommended to firstly normalise the average frequency by:

$$f_{n_{norm}} = \frac{f_n - f_n(1)}{\min(f_n) - f_n(1)} \tag{4-10}$$

Which means the first point of the average frequency is 0 in the normalised average frequency, and the deviation of the minimum point (or maximum point if the natural frequency increases) of the average frequency is 1 in the normalised average frequency. Therefore, the same threshold, e.g. 0.4, can be applied for all cases.

Another method to interpret the natural frequency perturbation is to fit it to a Gaussian distribution, and its standard deviation σ is representative of the width of the perturbation range, thus the estimated size is:

$$l = \frac{\pi f_r \left(D_p^2 - d^2\right)}{D_p} \sigma \tag{4-11}$$

## 4.3 Experiment setup and data collection

Three sets of experimental data were used in this chapter to verify and compare different methods and indicators. They were all collected from the UNSW Bearing Prognostics Simulator as presented in Section 3.4. However, the first two come from previous studies [80], [136], while last was collected during this thesis.

### 4.3.1 Test 1: artificially seeded rectangular notch

The first experiment consists of a single short-term run. A Brüel and Kjær 4394 IEPE-type accelerometer was stud-mounted in the horizontal direction of the test bearing case, and its vibration signal was collected by a Brüel and Kjær PULSE frequency analyser. The sampling frequency was 131,072 Hz and the duration of the record was 10 seconds.

The test was conducted at a shaft speed of 6 Hz, with 7 kN load applied, which is 50% of the rated dynamic load capacity of the test bearing. A through-notch with 1.6 mm width and 0.5 mm depth was seeded on the outer race of the bearing using electric spark erosion. The seeded fault is rectangular with sharp edges as described in Ref. [149].

### 4.3.2 Test 2: naturally extended spall from a rectangular notch

Test 2 consisted of a long-term degradation test, described in detail in Ref. [80], [136]. A notch of 0.4 mm width and 0.15 mm depth was seeded on the inner race of the bearing at the beginning. The seeded spall then extended naturally during 28 hours of running at a shaft speed of 6 Hz. For the first 20 hours, 7 kN load (50% rated dynamic load) was applied, while in the final 8 hours, it was increased to 14 kN (100% rated dynamic load). During the test, the bearing was disassembled to investigate the extended spall every 4 hours for the first 20 hours and every 2 hours for the final 8 hours. Vibration signals were collected every half an hour during the whole test. Compared to Test 1, the extended faults here are likely to more realistically represent naturally initiated faults. The faults extended from the 0.4 mm to 5.92 mm during the experiment as described in [80]. In this test, the only difference in data collection compared to Test 1 was that a PCB 352C04 accelerometer was used instead of the B&K 4394.

### 4.3.3 Test 3: naturally extended spall from a small conical dimple

This test is test number 1 discussed in Section 3.4.1. To remind the reader of a few important details, this test started from a small, drilled defect (a conical dimple of about 0.5 mm diameter and ~0.1 mm depth) on the outer race, and ended after 890 kilo cycles with spall increased to 8.5 mm in length.

## 4.4 Results

Three representative existing spall size estimation methods (Sawalhi's method, Smith's method and Moazen's method) and the proposed natural frequency approach were applied on the three experimental data sets presented in the last section. Their results and effectiveness are compared in this section.**Results of Test 1: rectangular notch**

The processing steps and results of existing methods and the proposed approach applied to Test 1 data were already presented in Sections 2 and 3. To compare the methods' effectiveness, their

analysis results are repeated here, and presented together with the spall size and raw vibration signal in Fig. 4-3. The duration of the presented signal is one ball pass occurrence, and the spall 'signal' Fig. 4-3 (a) is arranged (approximately) so as to position the rolling element/spall interaction in the middle of the record. The spall in this test is 1.6 mm in length and 0.15 mm in depth.

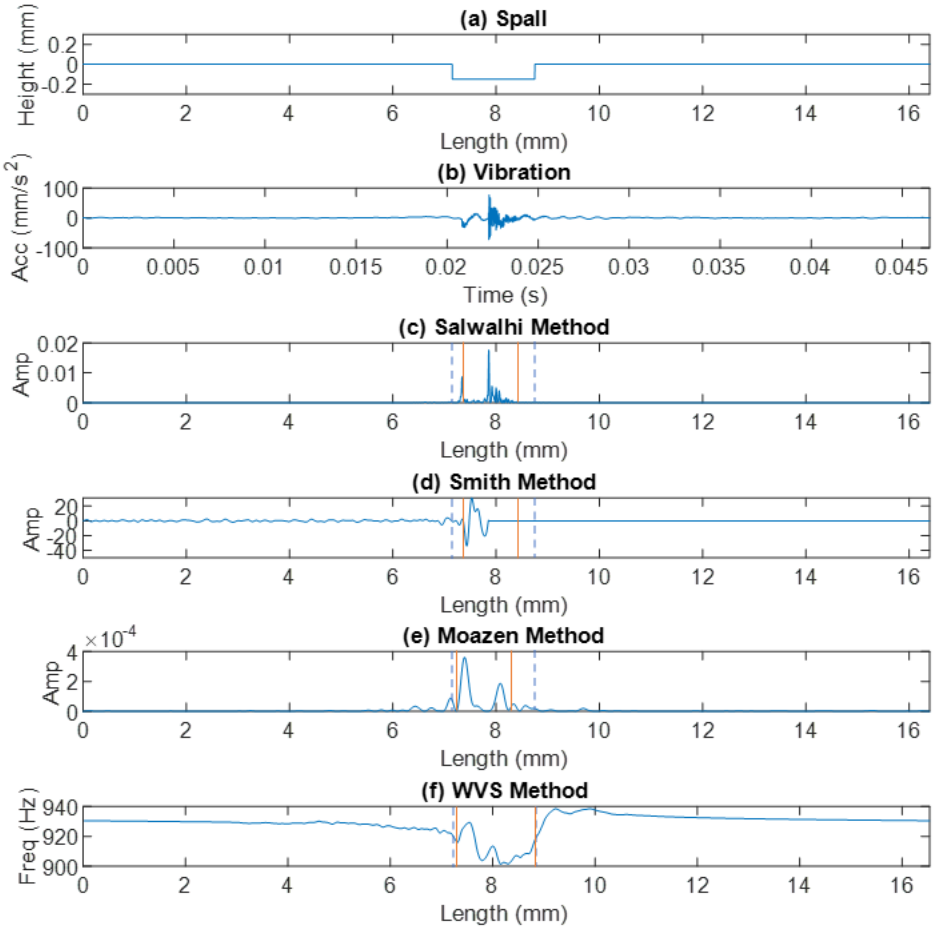


Fig. 4-3. Comparison of spall size estimation methods on Test 1 data (blue dashed line for measured size and red line for estimated size): (a) The spall (aligned approximately according to the impact event in the centre); (b) The collected vibration signal in time domain; (c) Sawalhi's method to reveal the entry and impact points, and the dotted lines represent the spall edges; (d) Smith's method (gradient); (e) Moazen's method to reveal the entry and exit points; (f) The natural frequency variation method by using WVS

As seen from Fig. 4-3, the clear and sudden change of shape on the leading and trailing edge of the rectangular spall arouses distinct entry and impact events in the acceleration signal as shown in Fig. 4-3 (b), while the low-frequency exit event is concealed in the decaying impact.

The entry and impact points are detected as two peaks in Sawalhi's method in Fig. 4-3 (c), and as known from previous discussion in Section 2, their distance of separation should be half of the spall size, which is consistent with what is shown here.

For the result of Smith's method in Fig. 4-3 (d), only the gradient signal is plotted here. The gradient signal is set to zero after the impact point, and the entry is recognised by the first zero crossing point before the roll-off effect. The distance of entry to impact in this plot is also half of the spall size, as with the result of Sawalhi's method in Fig. 4-3 (c).

Alternatively, Moazen's method intended to identify the low-frequency entry and exit events, shown as two peaks in Fig. 4-3 (e), with their separation distance used to estimate the full length of the spall. Compared to the previous two methods, the exit point identified here occurs after the impact point, but the entry to exit distance is still shorter than the real spall size shown in Fig. 4-3 (a). Therefore, compensation equations for the de-stressing and re-stressing process of the ball entering and exiting the spall area were introduced by Moazen, which can be found in Table 2-1.

All three above mentioned methods are successful in estimating the spall size, but their estimates are shorter than the actual spall. Compared to them, the result of the proposed method shown in Fig. 4-3 (f) provides a closer estimated size without any compensation algorithm. Table 4-1 shows a qualitative comparison of the improvement achieved in terms of estimation accuracy with the newly proposed technique, even if the results for previous techniques might be slightly improved by fine-tuning the parameters.

It should be noted that for plots (c) to (f) the signal has been order tracked according to the fault frequency, so that the x-axis effectively represents angle domain for the cage, which has been converted to the circumferential position along the relevant race. Differently from plots (c) to (e), which were processed directly from a single segment of vibration signal as shown in plot (b), plot (f) is an averaged result deriving from several such segments. Therefore, the perturbation area is not perfectly aligned with the previous plots.

Table 4-1. Comparison of spall size estimation methods on artificial spall (1.6 mm)

| Method | Estimated size (mm) | Percentage of error |
|---|---|---|
| Sawalhi's method | 1.12 | 30% |
| Smith's method | 1.21 | 24.4% |
| Moazen's method | 1.14 | 28.8% |
| Proposed | 1.53 | 4.3% |

### 4.4.2 Results of Test 2: natural spall extended from a rectangular notch

The same procedures were applied on Test 2 data for comparison. Different from the rectangular notch in Test 1, the spall was naturally extended from the notch in Test 2. The rough and irregular leading/trailing edges led to much weaker low-frequency entry/exit events in the vibration signal, which brought great difficulties to the size estimation of the extended spall. Another difference is that the spall of Test 2 is on the inner race rather than outer race (Test 1), which meant the impact signal was amplitude modulated by shaft rotation frequency, and therefore only some of the ball pass occurrences with high impact can be selected for calculation as mentioned in Section 3.

The results of the three existing methods and the proposed approach implemented on the vibration signal excited by an extended spall of 5.92 mm are gathered in Fig. 4-4, and the results of two other extended spall cases (2.18 mm and 4.50 mm) are also presented in Fig. 4-12 and Fig. 4-13 in the Additional results.

The existing methods, whose results are shown in Fig. 4-4 (c), (d), and (e), all fail to identify the entry/exit positions because of the weak signal generated by the naturally extended edges. On the contrary, the result of the proposed approach shown in Fig. 4-4 (f) indicates that the identified natural frequency of the machine decreased approximately 40 Hz (from 1080 Hz to 1040 Hz) while the rolling element traversed the spalled area, which clearly reveals the size of

the spall. This comparison demonstrates the superiority of the proposed approach to the other methods.

It is worth noting that some publications [50], [155] suggested the use of synchronous averaging to estimate size for naturally occurred bearing spalls, but they still suffer from the ambiguity problem of choosing entry and exit points, while a much clearer result is obtained in the proposed approach.

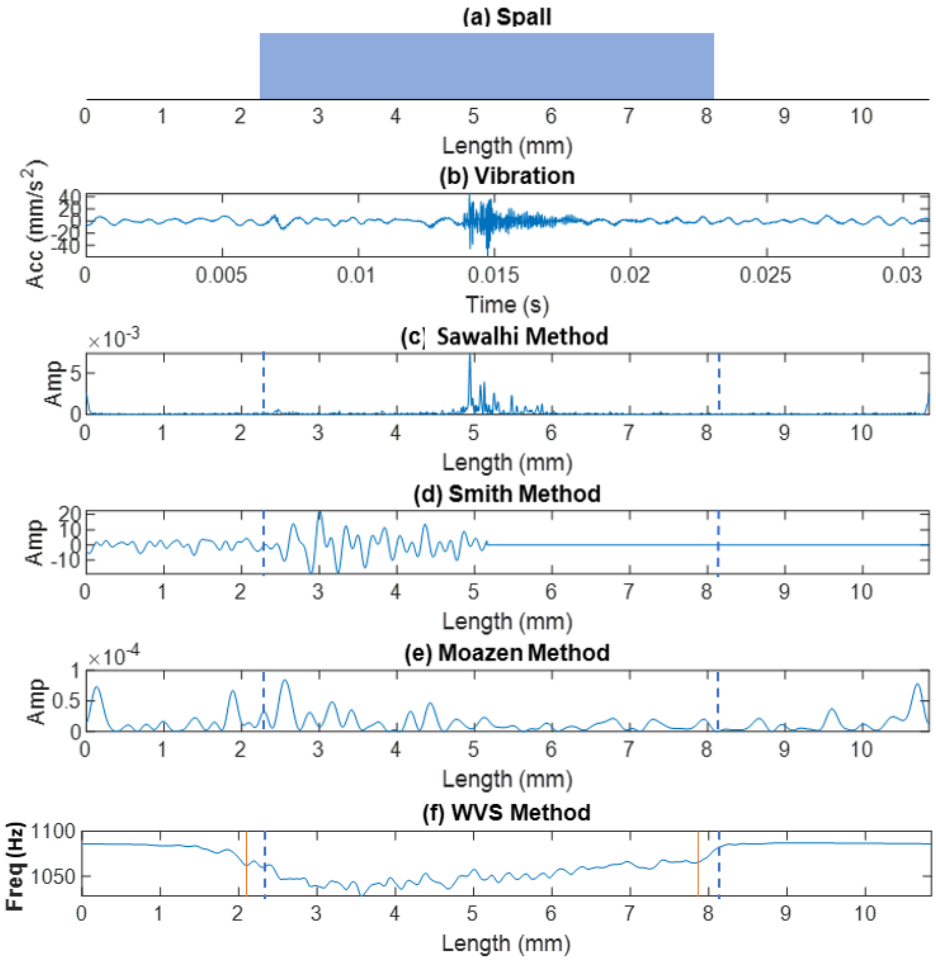


Fig. 4-4. Comparison of spall size estimation methods for 5.92 mm extended spall of Test 2 (blue dashed line for measured size and red line for estimated size): (a) The size of extended spall; (b) The raw vibration signal, (c) Sawalhi's method to reveal the entry and impact points, (d) Smith's method (gradient), (e) Moazen's method to reveal the entry and exit points, (f) The proposed approach by using WVS

To further validate this proposed approach, all the Test 2 data, from the beginning with a 0.4 mm rectangular slot to the final 5.92 mm extended spall were analysed to trend the spall growth. Since the spall only started to propagate in the final 8 hours of this test, Fig. 4-5 shows the natural frequency perturbation in two different bands (700 – 1400 Hz, and 1800 – 2600 Hz) in this period (20 – 28 hours). It is clear to see that the width of the perturbation area in both bands is increasing as the spall size grows. The normalised WVS results for both bands are shown in Fig. 4-16 of Section 4.6, which also display an increasing trend of the spalling area. Perhaps due to installation factors or a deviation in the manual load application, the studied natural frequencies vary by up to about 10% across the cases, from 1000 to 1100 Hz in the first band and 2100 to 2300 Hz in the second band.

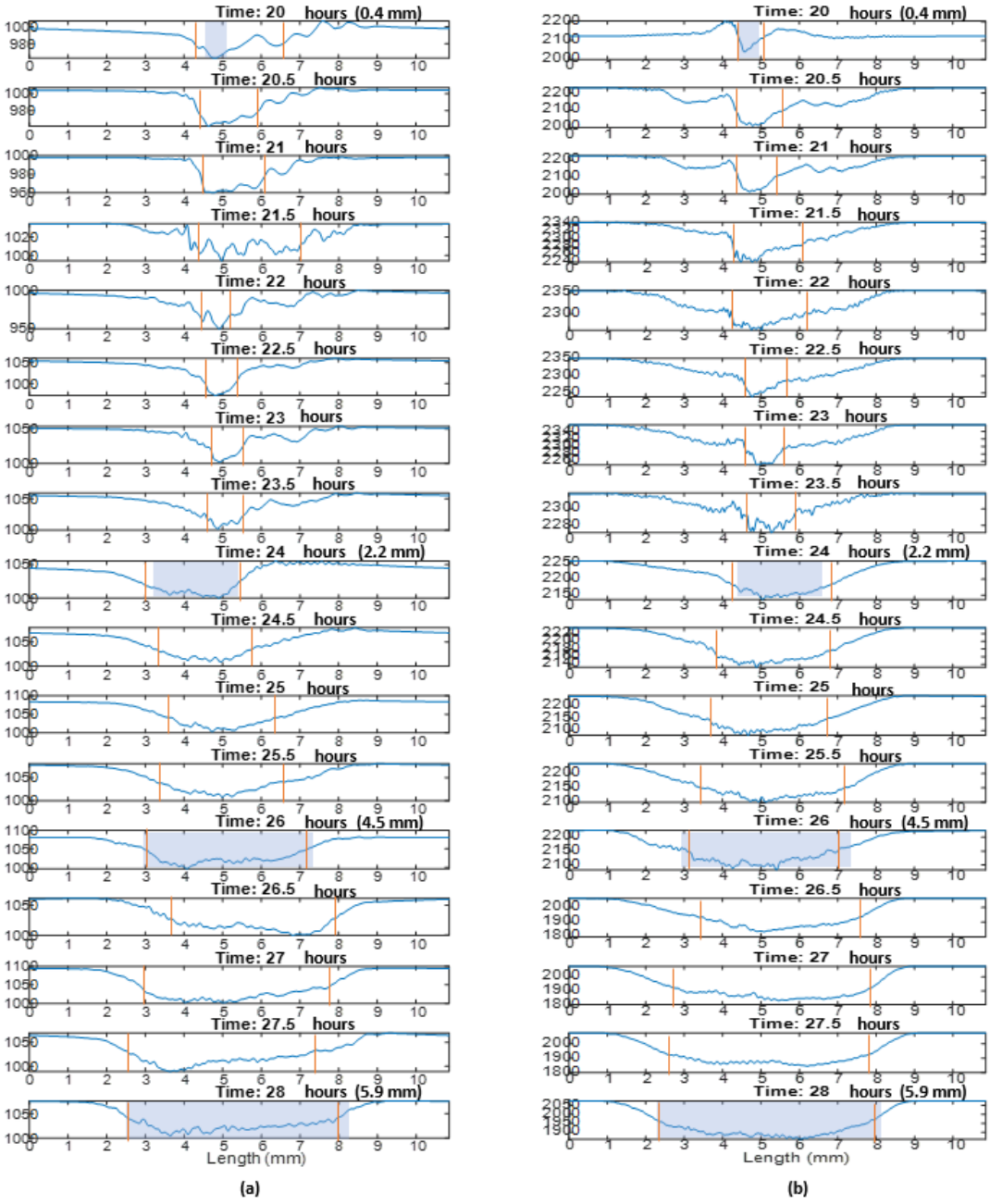


Fig. 4-5. The trend of natural frequency perturbation for Test 2 data in two different bands (the shaded areas represent the measured spall size, and the red lines represent the estimated size): (a) 700 - 1400 Hz, (b) 1800 – 2600 Hz

The estimated sizes are shown in Fig. 4-6 with a comparison with the measured size. As stated in Section 4.2, the size was only measured at 20, 24, 26 and 28 hours, while the vibration signal was collected every 0.5 hours. Therefore, the growth of the spall from 0.4 mm to 2.18 mm from

20 to 24 hours is unknown. And given that the size is relatively small in this area, the signal is likely more affected by the impact caused by the ball hitting the original artificial slot. This leads to a fluctuation in the size estimation results in this area. After this range, the estimated spall sizes become nearly monotonic from 22 hours to the end at 28 hours, and they are quite close to the measured sizes.

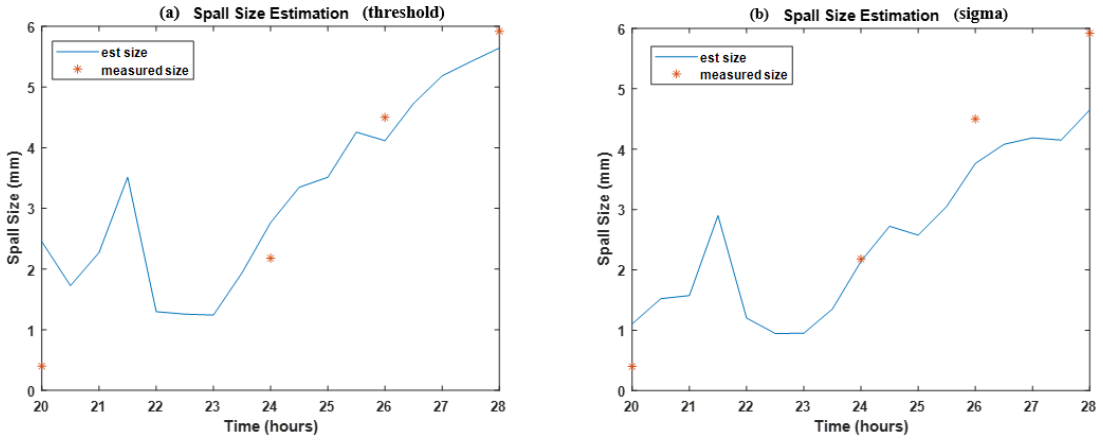


Fig. 4-6. Estimated spall size compared to the measured size (Test 2): (a) use of handpicked threshold (0.4) for the normalized average frequency to estimate the spall size; (b) use of standard deviation to represent the spall size

The size estimation results for the first 20 hours of Test 2 are shown in Fig. 4-7, during which period the seeded rectangular notch basically remained unchanged in size and shape. The plot displays a similar fluctuation of estimated size as in 20 - 22 hours, which suggests a limitation of this approach for spalls of small sizes. The main explanation for this behaviour is that when the spall is small (shorter than about 1.5 mm in this case), there is not enough time for the natural frequency to settle to another level, therefore making it difficult to track its change within a ball-pall cycle. Furthermore, the natural frequency perturbation is derived by averaging over many ball-pass periods, and thus jitter could play a significant role in reducing the visibility of frequency perturbations for small faults.

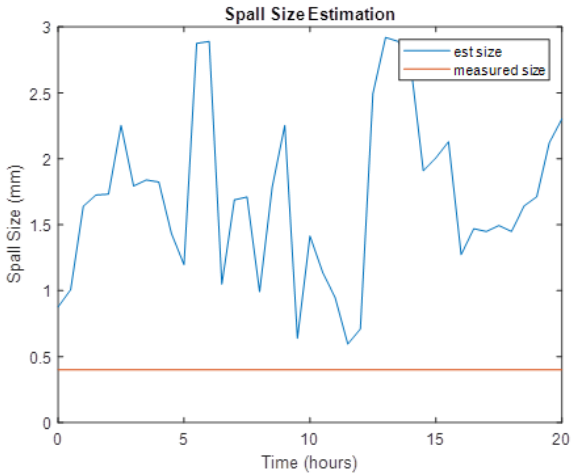


Fig. 4-7. Size estimation results for the first 20 hours of Test 2

This section of analysis confirmed that the proposed method could provide acceptable size estimation results when the bearing spall is relatively large (over about 1.5 mm in this case). In the meantime, it also revealed the limitation of this approach for small spall sizes. One possible solution may be using other indicators, such as RMS and kurtosis to track the fault severity when the spall is small, until a monotonic trend is displayed for the size estimation, as the actual spall size would not decrease.

### 4.4.3 Results of Test 3: natural spall extended from a small conical dimple

Since the naturally extended spall in Test 3 started from a small drilled defect on the bearing outer race, it is more like a naturally occurred and extended spall than the previous two tests, and it does not contain a clear edge in the two sides or in the middle, as seen from Fig. 4-8 (a). This is reflected in the vibration signal, shown in Fig. 4-8 (b), which exhibits no high-frequency impact event in the roller-passing spall process, and the low-frequency entry/exit events are also very weak. Therefore, Smith's method, which seeks the high-frequency impact event to locate the entry event, cannot be performed, and the results of the other two methods are clearly unsatisfactory. Meanwhile, the proposed approach can still recognise the spall zone effectively, as seen from Fig. 4-8. Results for two other spall sizes (1.93 and 5.57 mm) are also shown as examples in Fig. 4-14 and Fig. 4-15.

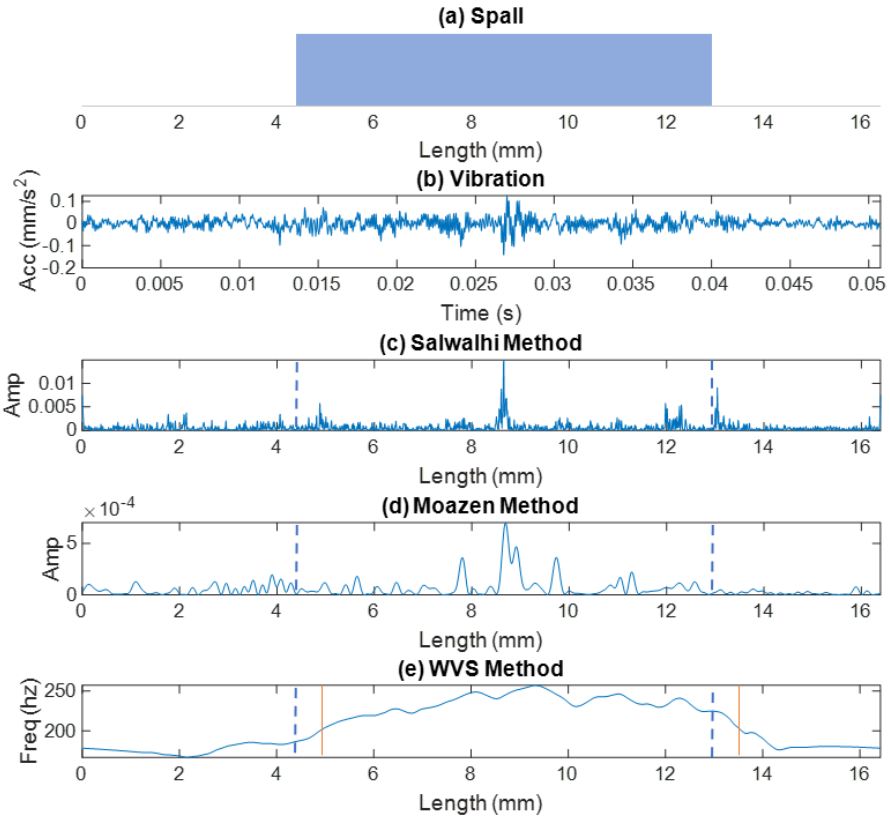


Fig. 4-8. Comparison of different spall size estimation approaches for 8.52 mm spall of Test 3 (blue dashed line for measured size and red line for estimated size): (a) The size of extended spall; (b) The collected vibration signal; (c) Sawalhi's method to reveal the entry and impact points; (d) Moazen's method to reveal the entry and exit points; (e) The proposed approach by using WVS

As with Test 2, data of different spall sizes were analysed to trend the spall growth. Two frequency bands, 10 – 400 Hz and 500 – 2000 Hz, were selected for this analysis, and their natural frequency perturbations are shown in Fig. 4-9. Compared with the previous two tests, the two natural frequency bands selected in this test are much lower, which may be due to the modification of the test rig loading rod from one-point contact to two-point contact with the bearing case before conducting Test 3.

The increasing trend of the estimated spall area seen from the natural frequency perturbations is obvious for both bands, as shown in Fig. 4-9, and a similar trend can be observed from Fig. 4-17 of Section 4.6. It can be seen in Fig. 4-9 (a) that average frequency increases in the affected area instead of decreasing as in our assumption. One possible explanation is the low frequency

band is more influenced by the whole bearing housing, test bearing, loading rod and hydraulic pump piston oscillation, with the hydraulic fluid in the cylinder acting as a nonlinear spring (purely an artefact of the test rig). Another reason may lie in that the perturbation part is leakage from a higher natural frequency band, which appears as an increase in this natural frequency after normalisation. In Fig. 4-9 (b), the natural frequency in the second band (500 – 2000 Hz) fluctuates a lot during the spall zone. This may be caused by the rolling element reconnecting with the bottom of the spall area and becoming restressed in the middle of the spall zone.

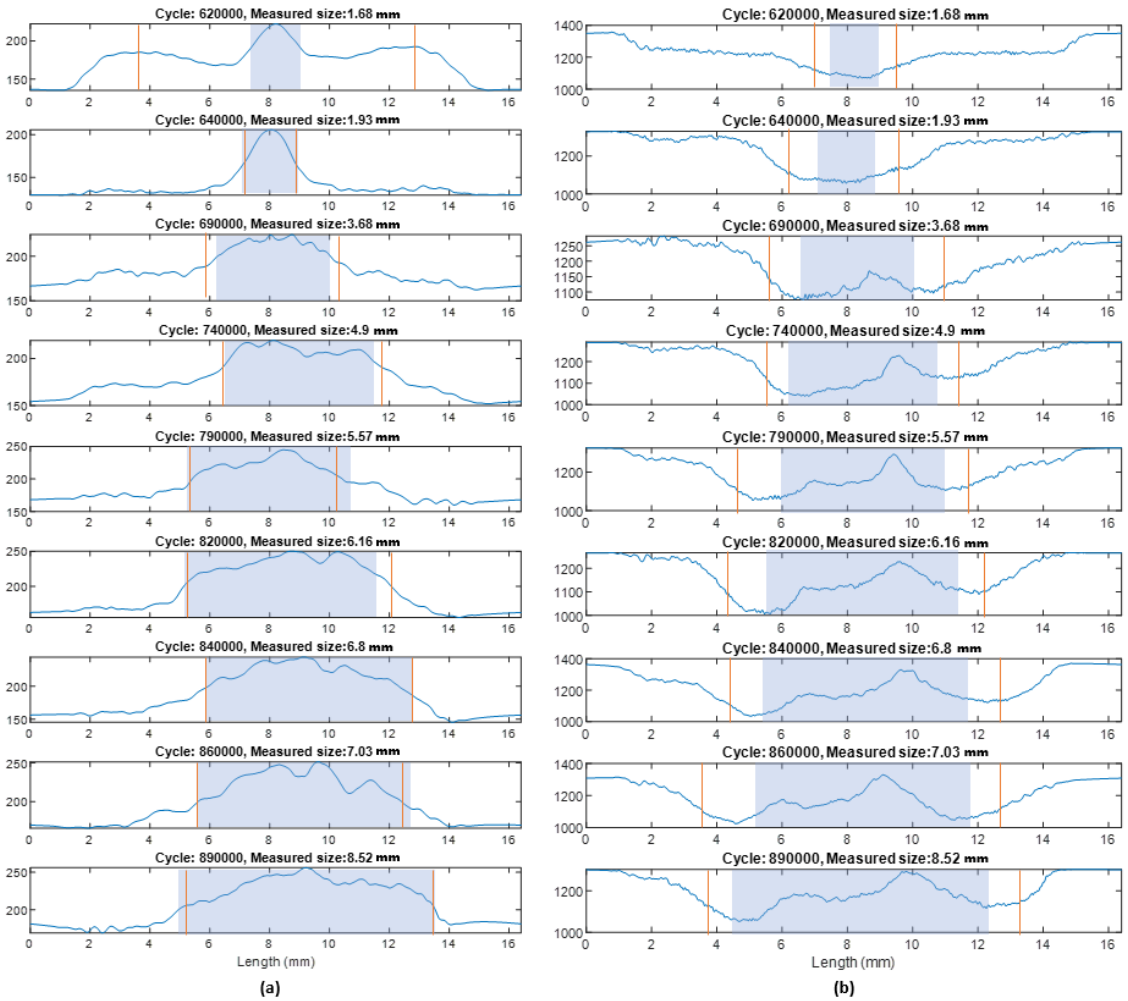


Fig. 4-9. The trend of natural frequency perturbation for Test 3 data in two different bands (the shaded areas represent the measured spall size, and the red lines represent the estimated size): (a) 10 - 400 Hz, (b) 500 – 2000 Hz

The estimated spall sizes compared to the measured ones are plotted in Fig. 4-10 and Fig. 4-11. As with Test 2, two techniques were utilised to express the spall size: the handpicked threshold technique, and the standard deviation technique, whose results for the 10 - 400 Hz band are shown in Fig. 4-10 (a) and Fig. 4-10 (b), respectively. It seems that the threshold technique tracks the spall size better in the larger area than the standard deviation technique, although they both wrongly estimate the 1.6 mm spall at 620 thousand cycles.

When applying the same techniques to the 500 – 2000 Hz band, it was found that the large fluctuation of the average frequency made it impossible to fit to a Gaussian distribution. While the threshold technique can still trend the spall growth (Fig. 4-11), it suffers from an over estimation of the size.

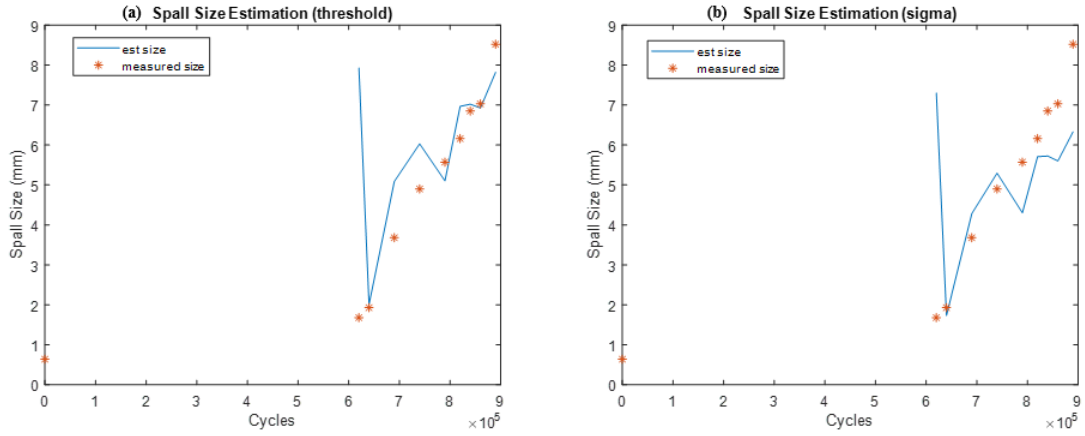


Fig. 4-10. Estimated spall size of 10 – 400 Hz band compared to the measured size (Test 3): (a) use of handpicked threshold (0.5) for the normalised average frequency to estimate the spall size; (b) use of standard deviation to represent the spall size

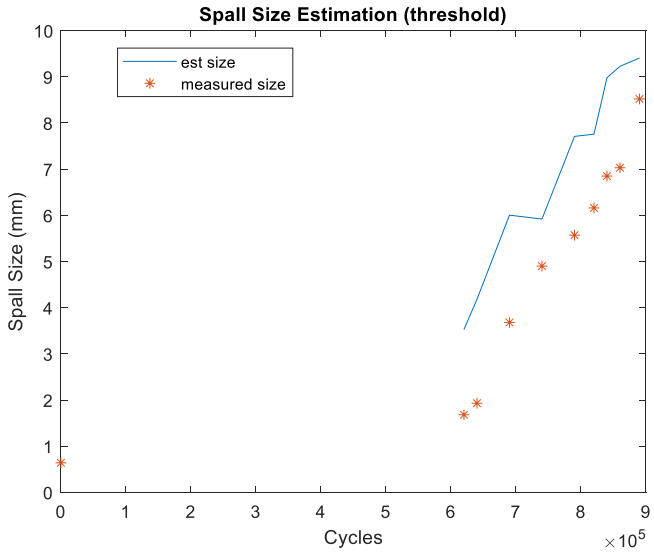


Fig. 4-11. Estimated spall size of 500 – 2000 Hz band compared to the measured size (Test 3) using handpicked threshold (0.5) for the normalised average frequency

## 4.5 Conclusion and future work

This study reviewed the current existing physical size estimation approaches for rolling element bearings, and three representative methods were rebuilt for performance comparison. A novel approach based on detecting the local stiffness variation of the bearing was proposed and compared with the previous methods. The rebuilt methods and proposed approach were applied on three sets of experimental data induced by an artificial rectangular spall and two extended spalls, and the results demonstrated the superiority of the proposed approach. The main conclusions are summarised as follows:

1. The spall induced stiffness variation of the rolling element bearing could be detected by its local natural frequency perturbation by utilising the Wigner-Ville spectrum (WVS), which overcomes the uncertainty principle limitations and interference terms of other time-frequency analysis methods. The length of local natural frequency perturbation can indicate the size of the spall.
2. The reviewed methods intending to locate the entry/exit points by identifying the characteristic entry, impact and exit events are effective for clear artificial spalls, but

they cannot recognise the weak entry/exit signals produced by an extended spall. On the other hand, the proposed method is effective for both artificial and extended spalls.

3. The proposed local natural frequency perturbation method is more effective for large spalls; it appears to be influenced by the decay length of the impact signal for small spalls.

Although the advantages of the proposed approach are seen compared to the existing spall size estimation methods, a great deal remains for future work. In this study, the averaging frequency band was selected manually around an identified natural frequency observed from the PSD. Therefore, one area for improvement is in automating the selection of the natural frequency and band width. The methodology used for the selection of the entry/exit points was based on a simple and arbitrary thresholding method. Future work should aim at developing a more rigorous and automated approach. Another improvement may lie in the experimental setup, since the floating test bearing housing used here is not typical of normal machines, which may be the reason that this approach performed better in low-frequency bands. In the future, the proposed approach should be tested on a bearing mounted on a solid base, and ideally in the presence of signal masking agents such as gears.

However, the intention of this study is not to provide a complete solution to the problem of bearing spall size estimation, but rather to put forth an alternative approach intended in particular to deliver improved performance in dealing with realistic rather than artificial spalls, and in particular to track the growth of spalls for prognostic purposes, especially as they grow larger.

## 4.6 Additional results

### 4.6.1 Comparison of results for selected cases of Test 2 and 3.

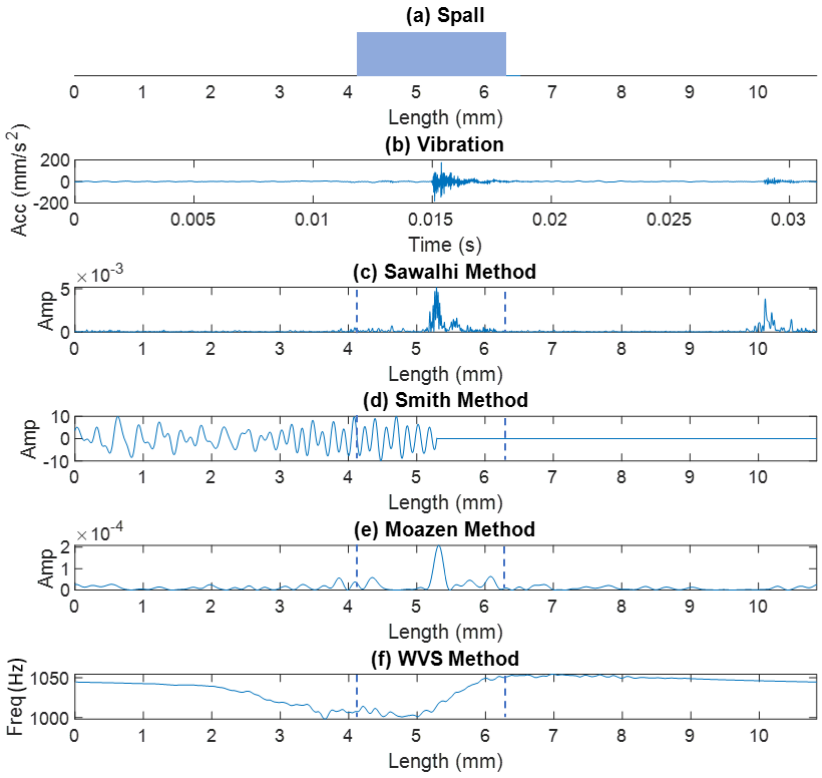


Fig. 4-12. Comparison of spall size estimation methods for Test 2 data (2.18 mm). (a) The size of extended spall; (b) The raw vibration signal, (c) Sawalhi's method to reveal the entry and impact points, (d) Smith's method (gradient), (e) Moazen's method to reveal the entry and exit points, (f) The proposed approach by using WVS

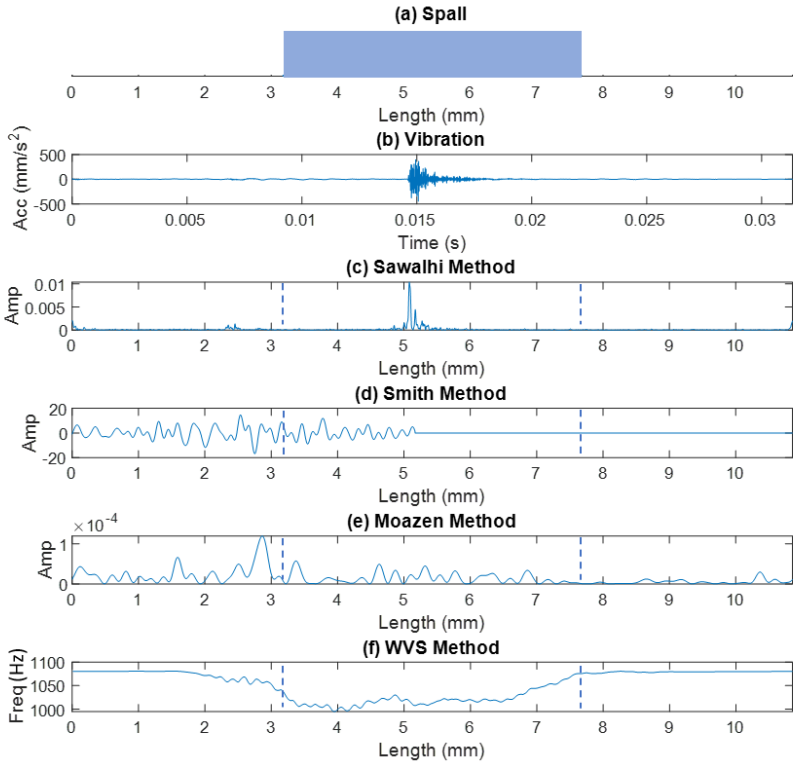


Fig. 4-13. Comparison of spall size estimation methods for Test 2 data (4.50 mm). (a) The size of extended spall; (b) The raw vibration signal, (c) Sawalhi's method to reveal the entry and impact points, (d) Smith's method (gradient), (e) Moazen's method to reveal the entry and exit points, (f) The proposed approach by using WVS

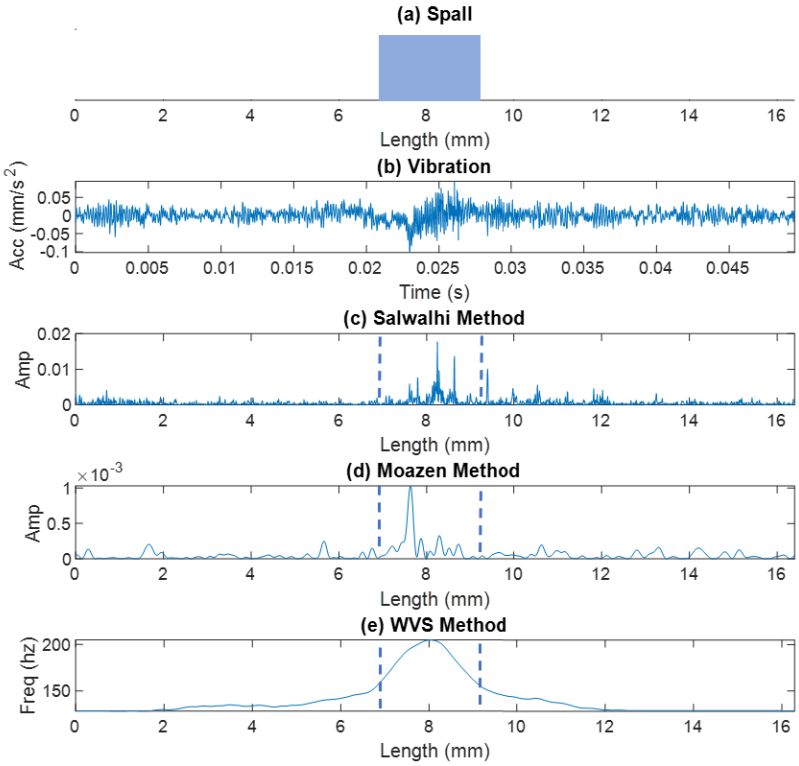


Fig. 4-14. Comparison of spall size estimation methods for Test 3 data (1.93 mm). (a) The size of extended spall; (b) The raw vibration signal, (c) Sawalhi's method to reveal the entry and impact points, (d) Moazen's method to reveal the entry and exit points, (e) The proposed approach by using WVS

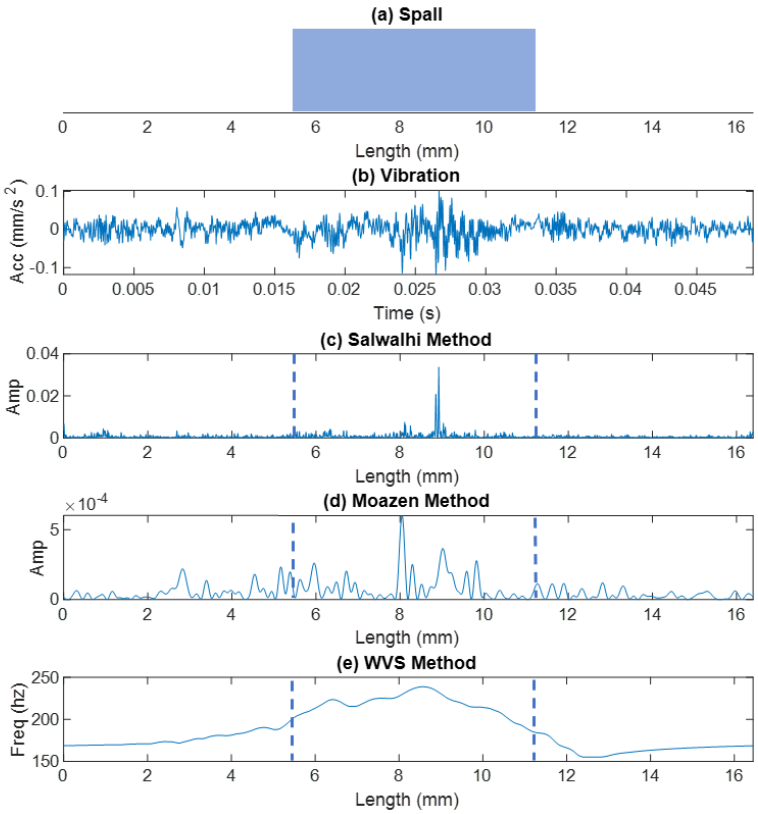


Fig. 4-15. Comparison of spall size estimation methods for Test 3 data (5.57 mm). (a) The size of extended spall; (b) The raw vibration signal, (c) Sawalhi's method to reveal the entry and impact points, (d) Moazen's method to reveal the entry and exit points, (e) The proposed approach by using WVS

### 4.6.2 Normalised WVS for different sizes and bands (Test 2 and 3).

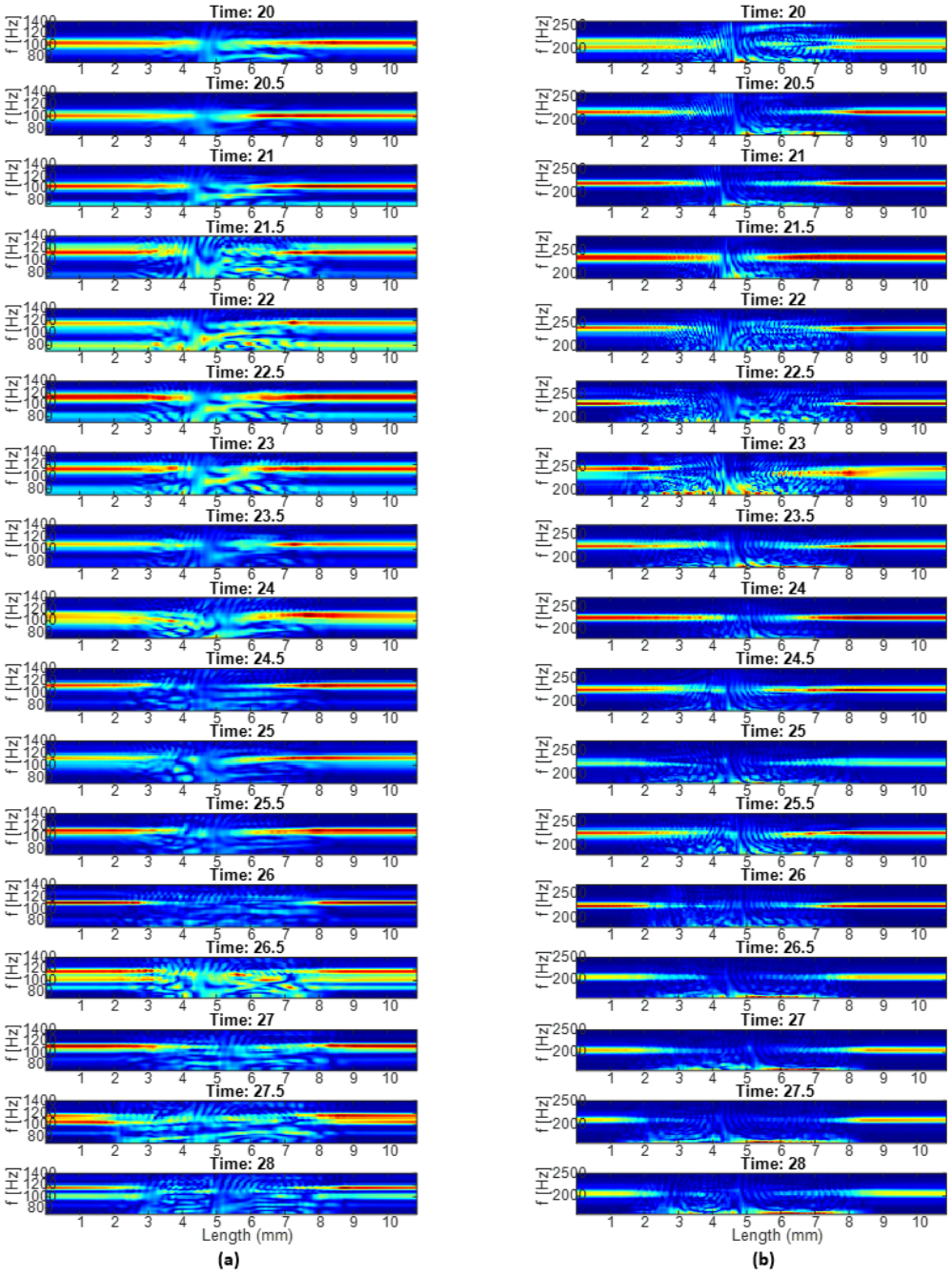


Fig. 4-16. The normalised WVS of two different frequency bands for Test 2: (a) 700 - 1400 Hz; (b) 1700 - 2600 Hz

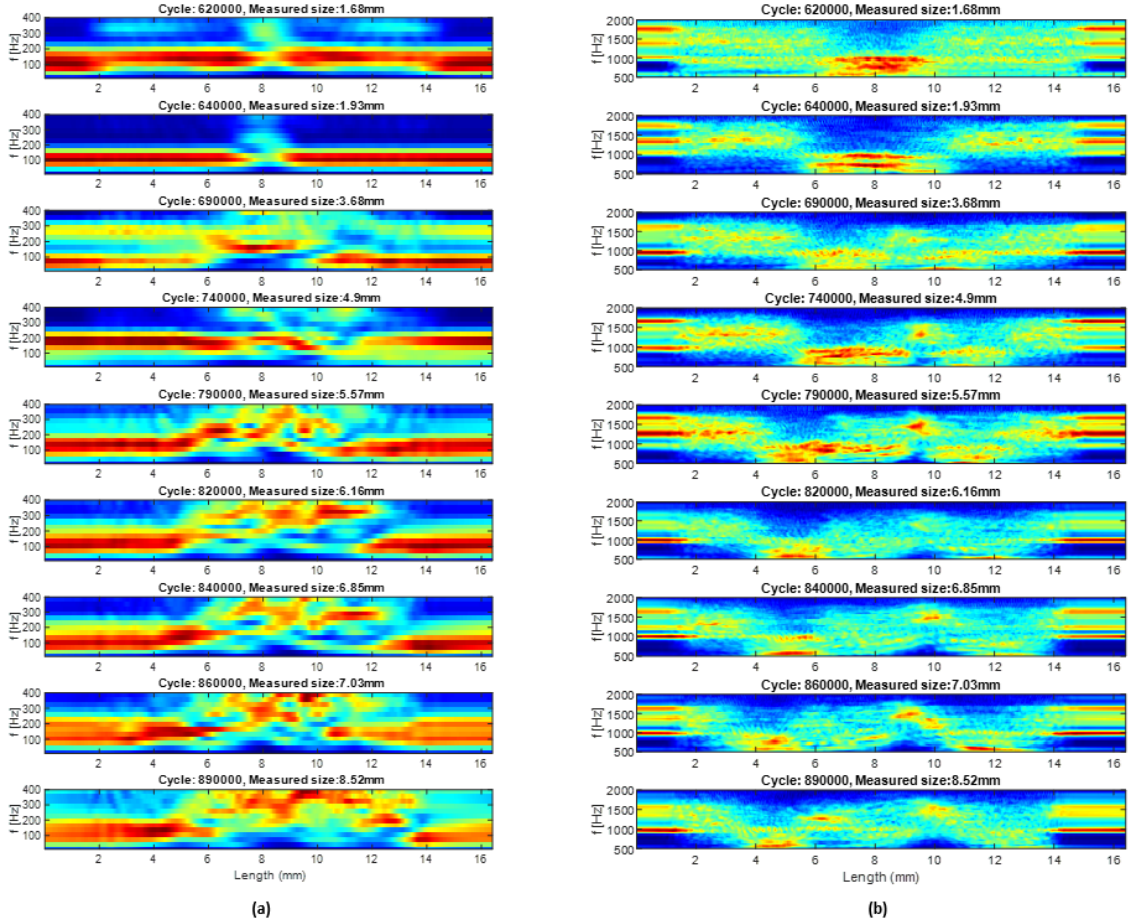


Fig. 4-17. The normalised WVS of two different frequency bands for Test 3: (a) 10 - 400 Hz; (b) 500 - 2000 Hz

# 5. Comparison of measurement approaches for tracking the natural evolution of spall severity in rolling element bearings

In Chapter 4, an effective spall size estimation approach for REBs based on accelerometer measurements was proposed. In this chapter the analysis of bearing fault severity will be extended to a series of other alternative measurements to fulfil **Objective 2**. As shown in section 2.4, most research available in literature using different measurements was conducted with individual sensors and therefore without a benchmark or comparison. In this section, by conducting bearing run-to-failure experiments with four measurement approaches (acceleration, AE, IAS, and radial load as a proxy for displacement) applied simultaneously, a comparison study of these sensors was accomplished. It was found in this study that the radial load (a proxy for displacement) was the most successful in quantifying spall size, acceleration required sophisticated techniques to be effective, IAS was successful in trending the size, but lacked an overall scaling factor, and AE showed the least reliable results.

This chapter is a modified version of the published paper "*Hengcheng Zhang, Pietro Borghesani, Robert B. Randall, Zhongxiao Peng. A benchmark of measurement approaches to track the natural evolution of spall severity in rolling element bearings, Mech. Syst. Signal Process., 166: 108466, 2022"*.[3] I contributed more than 90% of the methodology development

[3] Permission has been granted from co-authors.

and manuscript drafting. To better fit the thesis's structure, the literature review part of the original paper was merged within Section 2.4.2 and 2.4.3, and the experimental rig setup was merged within Section 3.4.1. In addition to the paper content, analysis results of extending the proposed methods to higher shaft speed data are also included at the end of this chapter.

This chapter is organised as follows. Section 5.1 briefly introduces the background of this study. Section 5.2 presents the experiments and a discussion on the load sensor acting as a proxy for displacement. The analysis results of the experimental data are presented in Section 5.3. Discussions and conclusions are found in Section 5.4 and Section 5.5, respectively. The results of testing the proposed approaches on higher speed are given in Section 5.6.

## 5.1 Introduction

As already discussed in Chapter 3, most of the existing public bearing prognostic datasets have the limitation that they only provided at most a single fault-size measurement at the end of the run-to-failure test. Without the measurement of the actual spall size during the experiment, a solid relationship between the developed indicators and the physical fault severity of a bearing cannot be established. To overcome this shortcoming, new run-to-failure experiments, which included a regular disassembly of the test bearing to measure the spall size as it evolved, were conducted in this thesis as presented in Section 3.4.1.

Another limitation of the prior studies is that the performance of different sensors in bearing fault severity estimation has not been systematically compared, although there are some limited researches conducted between AE and acceleration [164], [203], [204], and between IAS and acceleration [9], [171].

Four different types of sensors (two accelerometers, an AE sensor, an encoder, and a load cell) were used in our run-to-failure tests. By comparing commonly used indicators extracted from these signals with the measured spall size, a benchmark comparison of these measurement approaches for bearing fault severity trending was obtained. A note must be immediately made with respect to the interpretation and physical nature of the radial load measurements. Due to the particular setup of the rig, and the installation layout of the force sensor, load should be interpreted in this study as a proxy for relative displacement between the bearing housing and

the rotor. This is caused by the fact that the equivalent stiffness of the loading mechanism dominates the response of the force sensor, resulting in a force that is related to displacement. This characteristic is seen as an advantage since it allows comparing the results of this work with recent publications [8], which mentioned the potential of displacement in bearing diagnostics.

## 5.2 Experiments and interpretation of radial load as a proxy for displacement

The experiments have been presented in Section 3.4.1, and four sets of them are used in this chapter. For the reader's convenience, they are summarised here again in Table 5-1.

Table 5-1. Experiments for comparison study of measurements

| No. | Defect Position | Seeded Defect Size (mm) | Radial Load (kN) | End cycle (k) | End spall size (mm) |
|---|---|---|---|---|---|
| Test 1 | Outer race | 1.0 | 10.5 | 350 | 6.7 |
| Test 2 | Outer race | 1.0 | 7 | 2000 | 6.3 |
| Test 3 | Outer race | 0.5 | 10.5 | 600 | 8.6 |
| Test 4 | Inner race | 0.5 | 10.5 | 1670 | 6.3 |

As seen from the experimental setup in Section 3.4.1, the outer race of the test bearing was mounted in a floating housing, and it was loaded by the hydraulic system in the radial (horizontal) direction. During the experiment, we noticed from the load cell data that the radial load decreased when one ball fell into the spalling zone, as shown in Fig. 5-1 (b). This means that in such a circumstance the bearing outer race (bearing housing), moved away from the load application point and released the loading rod slightly. This behaviour can be compared to Fig. 5-1 (a), which shows the displacement of the bearing housing in the radial (horizontal) direction, obtained by double integration of the acceleration (thus without the true DC value). The maximum displacement due to a ball falling into the spalling zone is about 18 μm. The following paragraphs are aimed at showing that the assumption of a direct load-displacement relationship is suitable for this test-rig.

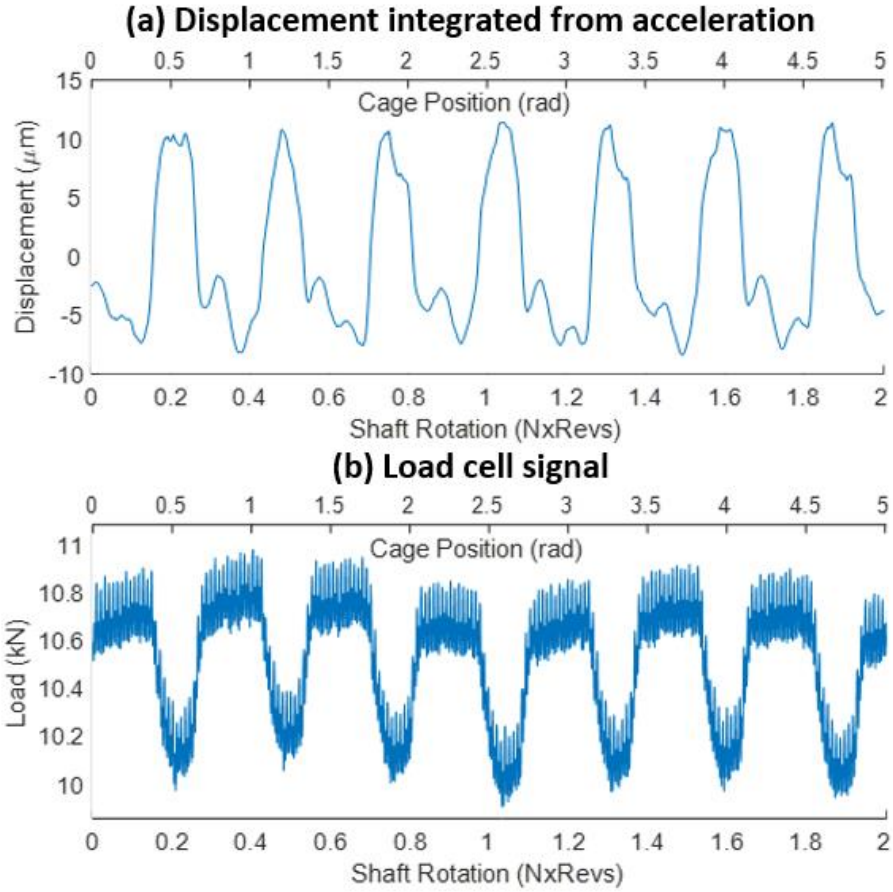


Fig. 5-1. Radial load and housing displacement at the end of Test 1: (a) housing displacement by double integration of the accelerometer signal, (b) radial load acquired from the load cell

If the radial position of the shaft (inner race) is deemed constant (a reasonable assumption in this system due to the high stiffness of the shaft and support bearings), the displacement of the housing (outer race) is equal to the deflection of the rolling elements and races. The relationship between load and deflection was studied by Harris in [1] by providing a model of the REB stiffness, which was further developed by Sawalhi et al. and Petersen et al. in [11], [52] to simulate bearings with spalls on the raceway. The main idea is that for a certain radial deflection between inner and outer race, the deformation of each rolling element around the bearing could be calculated according to its position, and the roller-raceway contact force could be obtained sequentially based on a non-linear stiffness model. The total applied radial load is then equal to the sum of the same direction components of the roller loads. It is important to highlight that a dynamic simulation of the bearing behaviour as in [11], [52] is outside the

scope of this section, which assumes that the relatively low operating speed and the configuration of the system result in a quasi-static behaviour of the bearing, which is considered as a simple non-linear flexible element. The following is a quick summary of the methodology adopted to validate this assumption, with details to be found in [1].

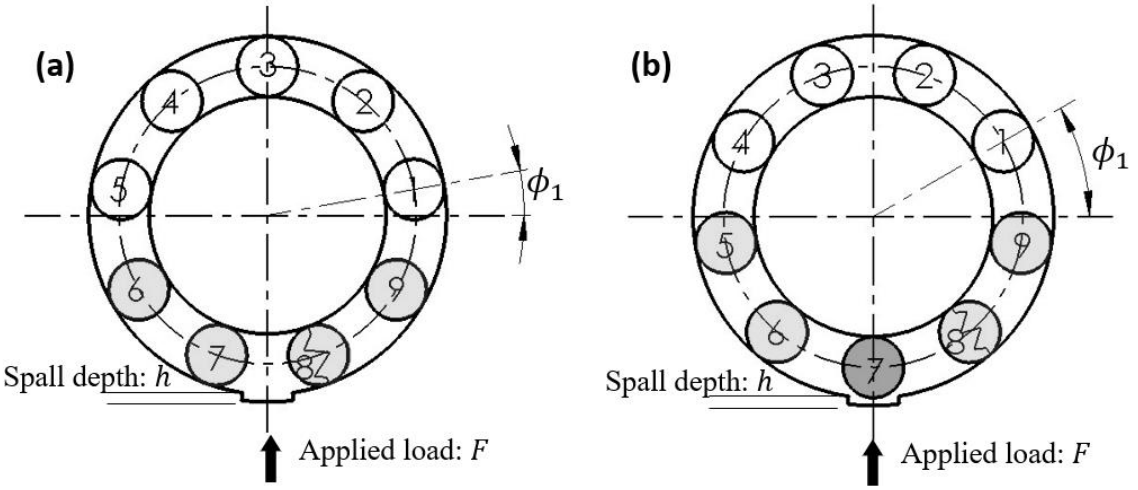


Fig. 5-2. Bearing with spall on the outer race: (a) no ball is in the spall zone, (b) one ball falls in the spall zone

The computation of load starts with the definition of two kinematic quantities: a relative radial displacement $x$ between the two races and a cage position angle $\phi_1$, representing the angular position of a reference ball (ball 1 in Fig. 5-2) with respect to the horizontal. Based on these two quantities, pure geometrical considerations (Fig. 5-2) allow the computation of the deformation $\delta_j$ of each ball at its angular position $\phi_j = \phi_1 + 2\pi(j-1)/N_b$ (neglecting jitter)

$$\delta_j(x, \phi_1) = x \sin(\phi_1 + \frac{2\pi}{N_b}(j-1) - \pi) - r_L - d(\phi_1 + \frac{2\pi}{N_b}(j-1)) \qquad (5\text{-}1)$$

where $N_b$ is the number of rolling elements and $r_L$ is the radial clearance. The defect depth $d$ at the ball angular position was set to zero when the ball is outside the spall and, for simplicity to $h = 50$ $\mu$m when the ball is inside the spall. This quantity, as well as the spall length of 6.7 mm was obtained from Fig. 3-5 (c), using the average depth as a constant $h$. The force on each ball is proportional to the 3/2 power of its deformation, and is given by

$$F_j = K_n \gamma_j \delta_j^{3/2} \qquad (5\text{-}2)$$

where $K_n$ is a bearing-specific factor dependent on materials and bearing geometry and $\gamma_j$ is a saturation coefficient, equal to 1 when $\delta_j > 0$ (rolling element in compression) and 0 otherwise (no reaction from the rolling element when the gap between the races is larger than its diameter). Then the applied load should be equal to the sum of the force on each ball, projected in the load direction

$$F = \sum_{j=1}^{N_b} F_j \sin(\phi_j - \pi) \tag{5-3}$$

This enabled the establishment of a displacement-load relationship $F(x, \phi_1)$, which was then used in two ways to validate the displacement-like interpretation of experimental load measurements.

First of all, the case of no spall contact ($\phi_1 = 10°$ configuration as in Fig. 5-2(a)) was analysed. Based on a load of ~10.7 kN observed in Fig. 5-1 for the centre of the no-spall area (expected to be around $\phi_1 = 10°$), the inversion of the relationship $10.7\ \text{kN} = F(x, 10°)$ yielded an estimate of $x_H = 64$ µm for the unknown absolute displacement of the bearing in healthy conditions.

Then, this deflection was combined with the measurement of Fig. 5-1 (a) shifting the no-spall-contact area to a value of $x_H = 64\ \mu$m and resulting in the estimated absolute displacement profile $x(\phi_1)$ as the red dotted line in Fig. 5-3(a). Because of the inaccuracy and fluctuation of the acceleration derived displacement, a square wave was used to replace it as the blue line in Fig. 5-3(a), which was used again in equations (5-3) to compute the expected load $F(x(\phi_1), \phi_1)$ of Fig. 5-3(b). Despite the approximations adopted for simplicity, the match of the actual load measurement of Fig. 5-1 (b) and the one shown in Fig. 5-3(b) confirms that the quasi-static assumption is appropriate and that the non-linear bearing relationship between displacement and load is valid.

In the rest of this chapter, we will therefore treat load as a proxy measurement for displacement. This is in no way a general consideration, and it is only valid thanks to the specific layout of this test-rig. For this reason, we will treat the load measurement together with the acceleration measurement, considering it an indirect effect of displacement.

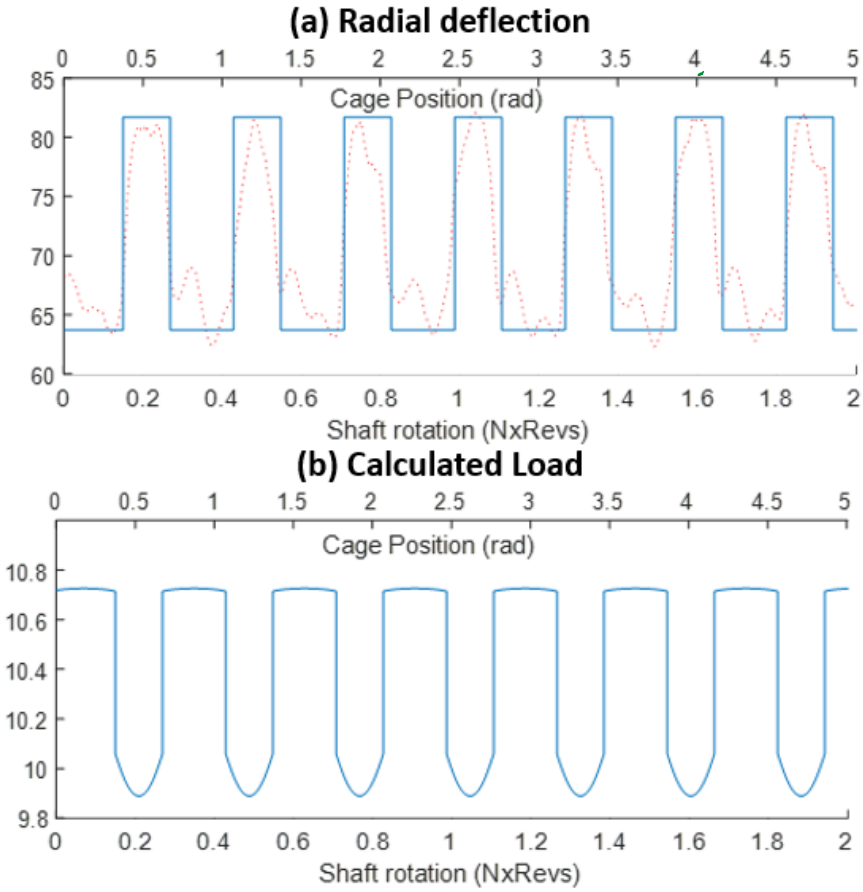


Fig. 5-3. Relationship of load and radial deflection: (a) the radial deflection, the red dotted line is the shifted displacement from accelerometer, the blue line is the simplified radial deflection, (b) the calculated radial load

## 5.3 Results

Results of the bearing fault severity analysis for 4 different measurement techniques (acceleration, radial load as a proxy of displacement, AE, and IAS) are presented in this section, and representative methods from those reviewed were selected for different sensors.

### 5.3.1 Acceleration

To provide a first qualitative idea of the evolution of the acceleration measurements, the order tracked accelerometer signals for different spall sizes along Test 1 are presented in Fig. 5-4. Their spectra and squared envelope spectra (SES) are presented as well since they are both indicative to the bearing fault for this rig. The ball-passing-spall bursts are clearly shown in the angular-domain acceleration signal, and their amplitude and duration grow larger in the first

phase of spall growth. However, when the spall size exceeds 3.5 mm, the amplitude stops growing, while their duration is difficult to assess. The non-monotonic relationship between spall size and acceleration amplitude is likely due to the importance of the topography of the naturally developed defect, whose profile evolves in time, e.g., smoothing of crests. The ball pass frequency outer (BPFO) and its harmonics can be identified from both spectrum and SES since the beginning because of the high signal-to-noise ratio of the acceleration signal. They are not visible in the first row just because of the linear scaling, which is kept the same with the below ones to enable an easy quantitative comparison.

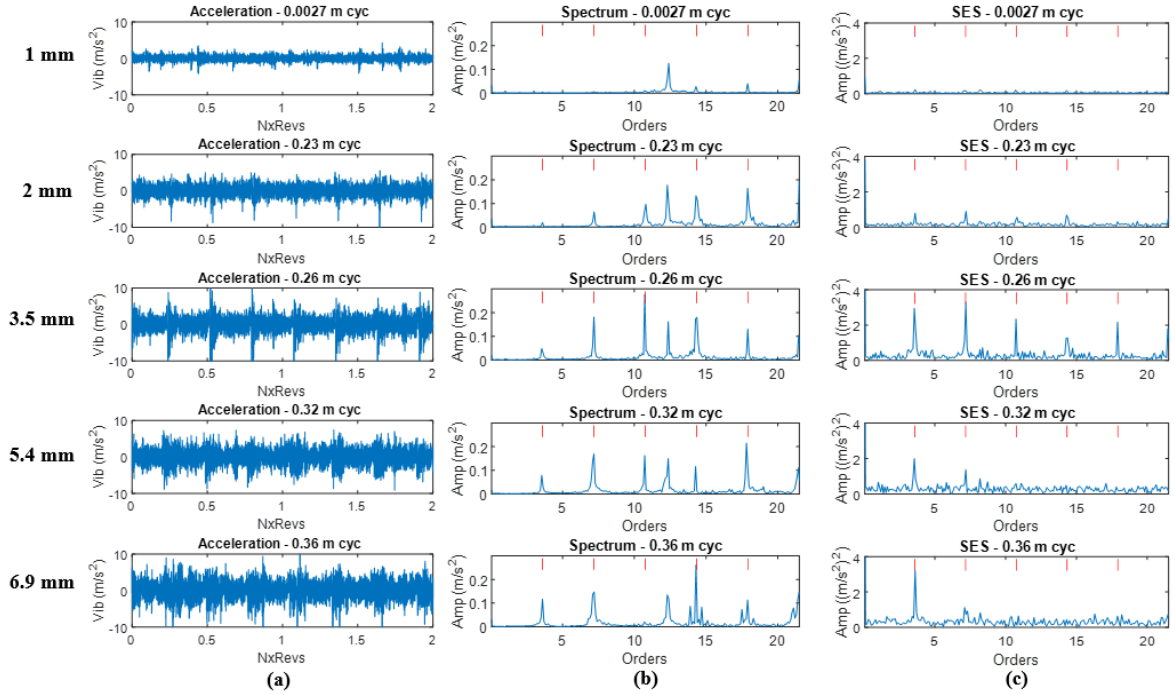


Fig. 5-4. Comparison of acceleration signals for different spall size in Test 1: (a) order tracked acceleration, (b) spectrum, (c) SES

RMS is a simple and commonly used indicator, and it is almost always present in most data-driven prognostic studies. Another commonly used indicator is the amplitude of the first BPFO harmonics in the SES. Due to the asynchronous and pseudo-cyclostationary nature of the signal the SES is often integrated over a narrow band around the BPFO rather than just using the peak value (in this case including 5 spectral lines before and after the peak) [89]. By using root squared sum of the selected lines, it compensates for both picket fence effect and smearing due

to slip. The trends of RMS and SES amplitude are shown in Fig. 5-5, in comparison with the evolution of the spall size.

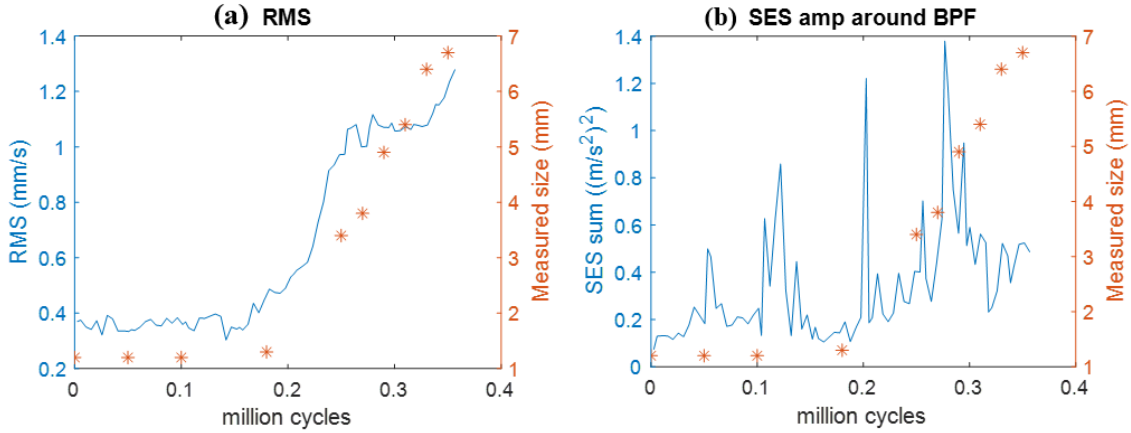


Fig. 5-5. Indicators to trend the growth of spall size: (a) RMS value, (b) root squared sum of the SES lines around BPFO

Despite following an overall increasing trend, RMS does not grow monotonically and shows a flat portion after 0.25 million cycles (spall size >3.5 mm), confirming the qualitative observation on the overall magnitude of the signal in angular domain (Fig. 5-4, left column). The SES amplitude of the BPFO displays large fluctuations, and it is not monotonic vs the spall size as also shown qualitatively in the SES diagrams in Fig. 5-4.

As reviewed in Section 2.1, if a direct quantification (rather than just trending) of the spall size is to be obtained, an entry-exit approach is to be adopted. As shown in a recent study [14], relying on two single events (entry and exit) is often difficult with natural spalls, where geometries are irregular. Based on previously proposed models [11], study [14] proposed instead to focus on the stiffness variation at the roller-passing-spall zone, and therefore on the duration of the corresponding perturbation of the system's natural frequencies. The Wigner-Ville Spectrum (WVS), which is a time-frequency analysis method exhibiting high resolution in both time and frequency domain, was utilised to reveal this perturbation, and its duration was found to be in accordance with the measured spall length. This method, applied to Test 1, yielded the result of Fig. 5-6. As reported in the original publication, this method shows little

effectiveness for small spalls (below 1.5-2.0 mm) because the natural frequency perturbation phenomenon is too short-lived, but then provides accurate estimates of larger spall size.

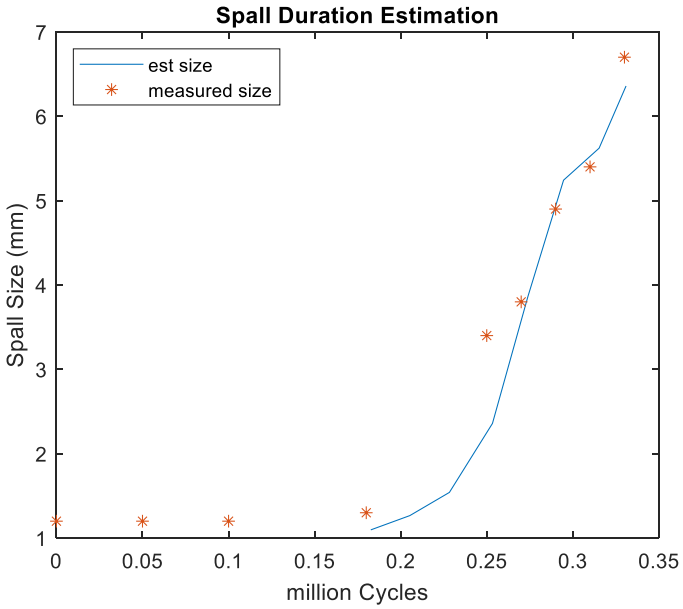


Fig. 5-6. Results of the spall size estimation approach by natural frequency perturbation [14] for acceleration signal

Comparing Fig. 5-6 with Fig. 5-5, it is clear that the two approaches show a strong complementarity, with RMS and SES showing early detection and trending of the fault, while the natural-frequency perturbation method enables quantifying spall size thereafter.

The same procedures were also applied to data of Test 2, Test 3, and Test 4 to validate the first analysis. Their results are illustrated together in Fig. 5-7, and similar situation can be found in RMS, SES as well as the more sophisticated spall-size estimation method. For data of Test 4 with inner race defect, since it is amplitude modulated at shaft frequency, only the ball-passing-spall instances with high energy were selected for the spall duration estimation as indicated in [14]. Despite similarities in the trends, it is important to highlight that only the natural-frequency perturbation approach has a result which directly quantifies the spall in microns, whereas all other indices result in non-scaled trends. RMS and SES have scale factors which are machine-specific and known to be affected by operating conditions and other components, thus requiring pre-processing and calibration.

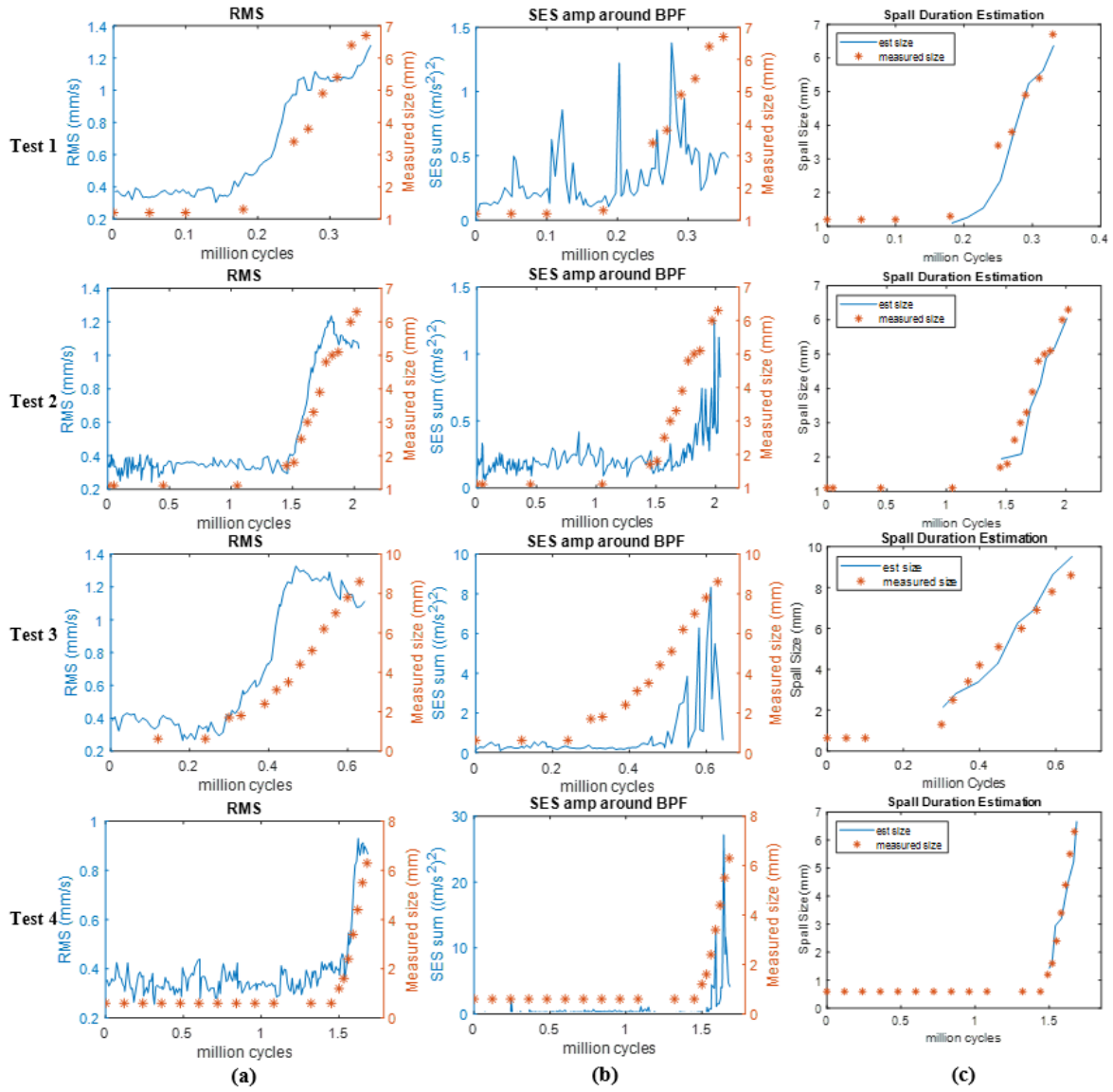


Fig. 5-7. Comparison of acceleration indicators for different tests: (a) RMS value, (b) root squared sum of the SES lines around BPFO/BPFI, (c) spall size estimated by the natural frequency perturbation

### 5.3.2 Radial load as a proxy of displacement

As discussed in Section 3, the load cell signal is analysed here as a proxy of the displacement of the bearing housing in radial (horizontal) direction. Their waveforms for different bearing spall sizes are shown in the left column of Fig. 5-8. It is easily seen that there is a cyclic load decrease corresponding to the roller-fault contact, and the duration of these perturbations increases with the spall growth. To highlight this phenomenon, a 15 – 300 Hz band pass filter

was applied, removing low-frequency shaft-synchronous harmonics and high frequency noise. The filtered signals are plotted in the second column of Fig. 5-8, and their spectra are shown in the last column. For the load signal, the high frequency components are not useful as in acceleration and AE, since it is in the spring-controlled region below resonance; therefore, the envelope analysis was not applied to it.

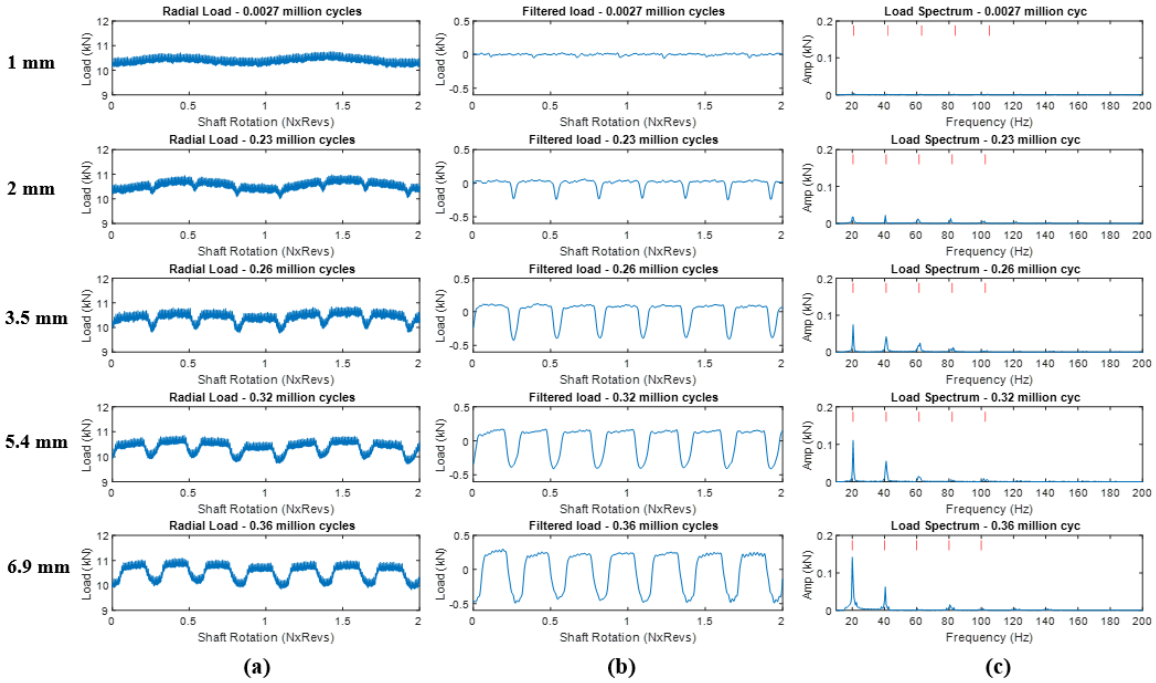


Fig. 5-8. Comparison of radial load signals of different spall sizes in Test 1: (a) raw radial load cell signal, (b) band pass filtered load signal, (c) spectrum of the filtered load signal

Fig. 5-8 already qualitatively shows that the duration of the load perturbation is related to the spall size. Therefore, the time duration was extracted by setting a threshold (-0.03 kN in this case) to the filtered load, and then substituted into the following expression from [45] to derive the spall size in mm:

$$l_{spall} = \frac{\pi f_r \left(D_p^2 - d^2\right)}{2D_p} t_{diff} \tag{5-4}$$

where $t_{diff}$ is the duration of the load perturbation, $D_p$ is the pitch diameter of the bearing, $d$ is the roller diameter, and $f_r$ is the shaft frequency. This calculation was repeated independently for each perturbation within a load signal.

The results of this approach are shown in the last column of Fig. 5-9. The blue line denotes the mean estimated size (across all perturbations), and the error bar shows the standard deviation of each estimation. It can be seen that the estimates follow the actual spall size very well with a narrow confidence interval. For Test 4 with inner race defect, the displacement is amplitude modulated at shaft frequency, and the fluctuation caused by small defect (less than about 1.5 mm) is too vague to be seen.

Fig. 5-8 also shows that the perturbations not only increase in width, but also in amplitude along with the spall growth. Therefore, the amplitude indicators such as RMS, peak-peak could be used to trend the spall size. Since the filtered load signal was dominated by the BPFO component as shown in the last column of Fig. 5-8, the RMS was expected to give similar trend as the amplitude of BPFO in spectrum. Their results are both shown in Fig. 5-9. The trending performance of BPFO amplitude is slightly better than RMS, and neither of them is as good as the duration approach.

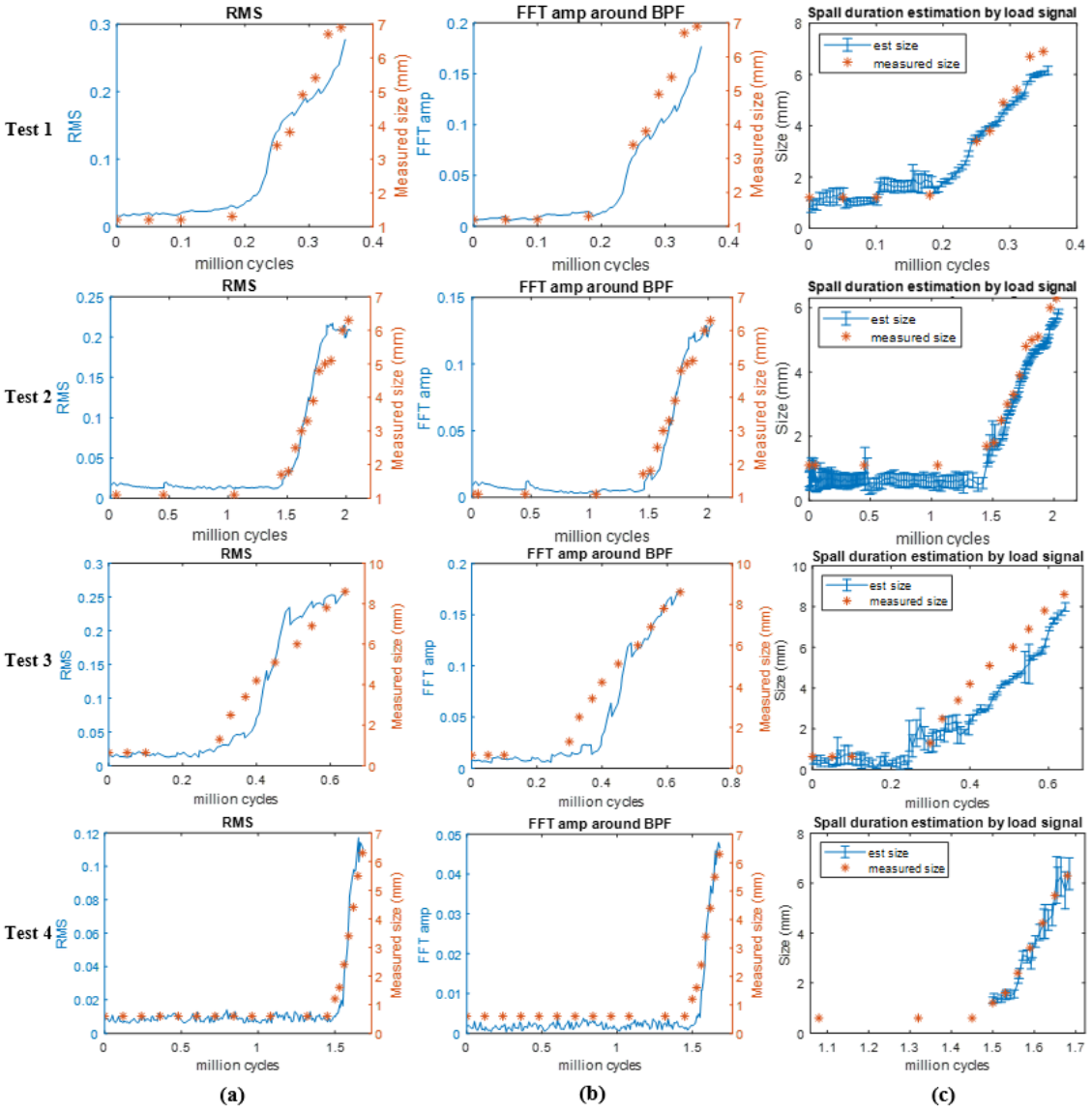


Fig. 5-9. Comparison of the load trend indicators for different tests: (a) RMS, (b) BPFO/BPFI amplitude, (c) estimated spall size

The displacement of the bearing housing could also be obtained by integrating the acceleration twice, and the results should be similar to that from the load cell, as already shown in Fig. 5-1. Therefore, the same spall duration estimation method for the load cell was applied to the acceleration converted displacement as well, and the results are compared with those from the load cell in Fig. 5-10. It is noticed that their results have similar mean estimated sizes, while the plots of the load signal have smaller standard deviations, especially for small spalls, which

may indicate that the load cell is a better displacement proxy than the accelerometer in this case.

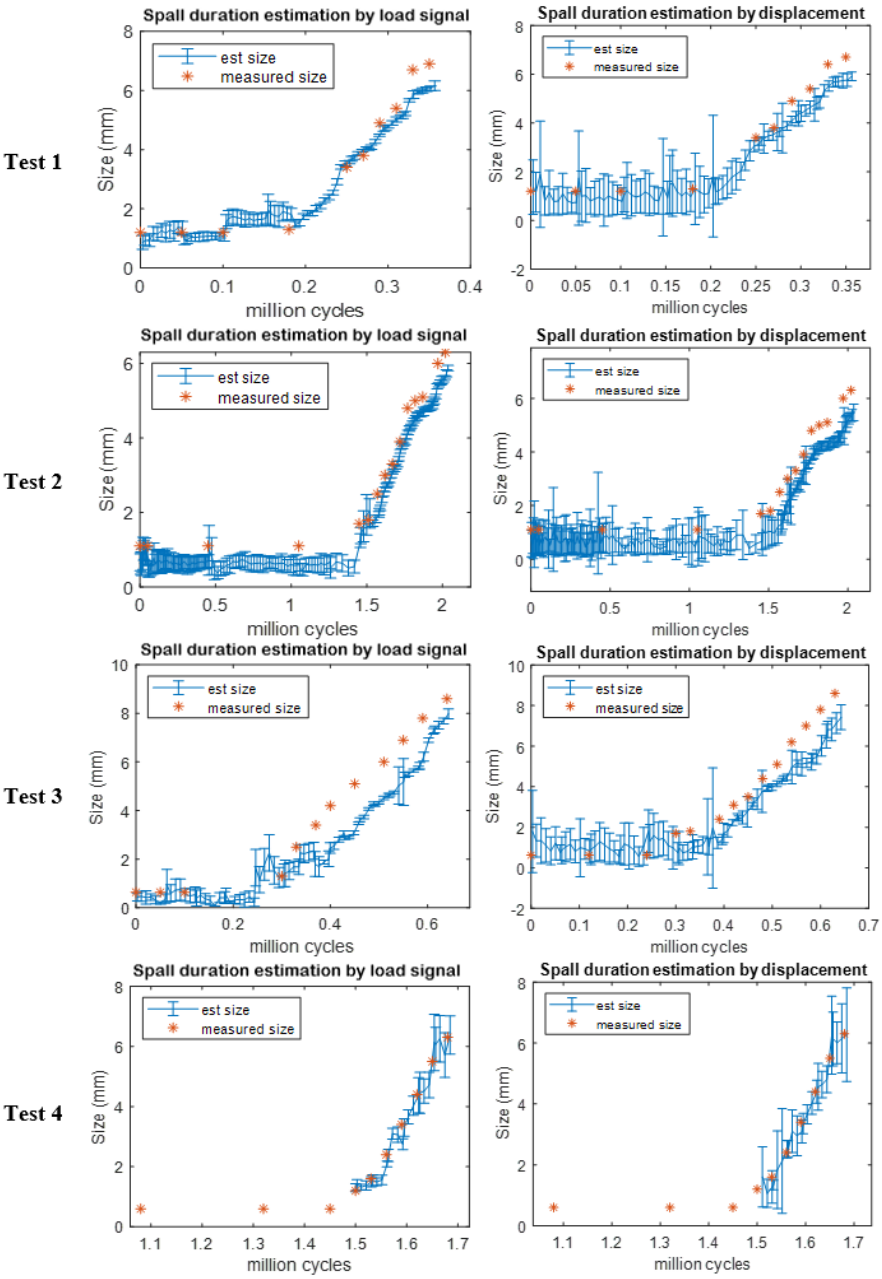


Fig. 5-10. Comparison of spall duration estimation by using bearing housing displacement: (left) from load signal, (right) derived from acceleration.

### 5.3.3 Acoustic emission

As reviewed in Section 2.2, the signal processing methods for AE signals are quite similar to those for acceleration signals, except for the frequency range of interest. Therefore, similar procedures to those in Section 4.1 were applied to AE.

The order-tracked AE signals from Test 1 together with their squared envelope spectra (SES) are illustrated in Fig. 5-11 to provide a visual expression. Although some researches [159], [161] reported that the duration of AE bursts could be utilised to estimate the spall size, this phenomenon was not found in our experiments as seen from the first column of Fig. 5-11. The natural frequency perturbation method was also applied to the AE signal, but it could not yield any significant result either. The insensitivity of AE carrier frequencies to faults can be expected, since the spectrum of the AE signal is expected to be dominated by sensor characteristics, and an example of the absence of any trend is reported for completeness in Fig. 5-12.

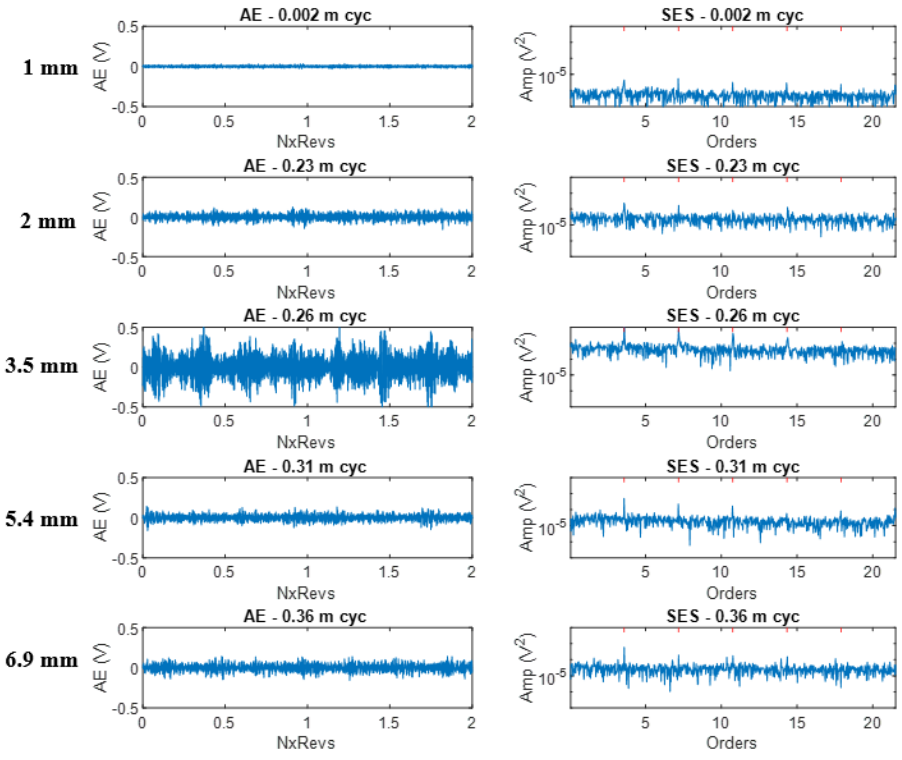


Fig. 5-11. Comparison of AE signals of different spall sizes in Test 1: (left) raw AE signal, (right) SES.

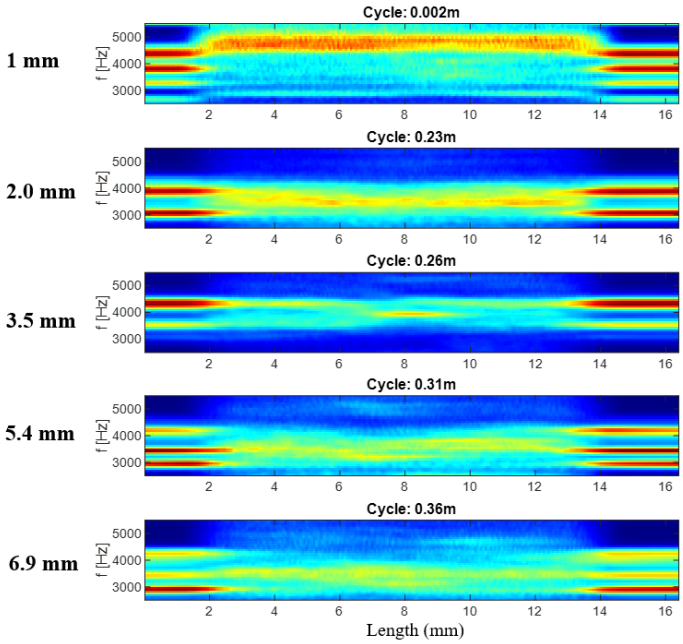


Fig. 5-12. Normalised Wigner-Ville Spectrum (WVS) of the AE signal

As shown in Fig. 5-11, the amplitude of AE increased in the initial stage of the degradation (1 mm to 3.5 mm of spall size) and then decreased afterwards, thus showing an unclear correlation with spall size and rather suggesting a possible dependency on other surface parameters, as shown in a similar study for gears [205]. The BPFO component and harmonics are also visible in the SES for the AE signal. The overall trends of RMS and SES amplitude at BPFO (with the same narrow band as for acceleration) are plotted in Fig. 5-13. It is obvious that their trends are non-monotonic and consistent with the observations already made based on Fig. 5-11.

The trends of Test 2, Test 3 and Test 4 are shown in Fig. 5-13 for validation. They confirm that AE-based indicators are not monotonic with spall size, and hence not suitable for bearing prognostics. It should be noted that the frequency fluctuations shown in Test 2, Test 3, and Test 4 are likely due to temperature changes between the start and stop of a single run of the rig, required for disassembly and spall size measurement. The increase of RMS in the beginning of spall growth may reveal that the AE signal is correlated with the morphology of the spall rather than its total length.

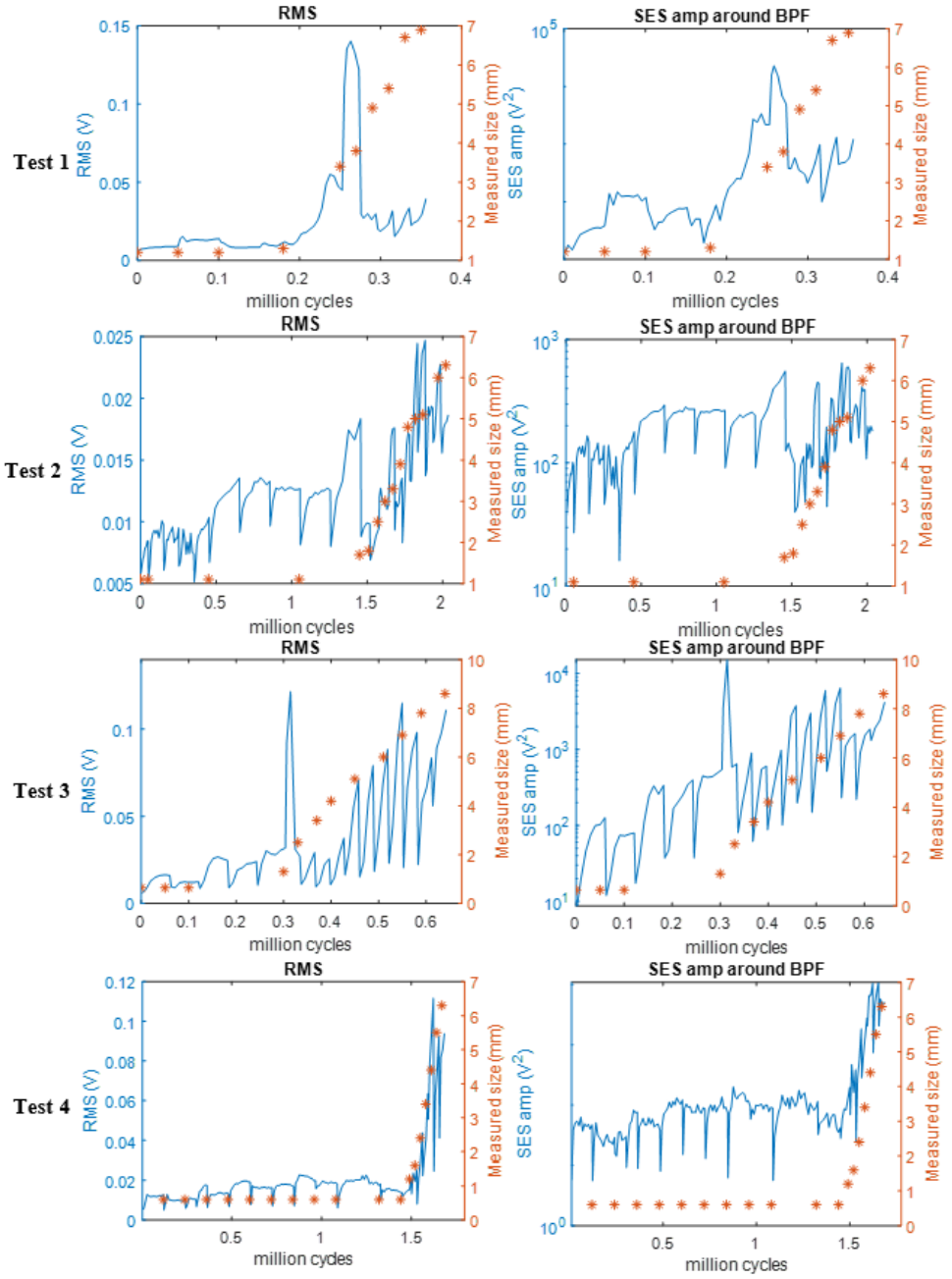


Fig. 5-13. Comparison of the AE trend indicators for different tests: (left) RMS value, (right) root squared sum of the SES lines around BPFO/BPFI

### 5.3.4 Instantaneous angular speed

The IAS signal in this section was based on our 1024 pulses per revolution encoder and 51.2 kHz sampling rate, and it was calculated using Feldman's method [168] as in Eq. (2-3). As for

the previous sections, the IAS of different spall sizes together with their spectrum and SES are illustrated in Fig. 5-14. The IAS signal was high pass filtered above 10 Hz to remove the DC component to bring the signal to zero mean, and to eliminate the fluctuations in shaft frequency, similarly to the procedure discussed in ref. [171]. An alternative method for the same task would be synchronous averaging of the IAS signal over shaft revolution periods, which has been tested with very similar results.

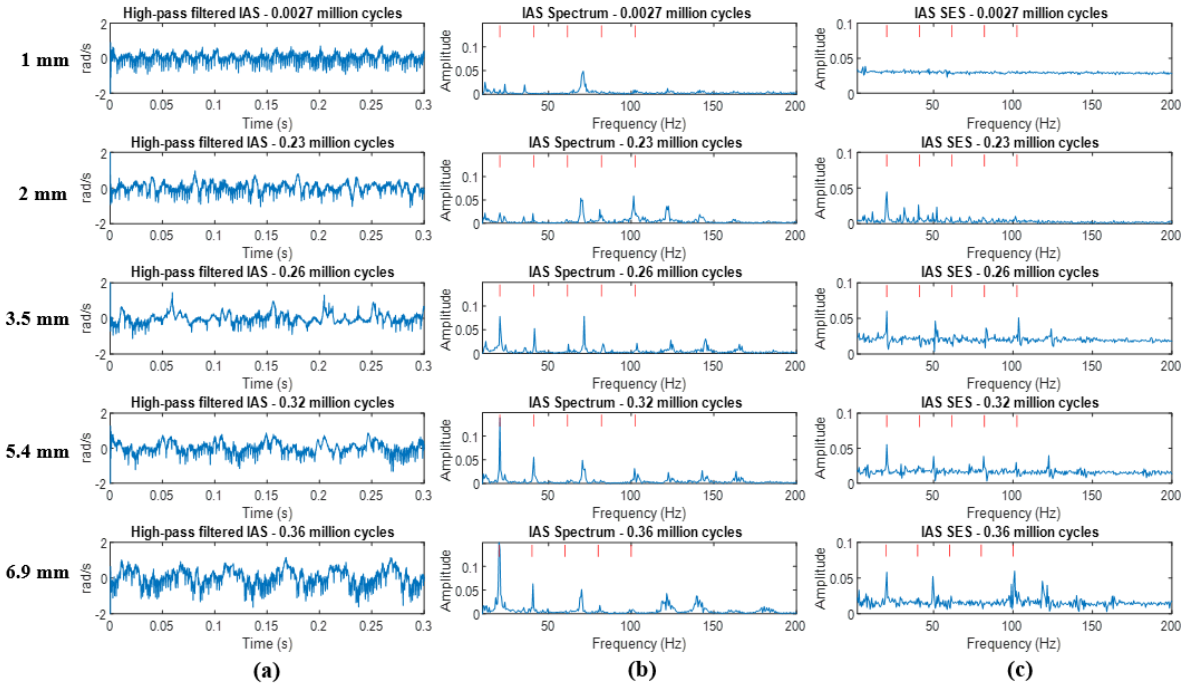


Fig. 5-14. Comparison of IAS signals of different spall sizes in Test 1: (a) high pass filtered IAS signal, (b) spectrum of IAS, (c) SES of IAS

By observing Fig. 5-14, it is found that the overall amplitude of the IAS did not increase significantly with the spall size, however, the amplitude of the first BPFO frequency component in the spectrum demonstrated a monotonically growing trend.

The RMS values, amplitudes of the BPFO component in the spectrum and SES through the whole time for all four tests are plotted respectively in Fig. 5-15. It was found that the spectral

amplitude at the BPFO provides better spall-size trending than RMS value and SES amplitude.

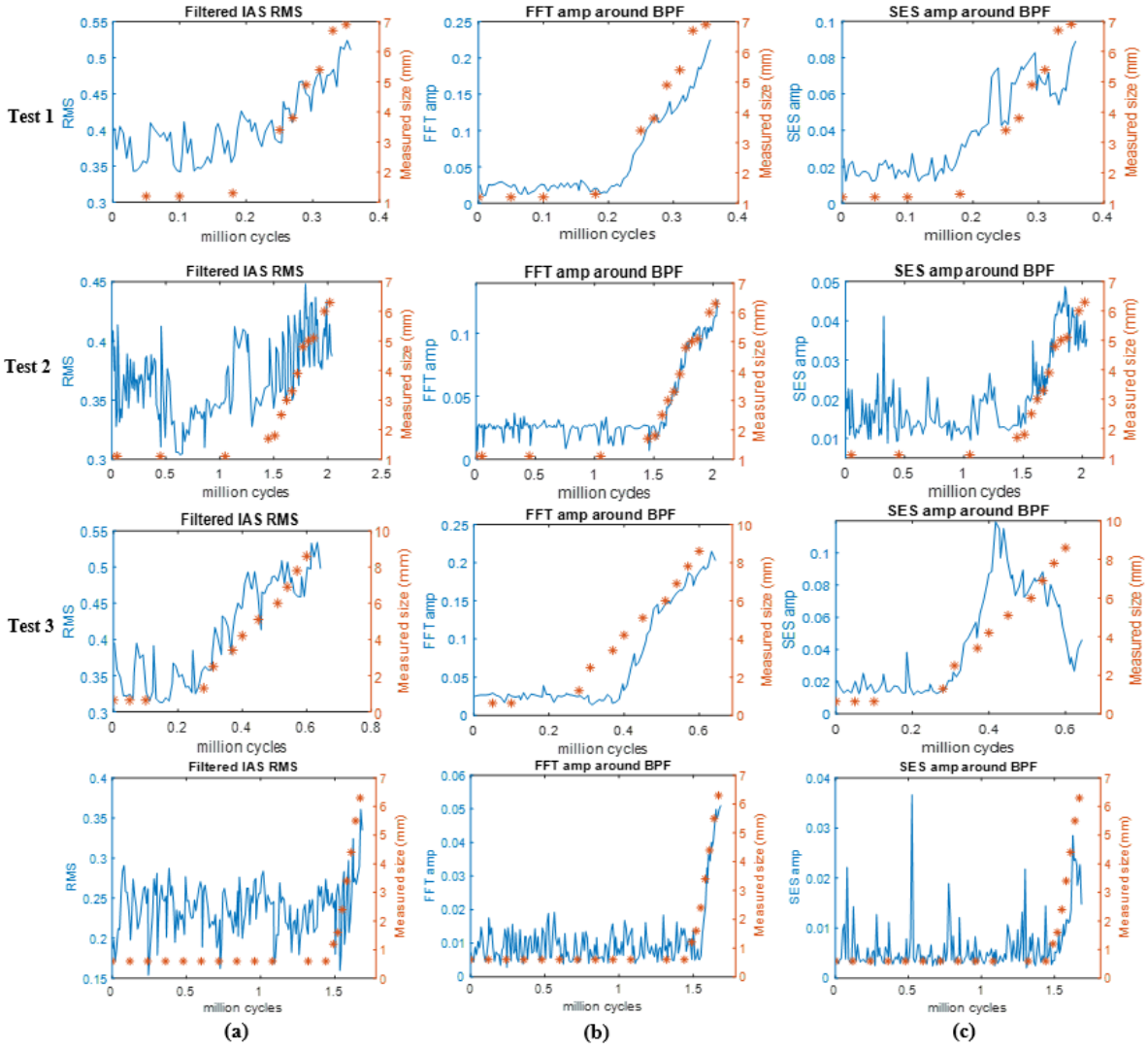


Fig. 5-15. Comparison of the IAS trend indicators for different tests: (a) RMS of filtered IAS, (b) BPFO/BPFI amplitude on the spectrum, (c) BPFO/BPFI amplitude on the SES

As discussed in Section 2.3, quantitative methods for the identification of spall size were proposed also using the IAS signal. The approach presented by Bourdon et al. [171] was to collect the first few harmonics of the ball pass frequency in the spectrum and inverse transform to time domain to observe the duration of the spall size. The application of this method to our experimental data yielded the results shown in Fig. 5-16. It can be seen from the right column of the figures that the spall duration is getting longer, but it is not as obvious as in Bourdon et

al.'s previous study. In the absence of an established way to automate this approach, it was not possible to apply it to all data points to trend the spall growth.

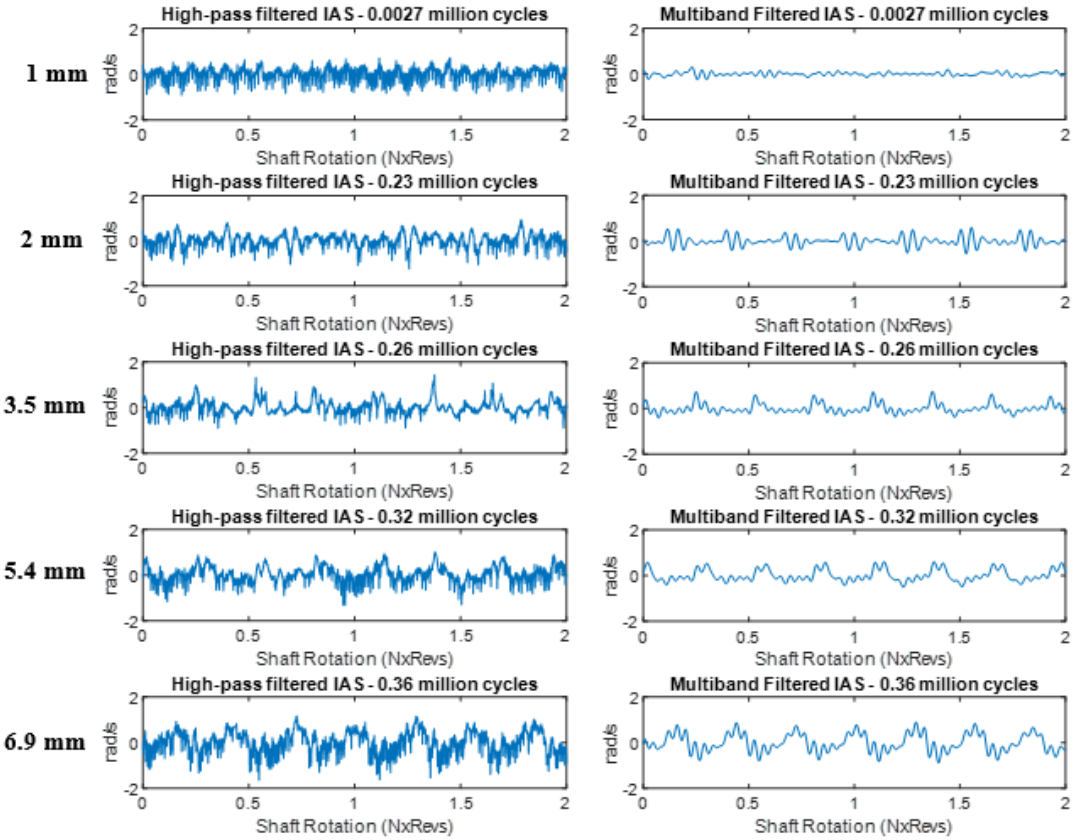


Fig. 5-16. Spall duration analysis of the IAS signals for different spall sizes in Test 1: (left) high pass filtered IAS signal, (right) multiple narrow band pass filtered IAS signal

The natural frequency perturbation method was also applied to the IAS signal, and the results are shown in Fig. 5-17. It can be seen from both the Wigner-Ville Spectrum in the left column and average natural frequency from the right column that the natural frequency perturbation only started to be effective when the spall size is larger than 3.5 mm (i.e., later than for acceleration). The trending results of this approach are shown in Fig. 5-18.

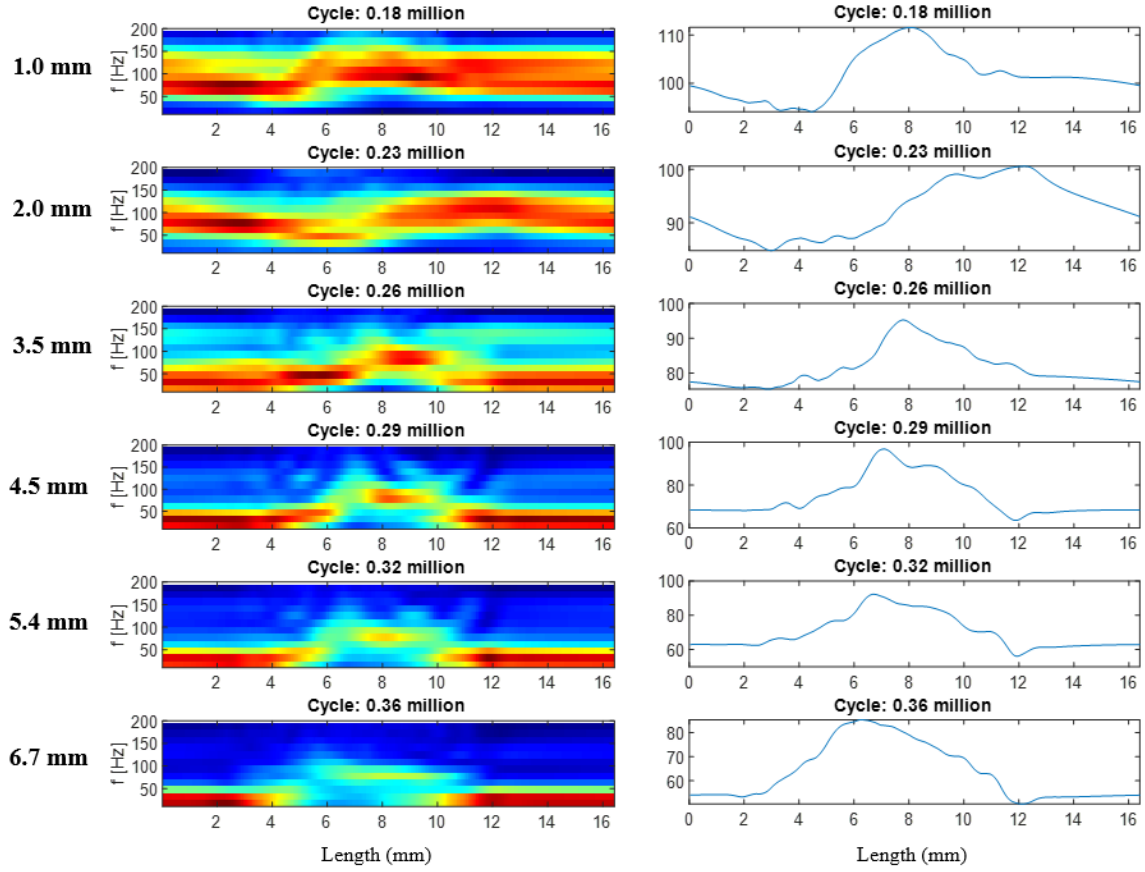


Fig. 5-17. Normalised WVS (left column) and average natural frequency (right column) of the IAS signal

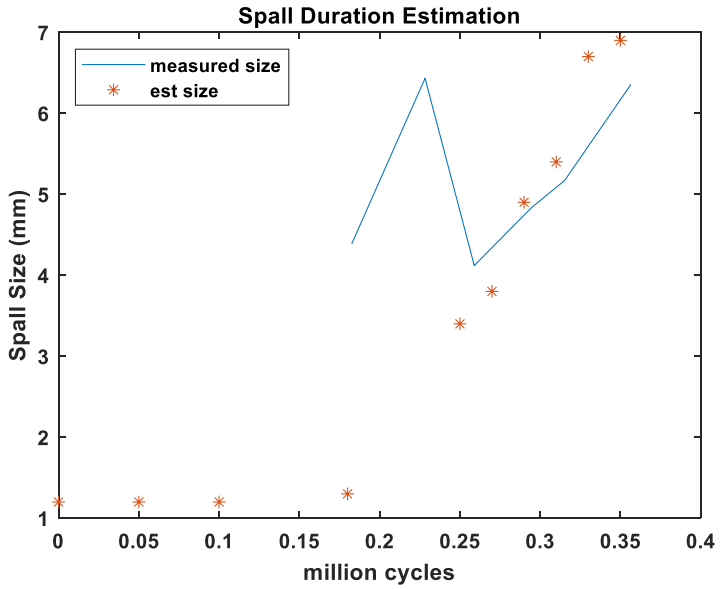


Fig. 5-18. Result of the spall size estimation approach for IAS signal

## 5.4 Discussion

As demonstrated in the previous sections, these four types of signals (acceleration, AE, IAS, and radial load as a proxy for displacement) have different performance in assessment of bearing fault severity. Different degradation indicators and spall duration estimation methods were applied with these four signals, and they are further validated by using four separate tests with different load and initial spall size.

In this section, the performance of these investigated signals and their severity indicators are summarised together for benchmarking and comparison. The indicators were selected from time domain, frequency domain and spall-event duration approaches as shown in Fig. 5-19. Their characteristics and potential are also discussed.

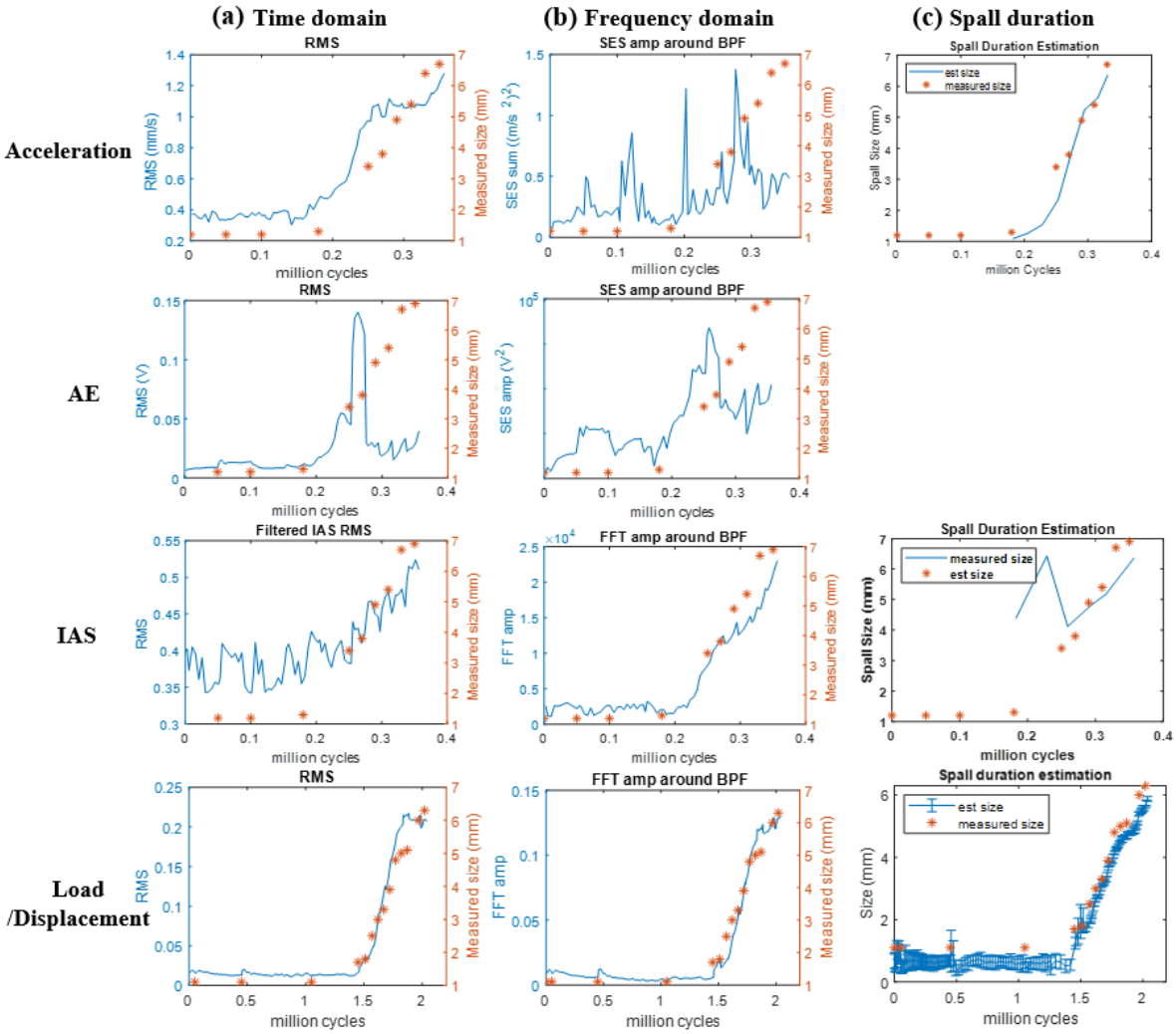


Fig. 5-19. Comparison between sensors and indicators: (a) time domain indicator, (b) frequency domain indicator, (c) spall size estimation

The overall RMS or band-pass filtered RMS can provide a fairly good performance on acceleration and load/displacement measurements, although it tends to plateau for large faults. On the other hand, RMS does not seem to be suitable for AE and IAS signals, which show trends that are non-monotonic and/or with large fluctuations.

Since the bearing fault information is commonly deemed to be modulated in the high-frequency range of acceleration and AE signals, the amplitude of the BPFO component of the SES was used as a spectral index for them, following both standard practice and better performance vs the raw spectrum (which is not even valid for AE due to the frequency range of the sensor). On

the other hand, the amplitude of the BPFO harmonics in the raw spectrum has been used for IAS and load/displacement, since they represent additive terms, not modulations. The frequency domain indicators show good severity trending performance for IAS and load, but they are not effective for acceleration and AE, which may indicate that the spall induced signature is better manifested in the low frequency range of angular speed and displacement, rather than in the components modulated in the high frequency range of acceleration or AE.

It is also important to remember that RMS values, spectral and SES amplitudes are strongly affected by operating conditions and thus would require a machine-specific calibration to provide a scaled quantitative estimate of spall size.

Direct spall-size quantification methods based on the duration of signal perturbations were only reported for acceleration, IAS, and radial load/displacement, because no applicable method was found effective for the AE signal in the experimental data. This approach is very simply applied on the displacement signal acquired from the band-pass filtered load and the integrated acceleration, and it shows very accurate results along the entire test, seemingly confirming the sensitivity of displacement to spall size, as previously reported by [8]. It should be emphasised that this cannot be expected in normal machines, since the relative displacement cannot be measured on the outer race alone, and the division between outer and inner races may not be a constant ratio. To extract similar information from acceleration and IAS, more sophisticated approaches are required, involving time-frequency maps that highlight the effect of stiffness variation on natural frequencies. The effectiveness is also lower, but still very promising for acceleration, fairly estimating all spall sizes larger than 1.5 mm. Also, IAS shows acceptable results for larger spalls (more than about 3.5 mm).

## 5.5 Conclusion and future work

This study has briefly reviewed the previous fault severity assessment methods of rolling element bearings on four types of signals (acceleration, AE, IAS, and load as a proxy for displacement). By conducting four similar bearing run-to-failure experiments and measuring the actual growth in spall size, time and frequency domain indicators, and spall passage time estimation methods for these four signals were investigated and compared. The main findings of this chapter are as follows.

1. The effectiveness of simple and well-established diagnostic indices with different sensor technologies was validated for the first time against actual spall-size measurements on naturally progressing faults, with a small artificial initiation.
2. The best performance was obtained from load measurements, which in this case were proportional to the relative displacement between inner and outer races. The estimates were simply obtained, quantitative (spall size in mm), accurate and very repeatable. Thus, the validity of the observations previously shown only for artificial faults is extended to natural degradation.
3. The amplitude of bearing fault spectral components in IAS signals correlates well with spall size, albeit not providing a direct quantitative measure of spall size.
4. Acceleration performs well for medium-large spall sizes and can provide a quantitative indication of spall size in microns, but only using sophisticated signal processing to identify the effect of spall size on natural frequency perturbations.
5. Applying the same natural-frequency perturbation method on IAS signals, acceptable results were obtained in the estimation of larger faults, suggesting a similar phenomenology as for acceleration, but involving torsional resonances. The relatively poorer performance of IAS vs acceleration could be case-specific and depend on the characteristics (and relative numbers) of torsional vs linear modes.
6. AE proved very poor in both quantification and tracking of natural spall size, possibly due to the sensitivity to other aspects of surface morphology, even though it might have advantages in earliest detection.

Because of the high signal-to-noise ratio of our test data, minimal pre-processing techniques were applied. Suitable pre-processing techniques for different signals could be a topic for future study.

The effect of machine layouts and configurations is also a fundamental aspect to be investigated further. Often, bearing housings are rigidly connected to the structure and less accessible than the case presented in this study, likely rendering load measurements less effective or even impossible. Similarly, the signal-to-noise ratio of accelerometric measurements would be likely lower in more complex configurations, both due to the lower mobility of the housing, but also

due to a series of interfering background components (e.g. gears). The effects of the same issues on the applicability of the natural-frequency-perturbation method to the same accelerometer measurements is also worth further investigation, as more complex systems would result in more complex transfer functions, on one hand offering more resonances to target, but on the other risking overlaps and interference. Angular (rotational) measurements are likely to show a comparative benefit in this regard, as they are likely to be less affected by complex layouts and structural resonances.

Given that the strong relationship between load and displacement is specific to the floating bearing housing shown in this work, the analysis of alternative displacement measurements for more general machine configurations is a natural continuation of this study. This however does not invalidate the general observation that displacement is in itself an effective quantity for bearing fault-severity, confirmed also by previous studies on different configurations [8], and in fact this encourages further work in this direction.

## 5.6 Validation on higher shaft speed

An acceleration-based bearing spall size estimation approach was proposed in Chapter 4, and by comparing four different measurement methods (acceleration, AE, IAS, and radial load as proxy of displacement) in Chapter 5, it was found that radial load achieved the most precise results in fault-size estimation than the other signals and the acceleration-based approach came next with complex signal processing techniques required. However, all these approaches were tested by the bearing run-to-failure experiments under a relatively low shaft speed (6 Hz), which gave rise to the question that how higher shaft speed conditions would affect the fault-size estimation results. This chapter is presented to answer this question.

As specified in Section 3.4 and Table 3-4, seven bearing run-to-failure experiments were conducted in this project in total. Three of them are used in this chapter, and for the convenience of readers, they are summarised in Table 5-2 here. During the bearing run-to-failure process of each experiment, the shaft speed was decreased to 20, 15, 12, and 6 Hz regularly for data collection, which enabled the analysis of this section.

In the following part of this section, the speed effect of the displacement-based approach and the acceleration-based approach will be analysed individually.

Table 5-2. Experiment for the study of load and speed effect

| No. | Defect | Initial size (μm) | Load (kN) |
|---|---|---|---|
| 1 | Outer race | 1000 | 7 |
| 2 | | 1000 | 10.5 |
| 3 | Inner race | 500 | 10.5 |

### 5.6.1 Displacement-based approach

As previously discussed, when a rolling element falls into the spalling area, the relative displacement between the bearing inner race and outer race will decrease, which will lead to a perturbation of the applied radial load for this particular experiment facility. This perturbation appears in cycles of the ball-passing-spall frequency, and the duration of it was found proportional to the spall size. Based on this understanding, the load signal was bandpass filtered and/or synchronous averaged to reveal the spall related perturbation, and then chopped into ball-passing-spall periods to extract the spall duration individually. The detail of this approach was presented in Section.5.3.2.

Since this perturbation is caused by the rolling element falling into the spalling area, a natural suspicion is that as the shaft speed rising, the rolling element goes through the spall more quickly, and it may affect the duration of the perturbation in the load signal, and thus affect the fault-size estimation result. To address this question, the same spall size estimation approach was applied to the load data of the above mentioned three experiments under different shaft speed conditions from 6 to 20 Hz. The analysis results are summarised in Fig. 5-20.

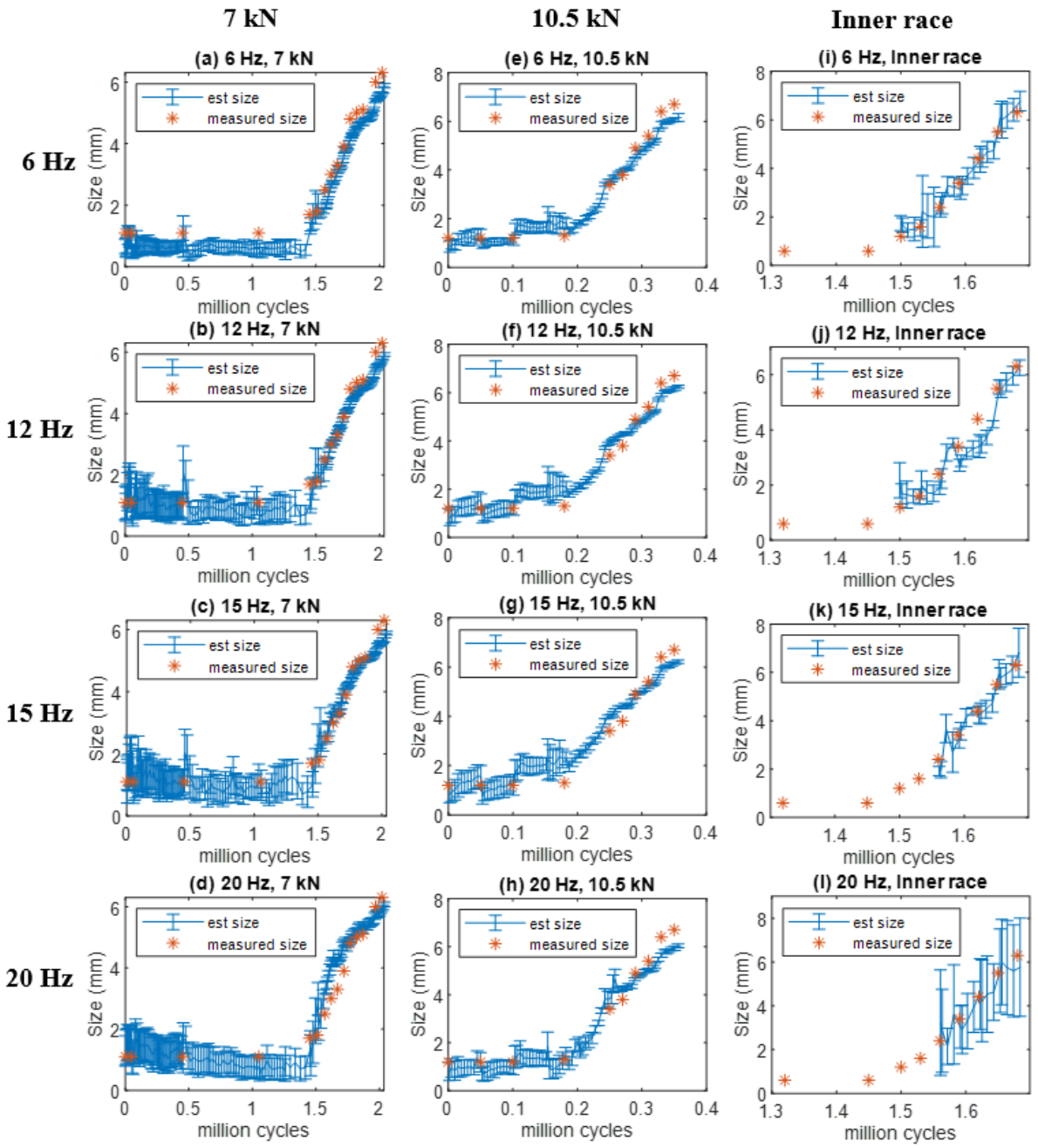


Fig. 5-20. Fault size estimation results of the radial-load-based approach under different load and speed conditions

As shown in Fig. 5-20, the blue line and the small error bars denote the mean estimated spall size and the standard deviation of each estimation, and the red dots are the actual spall size measured by disassembly the test bearing from time to time.

The first column of Fig. 5-20 illustrated the results for the first experiment, which has spalling on the outer race and 7 kN applied on the floating bearing housing. Seen from these four plots, as the shaft speed rising from 6 Hz to 20 Hz, the estimation results stay consistent in general, except for a rising of the standard deviation in the small spall area (under 2 mm) and some over estimation appears on the 20 Hz case when the spall size is between 2 to 5 mm.

Similar tendency could be seen from plots in the second column of Fig. 5-20, which are the results of the experiment with defect on the outer race and 10.5 kN load applied. For higher shaft speed, a slightly wider confidence interval of the estimated sizes is found when the spall size is lower than 2 mm, and for the 20 Hz case, the spall sizes are overestimated when it is around 4 mm.

The fault-size estimation results for the bearing with inner race defect are shown in the last column of Fig. 5-20. Unlike the former cases with outer race defect intentionally located at the centre of the loading area, the defect on the inner race rotates along with the shaft. Therefore, the spall related load perturbation should be amplitude modulated at shaft frequency, which makes it much harder to be identified, especially for small defect (less than 2 mm). Seen from the plots in the last column, the estimated results are still following the measured sizes quite well, but as the speed rises, the trend is not as consistent as in the former two outer-race-defect cases. For cases of shaft speed over 15 Hz, the effectiveness margin of this approach rises to about 2.5 mm in the defect size, and estimation confidence becomes lower for the 20 Hz case.

Overall, the shaft speed has almost no effect on the fault-size estimation results for bearings with outer race defect, but higher shaft speed would make the estimation more difficult and less precise when the defect is on the inner race of the test bearing.

### 5.6.2 Acceleration-based approach

A novel approach based on acceleration signal was proposed in Chapter 4, which utilises the natural frequency perturbation caused by the roller-spall interaction to estimate the spall size. Comparing to the representative existing methods, this approach was found the only one effective for naturally developed faults. Meanwhile, same as the load-based approach, the acceleration-based approach was only tested on the condition of 6 Hz shaft speed. To investigate the affection of shaft speed on its estimation results, the acceleration signals of the

three experiments listed in Table 5-2 under different shaft speed (6, 12, 15, and 20 Hz) are analysed in this section.

The fault-size estimation results of the three experiments under different shaft speed are illustrated in Fig. 5-21. As already stated in Chapter 4, the proposed acceleration-based approach is not effective for small spalls (shorter than about 1.5 mm), which could be due to that there is not enough time for the natural frequency to settle to another level. Therefore, the estimation for each case were applied after the point of the spall began to grow.

Different from the displacement-based approach, which estimated the spall size for each collected data point, the acceleration-based approach requires much more complex signal processing to conduct the high-resolution time-frequency analysis, therefore only the points before each stop were used for the estimation. And since the adopted time-frequency analysis technique (Wigner-Ville Spectrum) already averages over ball-pass cycles, there is no mean value and standard deviation for each estimation point as in the load-based approach.

Seen from Fig. 5-21, the blue lines of estimation results are following the measured points quite well in general for all three experiments, although appear more fluctuating and less accurate when the shaft speed rises. The results demonstrated that the proposed acceleration-based approach is generally not affected by the shaft rotational speed, however, it depends on careful selection of the filtering band and the threshold of frequency perturbation for different speed cases.

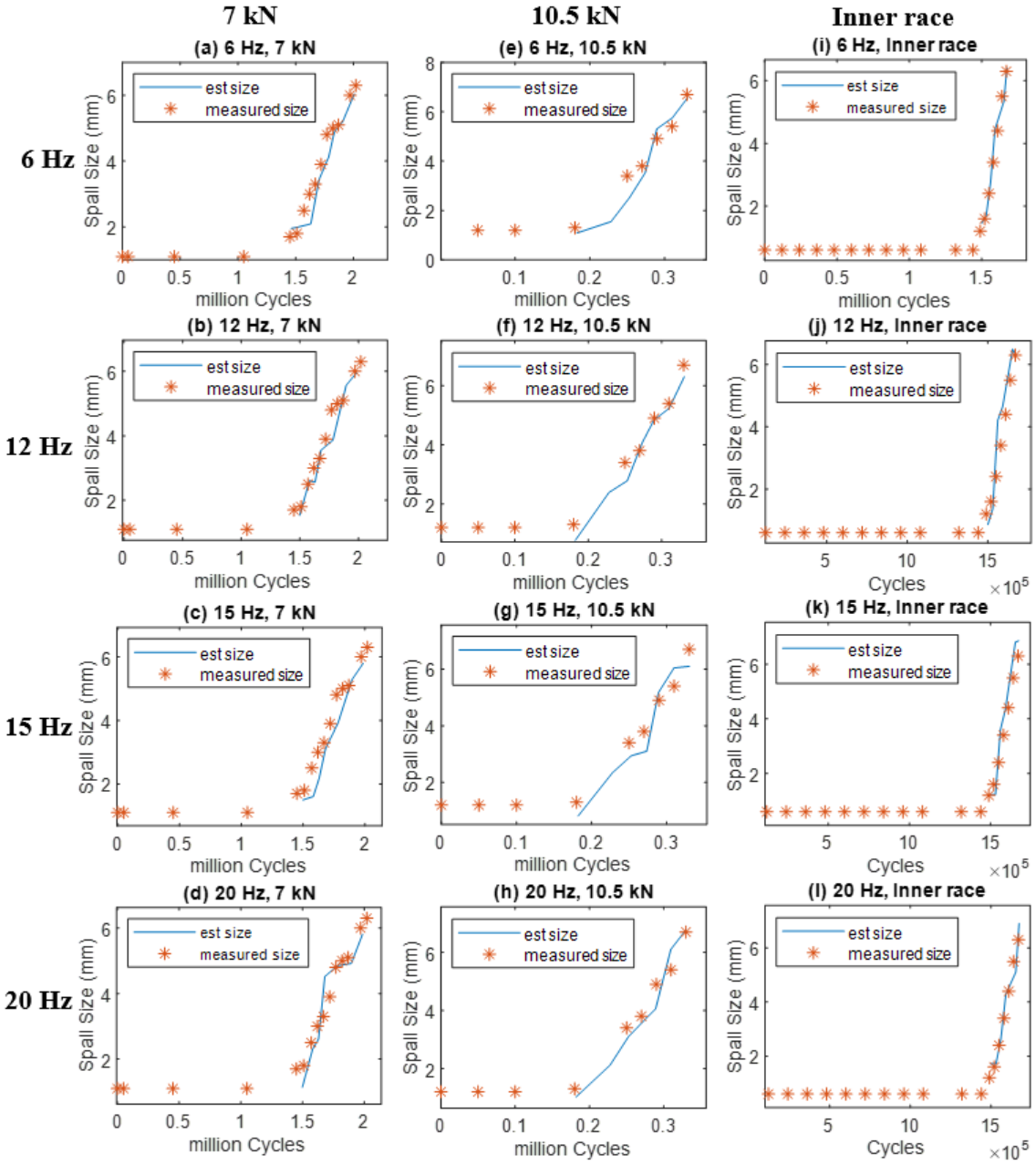


Fig. 5-21. Fault size estimation results of the acceleration-based approach under different load and speed conditions

Overall, the study conducted in this section proves that the proposed acceleration-based approach and displacement-based approach are both independent on the shaft speed.

# 6. Spall size estimation based on proximity probes

In Chapter 5, four types of sensors were mounted for the bearing run-to-failure experiment: the accelerometer, the AE sensor, an encoder, and a load cell. By comparison, it was found that the load cell signal is the most effective in the estimation of spall size. This was justified based on the specific configuration of the test rig: the loading mechanism connected to the test-bearing housing behaves like a spring and the load signal is therefore proportional to the displacement of the outer race of the bearing. Considering that in this peculiar arrangement the floating housing was significantly more mobile than the shaft (supported by large support-bearings), it is reasonable to assume that this absolute displacement proxy was also a proxy for the relative displacement between shaft and casing, i.e. inner vs outer bearing race.

The success of relative displacement was in fact theoretically predictable based on the observations of [10] discussed in Section 5.4. However, two main questions remained to be answered, related to the practical measurement of this quantity. Firstly, would a direct measurement of the housing displacement in the configuration of Chapter 5 be as effective as the proxy used so far, thus validating all the considerations of Chapter 5? Secondly, how well would this approach extend to more common machine configurations, where the bearing housing is rigidly installed within the structure of the machine?

To answer these questions, a proximity probe was added to both the bearing test rig used in the previous sections and on a larger gearbox test-rig. They are firstly mounted on the bearing rig to validate the previous study, and then applied on another large gearbox facility.

In addition to the experiments, the signal processing process is refined in this section to give a more automated fault-size estimation method based on the proximity probe signals.

In the following part of this chapter, the development of the spall size estimation approach based on proximity probes is firstly presented in Section 6.1, then the results of the two experiment are provided in Section 6.2. At last, a short summary is given in Section 6.3.

## 6.1 Spall size estimation approach based on proximity probes

The main idea of this method is to use the duration of the displacement perturbation of the bearing inner race or outer race to estimate the spall size on this bearing. It is based on the knowledge that the relative displacement between the bearing inner race to the outer race would change when a roller is in the spall zone, which has been proved theoretically [52] and experimentally [8]. The proximity probe-based approach is similar to the load-based one, which was briefly introduced in Section 5, but the pre-processing step is refined and more details are presented in this section.

**Step 1: Pre-processing**

The first step of this method is to remove the irrelevant signal and reveal the fault induced displacement perturbation. As reviewed in Section 2, order tracking and synchronous averaging are the commonly used techniques. Order tracking can remove the shaft speed fluctuation by resampling the fix-time-interval signal into fix-phase-interval signal. Then synchronous averaging can be applied to the order tracked signal to separate the shaft rotation related periodic signal from the non-periodic spall incurred signal.

**Step 2: Bandpass filter**

After pre-processing, the shaft frequency related displacement variation is removed, and the remaining signal is dominated by the spall related displacement variation. To further reveal this phenomenon, a bandpass filter around the corresponding bearing failure frequency (e.g., BPFO, BPFI) should be applied to remove the noise in irrelevant frequency range. The recommended range is from half to a bit over eight times the bearing failure frequency.

In this case, the spall in on the outer race of Nachi 6205 bearing, and its BPFO is about 3.6 times of the shaft frequency. Since the signal has already been transferred from time domain to angular domain by order tracking, the frequency domain is in the unit of shaft orders. Thus, the range of the filter band is selected to 1.8 – 30 orders of the shaft revolution.

**Step 3: Cut signal by BPF**

After bandpass filtering, the displacement signal should be clearly repeating in ball passing defect order. But due to the roller slippage, it is not strictly periodic. To overcome the fluctuation and instability caused by the slippage, a second time order tracking is employed here according to the unwrapped instantaneous phase of the signal itself bandpass filtered around the ball passing defect order with a tolerance of ±10%, which is a tacho-less order tracking technique proposed by Bonnardot et al. [202].

After the second time order tracking, each signal segment of one ball passing defect period should have the same number of samples, and thus it could be chopped into pieces of the same length. In practical, the one dimensional vector of the signal is reshaped into a m-by-n matrix, where m is the number of samples in one ball passing defect period, and n is number of periods it contains.

**Step 4: Spall size calculation**

Until now, many periods of ball passing spall signal segments are obtained, and each signal segment shows how the displacement varies during one BPF cycle. The time duration of the spall-induced displacement could then be used to calculate the spall size, as indicated in the existing methods and in our previous two chapters.

$$l_{spall} = \frac{\pi f_r \left(D_p^2 - d^2\right)}{2D_p} t_{diff} \qquad (7-2)$$

where $t_{diff}$ is the time duration of the spall induced displacement perturbation, $D_p$ is the pitch diameter of the bearing, $d$ is the roller diameter, and $f_r$ is the shaft frequency. However, the time duration $t_{diff}$ requires a threshold to determine the beginning and ending point of the desired period, which could be biased by background noise.

To address these problems and improve the robustness of this methods, the proportion of spall duration to the whole BPF cycle length is used to calculate the spall length as follows:

$$l_{spall} = \begin{cases} \frac{\pi(D_p + d)}{N_b} R_{spall}, & spall\ on\ the\ outer\ race \\ \frac{\pi(D_p - d)}{N_b} R_{spall}, & spall\ on\ the\ inner\ race \end{cases} \quad (7-3)$$

where $R_{spall}$ is calculated for each BPF signal segment. Simply put, the length of the spall is considered proportional to the ratio points under (or above) a certain threshold to the whole length of the segment. Since these signal segments were split according to BPFI or BPFO cycles, the length of them is already correlated to the distance between balls on the inner race or outer race, respectively. It should be noted that for bearing with inner race defect, the displacement perturbation is amplitude modulated at the shaft frequency, as the spall rotates along with the shaft. Therefore, only the BPF periods with clear perturbations should be considered.

The usage of spall ratio overcomes the influence of some sudden spikes in the signal caused by noise. Since the previous synchronous average step has removed the zero-frequency component from the signal and shifted it to around the mean value of zero, so zero is used as the threshold.

The above procedure is conducted for each signal segment of BPF cycle individually, therefore a distribution of estimated spall sizes can be drawn, and its mean value is used as the estimated spall size.

## 6.2 Experimental results

Two experiments were conducted on the bearing rig and planetary gearbox rig respectively, whose detail information are reported in Section 3.2.1 and Section 3.2.2. The analysis results of these two experiments based on the size estimation method provided in Section 6.2 are presented in the following part of this chapter.

### 6.2.1 Results of the bearing rig test

For the bearing rig test, the results of the first 3 steps, order tracking, synchronous averaging and bandpass filtering are presented in Fig. 6-1. The spall induced displacement perturbations are already visible in the raw displacement signal of Fig. 6-1 (a), although somewhat modulated

by the shaft frequency. In Fig. 6-1 (b), the order tracked signal has been transferred from time domain to angular domain.

The residual signal after synchronous averaging is shown in Fig. 6-1 (c). By subtracting the average signal, the shaft frequency components and the mean value are removed. Therefore, the signal in Fig. 6-1 (c) is more uniform and has been shifted to around the zero mean comparing to that in Fig. 6-1 (b).

In the third step, a bandpass filter around the bearing failure frequency was applied to reveal the spall induced displacement perturbation more clearly, and its result is shown in Fig. 6-1 (d). As stated in Step 3 of Section 6.2, the filter band was selected to be 0.5 – 8 times of the BPF frequency, which is 1.8 – 30 orders of the shaft frequency in this case.

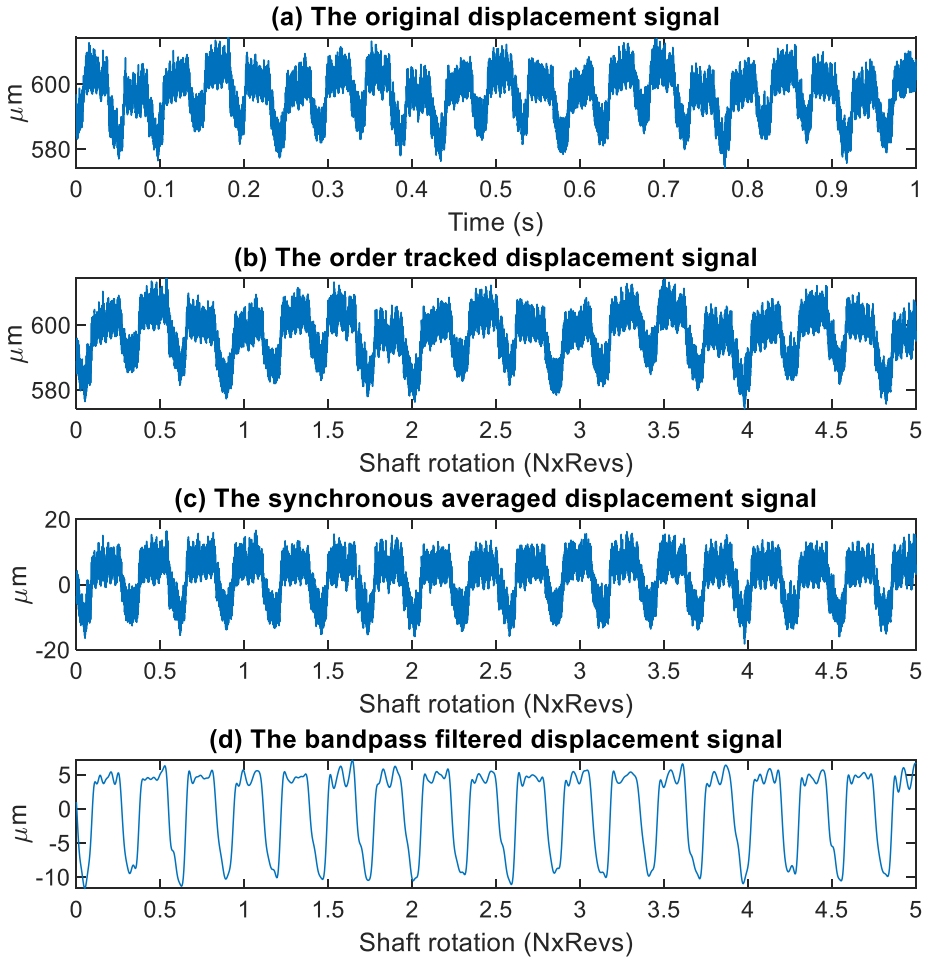


Fig. 6-1. Results of the first 3 signal processing steps for the bearing rig data: (a) the original displacement signal, (b) the signal after the first step of order tracking, (c) the signal after step 2 of synchronous averaging, (d) the signal after step 3 of bandpass filtering

The fourth step is to split the bandpass filtered signal in Fig. 6-1 (d) according to the BPF frequency, resulting in single BPF periods as displayed in Fig. 6-2 (a). To compare with the spall length, the x axis is transformed from angular domain to the corresponding distance on the outer race. It is seen that the duration of the displacement perturbation in the middle is consistent with the spall depth profile shown in Fig. 6-2 (b).

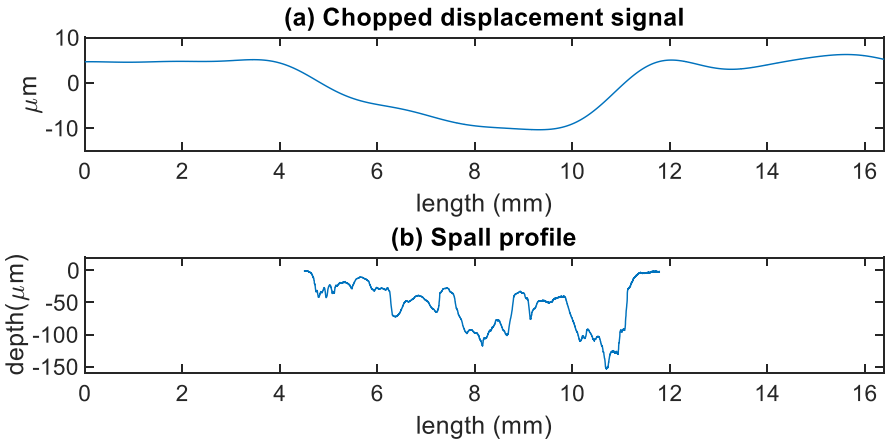


Fig. 6-2. Comparison of the split signals with the spall profile on the bearing outer race

As stated in Step 5 of Section 7.2, the duration of the spall induced displacement perturbation for each BPF period can be calculated by using the proportion of the signal under the threshold zero to the whole period times the distance between balls on the bearing outer race. Summarising all the estimated results together, their distribution is illustrated in Fig. 6-3, and their mean value is 6.3 mm.

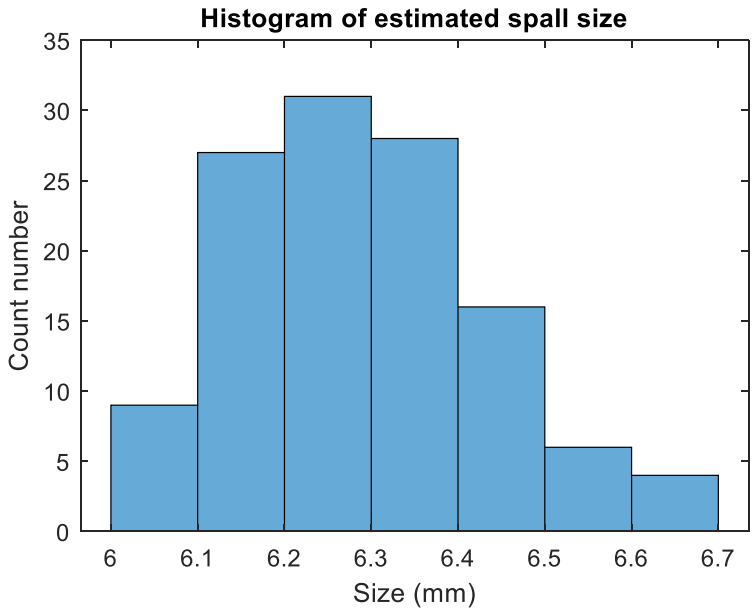


Fig. 6-3. Distribution of the estimated spall sizes for the bearing rig test

### 6.2.2 Results of the gearbox rig test

For the gearbox rig experiment, a proximity probe is installed vertically to the coupling near the test bearing, which is solidly connected to the shaft and the inner race of the test bearing. Therefore, the major difference between this experiment to the bearing rig test is that the inner race displacement of the spalled bearing is analysed, rather than the outer race enclosed in the floating case.

The first 3 signal processing steps used in this case are identical to those used for the bearing rig test, and the results are shown in Fig. 6-4. Comparing this to Fig. 6-1, it can be found that the overall non-bearing related shaft displacement is much larger, and the spall induced displacement perturbation is totally masked by the shaft-synchronous component, possibly due to unbalance, misalignment of the measured shaft, or non-circularity of the coupling.

After synchronous averaging, the spall induced displacement perturbations are manifested in the residual signal, as seen from Fig. 6-4 (c), where the existence of the spall increased the displacement as indicated above. This phenomenon is further highlighted by adopting the bandpass filter as shown in Fig. 6-4 (d).

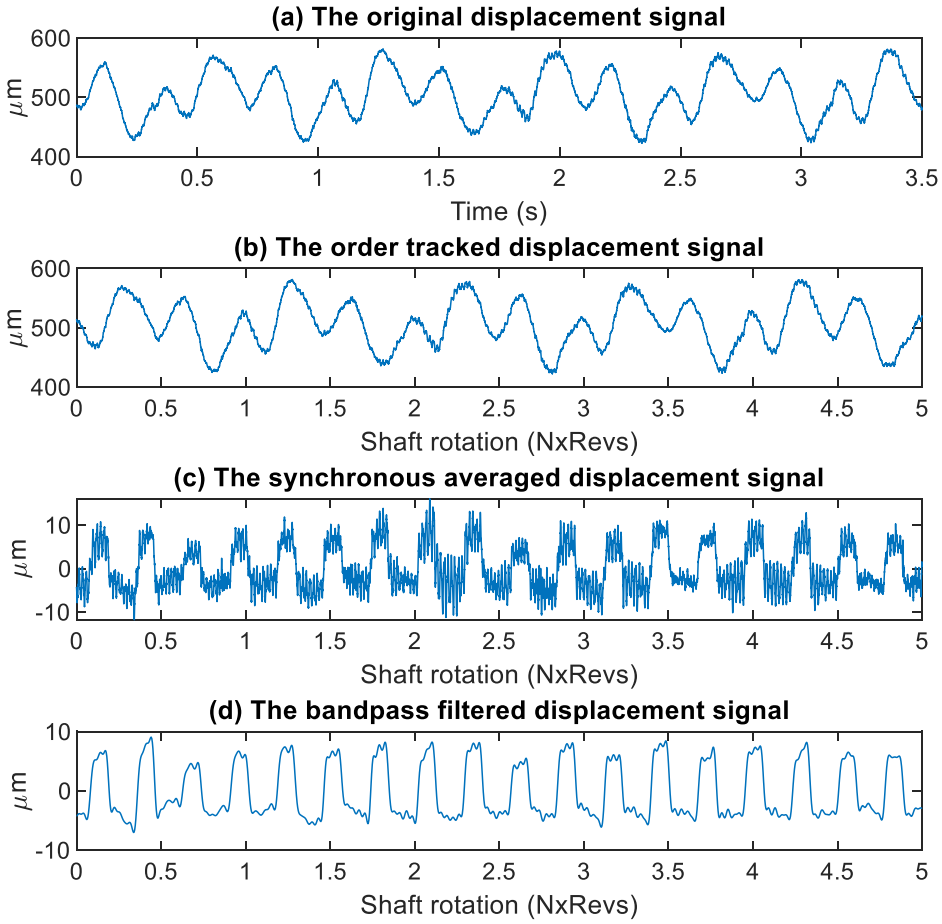


Fig. 6-4. Results of the first 3 signal processing steps for the gearbox rig data: (a) the original displacement signal, (b) the signal after the first step of order tracking, (c) the signal after step 2 of synchronous averaging, (d) the signal after step 3 of bandpass filtering

The signal is then again split in BPF periods as that shown in Fig. 6-5 (a).

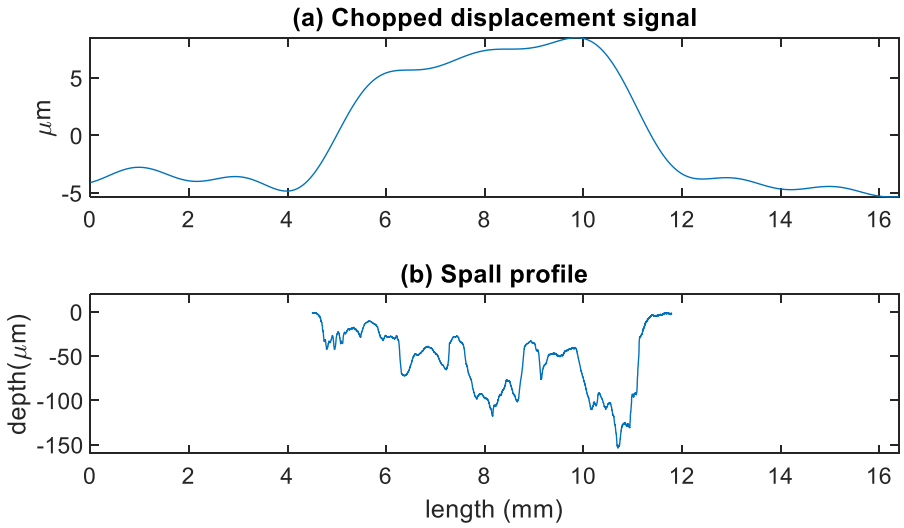


Fig. 6-5. Comparison of the chopped displacement signal from the gearbox rig with the spall profile on the bearing outer race

Since the proximity probe was in this case installed 180 degress from the load zone, the displacement due to the spall is positive and the ratio of points above zero is used for size estimation. This consideration must be carefully taken according to the direction of the sensor and position of the spall.

Finally, the distribution of the size estimation results is shown in Fig. 6-6, and its mean value is 6.5 mm.

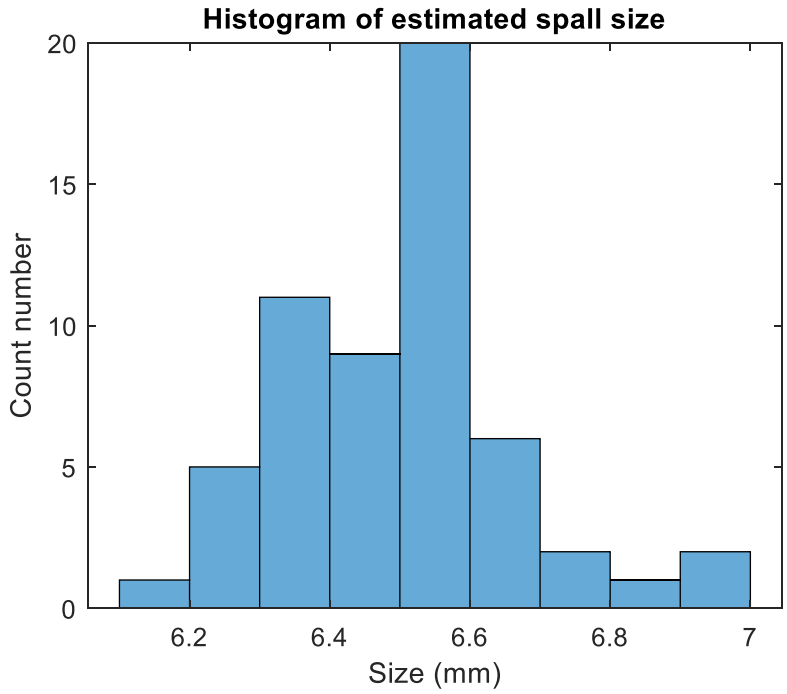


Fig. 6-6. Distribution of the estimated spall sizes for the gearbox rig test

## 6.3 Summary

In this chapter, a bearing spall size estimation based on proximity probe sensors is proposed. It is based on the knowledge that when a roller falls into the spall, the inner race moves relatively to the outer race. The proposed method uses the duration of the spall induced perturbation on the relative displacement between bearing inner race and outer race to estimate the spall size, with the help of some pre-processing steps aimed at removing shaft-synchronous components from the signal.

The proposed method was tested on two experimental signals, one on the bearing rig, and one on the planetary gearbox rig, with stationary shaft and stationary bearing case, respectively. Both experiments demonstrated that the proposed method could effectively estimate the size of the natural spall on the outer race of the test bearing.

This research investigated the possibility of using proximity probes to track the spall size on rolling element bearings and it is likely more reliable than the accelerometer-based methods in spall size estimation, because it requires less sophisticated signal processing procedures.

Despite the advantages of this method, there are still many questions to be answered, such as the influence of load and speed, and the detection of spalling on different positions. Moreover, the detectable size range of the spall is another topic to be covered, for example the minimum detectable spall size and signal behaviour when the spall size is larger than the roller distance. More experiments on different machines and under different load/speed are required to answer these questions, but they could not be carried out in this thesis due to time limitation and local COVID restriction. Therefore, it became a direction of future work.

# 7. Discussion

The main contribution of this thesis is the advancement of bearing fault severity assessment techniques, especially for the previously unsolved case of natural spalls. It is achieved by comparing different measurement approaches and proposing two effective methods: one based on acceleration, and another based on the relative displacement between bearing races. In this chapter, the strength and issues of these two approaches will be discussed by the aspects of ease of implementation, the requirement for signal processing, and estimation accuracy.

## 7.1 Ease of implementation

Accelerometers are the most widely used vibration sensor, and maintainers and operators are familiar with this technology. Therefore, the first advantage of the accelerometer-based approach is that it is easily retrofitted to existing condition monitoring systems without the need for additional sensors or data collection devices.

On the other hand, proximity probes are usually used for the condition monitoring of journal bearings rather than rolling element bearings. Therefore, a displacement-based method would require an upgrade of the measurement system, including allowing access to the shaft. Positioning and mounting of proximity probes are more constrained than accelerometers, which can be installed easily on any external surface. All these aspects make this approach harder to implement, especially on existing machines. However, with the fast development of Industry 4.0 and IoT (Internet of Things), it is more likely that the inclusion of displacement sensors in the design phase mitigates these problems.

## 7.2 Signal processing requirement

As presented in Chapter 4, the proposed acceleration-based approach relies on the identification of small and short-time perturbations of the system's natural frequencies. This results in a complex signal processing procedure, involving the manual choice of a few parameters. One is the target frequency band, which ultimately requires a trial-and-error approach, even if it is guided by observations on the PSD. Another parameter to be chosen is the threshold determining when a natural frequency deviation is considered sufficient to classify it as a fault-induced perturbation, and therefore identify its extent in time/angle. The fact that the threshold must be redefined if the target band changes makes the process even more delicate. The complexity of the procedure is also accompanied by its computational cost, especially for the time-frequency analysis (WVS). The latter also requires long signals to achieve high resolution, and a high sampling rate to capture short-time and possibly high-frequency events.

The displacement-based approach is instead directly measuring the rolling element falling into spall. This means that the signal of interest is in the low-frequency range and the estimation process only requires a short record of the signal and a relatively low sampling rate. Signal processing is also mostly pre-processing to increase the accuracy and automation of the procedure, but in fact only requires a band-pass filtering (or at most a synchronous averaging operation) to remove shaft-synchronous harmonics and achieve fairly accurate results manually.

## 7.3 Estimation accuracy

By comparing with the existing methods, the proposed acceleration-based approach was proved not only as effective as the former methods for artificial spalls, but also the only one valid for natural spalls. However, the manually selected parameters for the frequency band and thresholds limited the robustness of this approach. Moreover, this approach was found to be effective only for spalls larger than 1.5 mm, possibly due to the limited capability to capture very short-time perturbations in the natural frequencies.

By contrast, the results of the displacement-based approach are more robust and reliable as a consequence of the very limited signal processing required. The distributional output of this method (mean and standard deviation of the estimated spall size) boosts confidence in the

results. Contrarily to acceleration, the displacement approach is effective for all spall sizes, including spalls smaller than 1.5 mm, as indicated in Section 5.

The effectiveness of both acceleration- and displacement-based approaches was proven constant at the different shaft speeds as investigated in Section 5.6.

Overall, by comparing the pros and cons of these two approaches, a preliminary conclusion can be drawn that the acceleration-based approach is more likely to be applied in the present stage, but if installation issues are solved, the displacement-based approach is likely to give more accurate and reliable results.

# 8. Conclusions and Future Work

Overall, this thesis aims to build effective methods to estimate the spall size of REBs and hence indicate the fault severity. Therefore, three objectives were set up to achieve this target: 1) Extend the use of accelerometers to the estimation of spall-size in naturally growing faults, 2) Investigating the capabilities of other measurements for fault severity assessment in naturally growing faults, and 3) Further investigate and refine the most promising approach. These objectives were achieved step by step as described in the above chapters. In this section, the achievements and contributions of this thesis are summarised, and the limitations of this research are also discussed. At last, recommendations on the future research directions are presented.

## 8.1 Summary of outcomes

In this thesis, four types of measurements were compared in tracking bearing fault severity. Two novel spall size estimation approaches were proposed based on accelerometer and proximity probe, respectively. Overall, this thesis provided a framework for the size estimation techniques of naturally extended bearing spalls, and it is believed to have formed a foundation for future studies in this area. The outcomes for each objective are summarised in the following part of this section.

**Objective 1: Extend the use of accelerometers to the estimation of spall size in naturally growing faults.**

Based on the bearing run-to-failure experimental data, a novel approach of using acceleration signal to detect the spall size of REBs was proposed in Section 4. The foundation of this method is that the stiffness of the bearing would change as the roller falls into the spalling zone. A time-frequency analysis technique, Wigner-Ville Spectrum (WVS), which has high resolution

in both time and frequency domain without interference terms, was adopted to extract the local natural frequency perturbation caused by the spall induced stiffness variation. The duration of this perturbation was used to estimate the size of the spall.

The key difference of this approach to the prior literature is that it focuses on the signal variation brought by the spall during the whole ball-passing-spall process, rather than detecting the weak entry and exit events. Experiments were taken to compare the performance of the proposed method with the previous ones, and it was found that they are similarly effective for artificial spalls with sharp edges, but only the proposed method is successful with naturally developed spalls.

The proposed acceleration-based approach was proved effective for bearings with defects on either inner race or outer race. The estimation results tracked the actual spall size very well during the bearing run-to-failure process, from about 1.5 mm to over 8 mm.

**Objective 2: Investigate the capabilities of other measurements for fault severity assessment in naturally growing faults.**

Given its popularity, acceleration was the first focus of this thesis (Objective 1). However, thanks to the rapid progress of Industry 4.0 and IoT, more types of sensors are now available to be built into machines at the design phase. Consequently, the second objective of this thesis was to investigate other measurement options for bearing fault severity assessment, especially for naturally growing spalls.

In Chapter 5, four types of measurement approaches (acceleration, displacement, AE, and IAS) were compared in tracking the natural evolution of spall severity in REBs. To the author's knowledge, it is the first time that estimates based on different sensor technologies are compared against actual spall-size measurements of naturally progressing faults.

The best performance was found in the load signal, which, in the specific arrangement of the UNSW bearing test-rig, was identified as a proxy of radial displacement between the bearing races. The estimations were quantitative (spall size in mm), accurate, very repeatable, and required very limited signal processing. For the IAS derived from encoder signals, the amplitude of bearing fault spectral components correlated well with the spall size, but not

giving a quantitative measure (unknown scaling factor). The acceleration signal required sophisticated signal processing to identify the spall-induced natural frequency perturbation, and it only performed well for medium-to-large spall sizes. The AE signal was found less effective in both quantification and tracking of the natural spall.

**Objective 3: Further investigate and refine the most promising approach and related technology.**

By comparing the capabilities of different measurements (Objective 2), displacement was found the best measurement for bearing spall size estimation. However, in the initial study, the displacement was indirectly derived from the load-cell signal, a proxy only valid in the case of floating bearing housings. A more generally applicable (and properly displacement-related) sensor technology was to be investigated.

Therefore, a proximity probe was added to the former bearing test rig, and its direct displacement signal was found very similar to the load proxy. This validated the observation and physical explanations of the previous study, but still did not prove the general applicability of a displacement-based approach to other machine configurations.

For this reason, a proximity probe was also installed on the UNSW planetary gearbox rig, which has rigidly mounted bearing housings. The proximity probe measured shaft radial displacements relative to the machine foundation, and therefore the bearing housing. The spall estimation procedure applied to load measurements was improved and automated for the proximity probe measurements, which were proven effective on both facilities. Compared to acceleration, the proximity probe-based approach was found more reliable and requiring less sophisticated signal processing.

## 8.2 Future works

Although the proposed approaches have been proved effective on the experimental data used in this work, there is still room for validation, and to improve their accuracy and robustness. Some possible directions for future studies are given as follows.

1. For the acceleration-based approach proposed in Chapter 4, some parameters are selected manually, for instance, the targeted frequency band, and the threshold used to

detect natural frequency perturbations. Therefore, one aim of future works is to develop automated and rigorous methods to select these parameters. On a similar topic, the computational efficiency of the procedure is likely sub-optimal and could benefit from further developments.

2. Another limitation of this research is that the experimental data generated from the Bearing Prognostics Simulator (BPS) test rig has a high signal-to-noise ratio. As a result, minimal pre-processing techniques were required in the proposed methods. In real-life circumstances, all measured signals are likely to be masked by stronger background noise and other sources. The development and testing of suitable pre-processing techniques for more complex machines constitute another research direction in this area.
3. The outputs of the bearing fault severity estimation are a natural starting point for prognostics, whose aim is to predict the progression of the fault. It is hoped that the methodologies of this work will aid future prognostic studies.
4. The spall size estimation approaches proposed in this thesis were validated on two test rigs. Further experiments on different machines and working conditions could be beneficial for testing their applicability. Due to the time limitation of this project and the current local COVID restriction, these works are hoped to be done in the future.

In summary, this research provided a framework for bearing fault severity estimation with different measurement approaches. Improvements could be made in automating the proposed methods, extending their scope of applications, and applying them for prognostics.

# References


[1] T. A. Harris, *Rolling Bearing Analysis*. John Wiley and sons., 2001. doi: 10.1115/1.3617048.

[2] G. D. White, *Introduction to Machin Vibration*. DLI Engineering, 2008.

[3] G. Georgoulas, T. Loutas, C. D. Stylios, and V. Kostopoulos, "Bearing fault detection based on hybrid ensemble detector and empirical mode decomposition," *Mech. Syst. Signal Process.*, vol. 41, no. 1–2, pp. 510–525, 2013, doi: 10.1016/j.ymssp.2013.02.020.

[4] SKF, "Bearing damage and failure analysis," 2017. [Online]. Available: https://www.skf.com/binaries/pub12/Images/0901d1968064c148-Bearing-failures---14219_2-EN_tcm_12-297619.pdf

[5] ISO, "ISO 15243: Rolling bearing - Damage and failures — Terms , characteristics and," 2017.

[6] R. B. Randall, *Vibration-based condition monitoring: industrial, automotive and aerospace applications*. John Wiley & Sons, 2021.

[7] M. Cerrada, R.-V. Sánchez, C. Li, F. Pacheco, D. Cabrera, J. Valente de Oliveira, and R. E. Vásquez, "A review on data-driven fault severity assessment in rolling bearings," *Mech. Syst. Signal Process.*, vol. 99, pp. 169–196, Jan. 2018, doi: 10.1016/J.YMSSP.2017.06.012.

[8] A. Moazen Ahmadi, C. Q. Howard, and D. Petersen, "The path of rolling elements in defective bearings: Observations, analysis and methods to estimate spall size," *J. Sound Vib.*, vol. 366, pp. 277–292, 2016, doi: 10.1016/j.jsv.2015.12.011.

[9] W. Moustafa, O. Cousinard, F. Bolaers, K. Sghir, and J. P. Dron, "Low speed bearings

fault detection and size estimation using instantaneous angular speed," *JVC/Journal Vib. Control*, vol. 22, no. 15, pp. 3413–3425, 2016, doi: 10.1177/1077546314560600.

[10] D. Petersen, C. Howard, and Z. Prime, "Varying stiffness and load distributions in defective ball bearings: Analytical formulation and application to defect size estimation," *J. Sound Vib.*, vol. 337, pp. 284–300, 2015, doi: 10.1016/j.jsv.2014.10.004.

[11] D. Petersen, C. Howard, N. Sawalhi, A. Moazen Ahmadi, and S. Singh, "Analysis of bearing stiffness variations, contact forces and vibrations in radially loaded double row rolling element bearings with raceway defects," *Mech. Syst. Signal Process.*, vol. 50–51, pp. 139–160, 2015, doi: 10.1016/j.ymssp.2014.04.014.

[12] J. Lee, H. Qiu, G. Yu, and J. Lin, "Bearing data set," *IMS, University of Cincinnati, NASA Ames Prognostics Data Repository, Rexnord Technical Services*, 2007. http://ti.arc.nasa.gov/project/prognostic-data-repository

[13] P. Nectoux, R. Gouriveau, K. Medjaher, E. Ramasso, B. Chebel-Morello, N. Zerhouni, and C. Varnier, "PRONOSTIA: An experimental platform for bearings accelerated degradation tests.," in *IEEE International Conference on Prognostics and Health Management, PHM'12.*, 2012, pp. 1–8.

[14] H. Zhang, P. Borghesani, W. A. Smith, R. B. Randall, M. R. Shahriar, and Z. Peng, "Tracking the natural evolution of bearing spall size using cyclic natural frequency perturbations in vibration signals," *Mech. Syst. Signal Process.*, vol. 151, p. 107376, Apr. 2021, doi: 10.1016/j.ymssp.2020.107376.

[15] H. Zhang, P. Borghesani, R. B. Randall, and Z. Peng, "A benchmark of measurement approaches to track the natural evolution of spall severity in rolling element bearings," *Mech. Syst. Signal Process.*, vol. 166, p. 108466, Mar. 2022, doi: 10.1016/j.ymssp.2021.108466.

[16] M. J. Neale, "Rolling bearings in service: TS Nisbet and GW Mullett." Elsevier, 1978.

[17] ISO, "ISO 281 Rolling bearings - Dynamic load ratings and rating life," 2007. doi: 10.1021/es0620181.

[18] G. Lundberg, "Dynamic capacity of roller bearings," *IVA Handl.*, vol. 210, 1952.

[19] T. Makino, Y. Neishi, D. Shiozawa, S. Kikuchi, S. Okada, K. Kajiwara, and Y. Nakai, "Effect of defect shape on rolling contact fatigue crack initiation and propagation in high strength steel," *Int. J. Fatigue*, vol. 92, pp. 507–516, 2016, doi: 10.1016/j.ijfatigue.2016.02.015.

[20] G. Fajdiga, S. Glodež, and J. Kramar, "Pitting formation due to surface and subsurface initiated fatigue crack growth in contacting mechanical elements," *Wear*, vol. 262, no. 9–10, pp. 1217–1224, Apr. 2007, doi: 10.1016/j.wear.2006.11.016.

[21] A. Warhadpande, F. Sadeghi, M. N. Kotzalas, and G. Doll, "Effects of plasticity on subsurface initiated spalling in rolling contact fatigue," *Int. J. Fatigue*, vol. 36, no. 1, pp. 80–95, Mar. 2012, doi: 10.1016/j.ijfatigue.2011.08.012.

[22] J. E. Shigley, *Shigley's mechanical engineering design*. Tata McGraw-Hill Education, 2011.

[23] G. Lundberg and A. Palmgren, "Dynamic capacity of rolling bearing," *Acta Polytech. Mech. Eng.*, 1947.

[24] T. A. Harris and W. K. Yu, "Lundberg-Palmgren fatigue theory: considerations of failure stress and stressed volume," *J. Tribol.*, vol. 121, no. 1, p. 85, Jan. 1999, doi: 10.1115/1.2833815.

[25] E. V Zaretsky, J. V. Poplawski, and C. R. Miller, "Rolling bearing life prediction-past, present, and future," Nov. 2000, Accessed: Apr. 16, 2019. [Online]. Available: https://ntrs.nasa.gov/search.jsp?R=20010018968

[26] M. N. Kotzalas and T. A. Harris, "Fatigue failure progression in ball bearings," *J. Tribol.*, vol. 123, no. 2, p. 238, Apr. 2001, doi: 10.1115/1.1308013.

[27] P. Paris and F. Erdogan, "A critical analysis of crack propagation laws," *J. Basic Eng.*, vol. 85, no. 4, p. 528, 1963, doi: 10.1115/1.3656900.

[28] G. E. Morales-Espejel and A. Gabelli, "The behavior of indentation marks in rolling–sliding Elastohydrodynamically Lubricated Contacts," *Tribol. Trans.*, vol. 54, no. 4, pp.

589–606, Jul. 2011, doi: 10.1080/10402004.2011.582571.

[29] G. E. Morales-Espejel and A. Gabelli, “The progression of surface rolling contact fatigue damage of rolling bearings with artificial dents,” *Tribol. Trans.*, vol. 58, no. 3, pp. 418–431, May 2015, doi: 10.1080/10402004.2014.983251.

[30] S. Zhuang, “Tribological investigation on the degradation process of contact fatigue in rolling bearings,” University of New South Wales, 2021.

[31] S. Singh, C. Q. Howard, and C. H. Hansen, “An extensive review of vibration modelling of rolling element bearings with localised and extended defects,” *J. Sound Vib.*, vol. 357, 2015, doi: 10.1016/j.jsv.2015.04.037.

[32] P. D. McFadden and J. D. Smith, “Model for the vibration produced by a single point defect in a rolling element bearing,” *J. Sound Vib.*, vol. 96, no. 1, pp. 69–82, Sep. 1984, doi: 10.1016/0022-460X(84)90595-9.

[33] P. D. McFadden and J. D. Smith, “Vibration monitoring of rolling element bearings by the high-frequency resonance technique — a review,” *Tribol. Int.*, vol. 17, no. 1, pp. 3–10, Feb. 1984, doi: 10.1016/0301-679X(84)90076-8.

[34] N. Tandon and A. Choudhury, “An analytical model for the prediction of the vibration response of rolling element bearings due to a localized defect,” *J. Sound Vib.*, vol. 205, pp. 275–292, 1997.

[35] P. D. McFadden and J. D. Smith, “The vibration produced by multiple point defects in a rolling element bearing,” *J. Sound Vib.*, vol. 98, no. 2, pp. 263–273, Jan. 1985, doi: 10.1016/0022-460X(85)90390-6.

[36] Y.-T. Su and S.-J. Lin, “On initial fault detection of a tapered roller bearing: Frequency domain analysis,” *J. Sound Vib.*, vol. 155, no. 1, pp. 75–84, May 1992, doi: 10.1016/0022-460X(92)90646-F.

[37] R. B. Randall, J. Antoni, and S. Chobsaard, “The relationship between spectral correlation and envelope analysis in the diagnostics of bearing faults and other cyclostationary machine signals,” *Mech. Syst. Signal Process.*, vol. 15, no. 5, pp. 945–

962, 2001, doi: 10.1006/mssp.2001.1415.

[38] J. Antoni and R. B. Randall, "Differential diagnosis of gear and bearing faults," *J. Vib. Acoust.*, vol. 124, no. 2, p. 165, Apr. 2002, doi: 10.1115/1.1456906.

[39] J. Antoni and R. B. Randall, "A Stochastic Model for Simulation and Diagnostics of Rolling Element Bearings With Localized Faults," *J. Vib. Acoust.*, vol. 125, no. 3, p. 282, Jul. 2003, doi: 10.1115/1.1569940.

[40] J. Antoni, F. Bonnardot, A. Raad, and M. El Badaoui, "Cyclostationary modelling of rotating machine vibration signals," *Mech. Syst. Signal Process.*, vol. 18, no. 6, pp. 1285–1314, Nov. 2004, doi: 10.1016/S0888-3270(03)00088-8.

[41] M. Behzad, A. R. Bastami, and D. Mba, "A new model for estimating vibrations generated in the defective rolling element bearings," *J. Vib. Acoust. Trans. ASME*, vol. 133, no. 4, 2011, doi: 10.1115/1.4003595.

[42] A. Rohani Bastami and S. Vahid, "A comprehensive evaluation of the effect of defect size in rolling element bearings on the statistical features of the vibration signal," *Mech. Syst. Signal Process.*, vol. 151, p. 107334, 2021, doi: 10.1016/j.ymssp.2020.107334.

[43] I. K. Epps, "An Investigation into Vibrations by Faults in Rolling Element Bearings," University of Canterbury, 1991.

[44] M. J. Dowling, "Application of non-stationary analysis to machinery monitoring," in *IEEE International Conference on Acoustics Speech and Signal Processing*, 1993, pp. 59–62 vol.1. doi: 10.1109/ICASSP.1993.319054.

[45] N. Sawalhi and R. B. Randall, "Vibration response of spalled rolling element bearings: Observations, simulations and signal processing techniques to track the spall size," *Mech. Syst. Signal Process.*, vol. 25, no. 3, pp. 846–870, 2011, doi: 10.1016/j.ymssp.2010.09.009.

[46] A. Chen and T. R. Kurfess, "Signal processing techniques for rolling element bearing spall size estimation," *Mech. Syst. Signal Process.*, vol. 117, pp. 16–32, Feb. 2019, doi: 10.1016/J.YMSSP.2018.03.006.

[47] L. Cui, N. Wu, C. Ma, and H. Wang, "Quantitative fault analysis of roller bearings based on a novel matching pursuit method with a new step-impulse dictionary," *Mech. Syst. Signal Process.*, vol. 68–69, pp. 34–43, Feb. 2016, doi: 10.1016/J.YMSSP.2015.05.032.

[48] M. Luo, Y. Guo, X. Wu, and J. Na, "An analytical model for estimating spalled zone size of rolling element bearing based on dual-impulse time separation," *J. Sound Vib.*, vol. 453, pp. 87–102, Aug. 2019, doi: 10.1016/J.JSV.2019.04.014.

[49] D. Petersen and C. Howard, "Bearing defect size estimation for extended raceway defects," pp. 1–10, 2014, doi: 10.1143/PTP.70.654.

[50] N. Sawalhi, W. Wang, and A. Becker, "Vibration signal processing for spall size estimation in rolling element bearings using autoregressive inverse filtration combined with bearing signal synchronous averaging," *Adv. Mech. Eng.*, vol. 9, no. 5, pp. 1–20, 2017, doi: 10.1177/1687814017703007.

[51] A. Moazen-ahmadi and C. Q. Howard, "A defect size estimation method based on operational speed and path of rolling elements in defective bearings," *J. Sound Vib.*, vol. 385, pp. 138–148, 2016, doi: 10.1016/j.jsv.2016.09.014.

[52] N. Sawalhi and R. B. Randall, "Simulating gear and bearing interactions in the presence of faults: Part I. The combined gear bearing dynamic model and the simulation of localised bearing faults," *Mech. Syst. Signal Process.*, vol. 22, no. 8, pp. 1924–1951, Nov. 2008, doi: 10.1016/J.YMSSP.2007.12.001.

[53] A. Rafsanjani, S. Abbasion, A. Farshidianfar, and H. Moeenfard, "Nonlinear dynamic modeling of surface defects in rolling element bearing systems," *J. Sound Vib.*, vol. 319, no. 3–5, pp. 1150–1174, 2009, doi: 10.1016/j.jsv.2008.06.043.

[54] V. N. Patel, N. Tandon, and R. K. Pandey, "A dynamic model for vibration studies of deep groove ball bearings considering single and multiple defects in races," *J. Tribol.*, vol. 132, no. 4, p. 041101, Oct. 2010, doi: 10.1115/1.4002333.

[55] M. Nakhaeinejad and M. D. Bryant, "Dynamic Modeling of Rolling Element Bearings With Surface Contact Defects Using Bond Graphs," *J. Tribol.*, vol. 133, no. 1, p. 011102, Jan. 2011, doi: 10.1115/1.4003088.

[56] S. Zhao, L. Liang, G. Xu, J. Wang, and W. Zhang, "Quantitative diagnosis of a spall-like fault of a rolling element bearing by empirical mode decomposition and the approximate entropy method," *Mech. Syst. Signal Process.*, vol. 40, no. 1, pp. 154–177, 2013, doi: 10.1016/j.ymssp.2013.04.006.

[57] L. Niu, H. Cao, Z. He, and Y. Li, "Dynamic modeling and vibration response simulation for high speed rolling ball bearings with localized surface defects in raceways," *J. Manuf. Sci. Eng. Trans. ASME*, vol. 136, no. 4, pp. 1–16, 2014, doi: 10.1115/1.4027334.

[58] I. El-Thalji and E. Jantunen, "A summary of fault modelling and predictive health monitoring of rolling element bearings," *Mech. Syst. Signal Process.*, vol. 60, pp. 252–272, 2015, doi: 10.1016/j.ymssp.2015.02.008.

[59] A. Moazen Ahmadi, D. Petersen, and C. Howard, "A nonlinear dynamic vibration model of defective bearings – The importance of modelling the finite size of rolling elements," *Mech. Syst. Signal Process.*, vol. 52–53, pp. 309–326, Feb. 2015, doi: 10.1016/J.YMSSP.2014.06.006.

[60] F. Larizza, A. Moazen-Ahmadi, C. Q. Howard, and S. Grainger, "The importance of bearing stiffness and load when estimating the size of a defect in a rolling element bearing," *Struct. Heal. Monit.*, p. 147592171880880, Oct. 2018, doi: 10.1177/1475921718808805.

[61] F. Larizza, C. Q. Howard, S. Grainger, and W. Wang, "A nonlinear dynamic vibration model of a defective bearing: the importance of modelling the angle of the leading and trailing edges of a defect," *Struct. Heal. Monit.*, 2020, doi: 10.1177/1475921720963950.

[62] M. Luo, Y. Guo, H. Andre, X. Wu, and J. Na, "Dynamic modeling and quantitative diagnosis for dual-impulse behavior of rolling element bearing with a spall on inner race," *Mech. Syst. Signal Process.*, vol. 158, p. 107711, 2021, doi: 10.1016/j.ymssp.2021.107711.

[63] S. Su, H. Cao, and Y. Zhang, "Dynamic modeling and characteristics analysis of cylindrical roller bearing with the surface texture on raceways," *Mech. Syst. Signal Process.*, vol. 158, p. 107709, 2021, doi: 10.1016/j.ymssp.2021.107709.

[64] S. Fukata, E. H. Gad, T. Kondou, T. Ayabe, and H. Tamura, “On the radial vibration of ball bearings : computer simulation,” *Bull. JSME*, vol. 28, no. 239, pp. 899–904, 1985, doi: 10.1299/jsme1958.28.899.

[65] N. S. Feng, E. J. Hahn, and R. B. Randall, “Using transient analysis software to simulate vibration signals due to rolling element bearing defects,” in *Applied Mechanics: Progress and Applications*, World Scientific, 2002, pp. 689–694.

[66] J. Sopanen and A. Mikkola, “Dynamic model of a deep-groove ball bearing including localized and distributed defects. Part 1: Theory,” *Proc. Inst. Mech. Eng. Part K J. Multi-body Dyn.*, vol. 217, no. 3, pp. 201–211, Sep. 2003, doi: 10.1243/14644190360713551.

[67] H. Arslan and N. Aktürk, “An investigation of rolling element vibrations caused by local defects,” *J. Tribol.*, vol. 130, no. 4, pp. 1–12, 2008, doi: 10.1115/1.2958070.

[68] A. Ashtekar, F. Sadeghi, and L. E. Stacke, “A new approach to modeling surface defects in bearing dynamics simulations,” *J. Tribol.*, vol. 130, no. 4, pp. 1–8, 2008, doi: 10.1115/1.2959106.

[69] M. Cao and J. Xiao, “A comprehensive dynamic model of double-row spherical roller bearing-Model development and case studies on surface defects, preloads, and radial clearance,” *Mech. Syst. Signal Process.*, vol. 22, no. 2, pp. 467–489, 2008, doi: 10.1016/j.ymssp.2007.07.007.

[70] N. Sawalhi and R. B. Randall, “Simulating gear and bearing interactions in the presence of faults: Part II: Simulation of the vibrations produced by extended bearing faults,” *Mech. Syst. Signal Process.*, vol. 22, no. 8, pp. 1952–1966, Nov. 2008, doi: 10.1016/J.YMSSP.2007.12.002.

[71] P. K. Gupta, *Advanced dynamics of rolling elements*. Springer Science & Business Media, 1984.

[72] S. Singh, U. Köpke, C. Howard, and D. Petersen, “Impact generating mechanisms in damaged rolling element bearings,” *Proc. Acoust. 2013-Victor Harb.*, no. 2, pp. 1–7, 2013, doi: 10.1177/0363546507307756.

[73] S. P. Harsha, "Nonlinear dynamic analysis of an unbalanced rotor supported by roller bearing," *Chaos, Solitons & Fractals*, vol. 26, no. 1, pp. 47–66, Oct. 2005, doi: 10.1016/J.CHAOS.2004.12.014.

[74] S. Singh, "Explicit dynamics finite element modelling of defective rolling element bearings," University of Adelaide, 2014.

[75] Z. Kiral and H. Karagülle, "Simulation and analysis of vibration signals generated by rolling element bearing with defects," *Tribol. Int.*, vol. 36, no. 9, pp. 667–678, Sep. 2003, doi: 10.1016/S0301-679X(03)00010-0.

[76] Z. Kıral and H. Karagülle, "Vibration analysis of rolling element bearings with various defects under the action of an unbalanced force," *Mech. Syst. Signal Process.*, vol. 20, no. 8, pp. 1967–1991, Nov. 2006, doi: 10.1016/J.YMSSP.2005.05.001.

[77] F. Cheli and G. Diana, *Advanced dynamics of mechanical systems*. London: Springer, 2015. doi: 10.1007/978-3-319-18200-1.

[78] International Standard, "ISO 10816-3 Industrial machines with nominal power above 15 kW and nominal speeds between 120 r/min and 15 000 r/min when measured in situ," 2009.

[79] I. El-Thalji and E. Jantunen, "Fault analysis of the wear fault development in rolling bearings," *Eng. Fail. Anal.*, vol. 57, pp. 470–482, Nov. 2015, doi: 10.1016/J.ENGFAILANAL.2015.08.013.

[80] W. S. Siew, W. A. Smith, Z. Peng, and R. B. Randall, "Fault severity trending in rolling element bearings," 2015.

[81] N. Li, Y. Lei, J. Lin, and S. X. Ding, "An Improved Exponential Model for Predicting Remaining Useful Life of Rolling Element Bearings," *IEEE Trans. Ind. Electron.*, vol. 62, no. 12, pp. 7762–7773, 2015, doi: 10.1109/TIE.2015.2455055.

[82] Y. Li, S. Billington, C. Zhang, T. Kurfess, S. Danyluk, and S. Liang, "Adaptive prognostics for rolling element bearing condition," *Mech. Syst. Signal Process.*, vol. 13, no. 1, pp. 103–113, Jan. 1999, doi: 10.1006/MSSP.1998.0183.

[83] H. V. Liew and T. C. Lim, “Analysis of time-varying rolling element bearing characteristics,” *J. Sound Vib.*, vol. 283, no. 3–5, pp. 1163–1179, 2005, doi: 10.1016/j.jsv.2004.06.022.

[84] R. Li, P. Sopon, and D. He, “Fault features extraction for bearing prognostics,” *J. Intell. Manuf.*, vol. 23, no. 2, pp. 313–321, Apr. 2012, doi: 10.1007/s10845-009-0353-z.

[85] D. Wang, “Prognostics and Health Management : A Review of Vibration Based Bearing and Gear Health Indicators,” *IEEE Access*, vol. 6, pp. 665–676, 2018, doi: 10.1109/ACCESS.2017.2774261.

[86] J. Li, X. Chen, and Z. He, “Adaptive stochastic resonance method for impact signal detection based on sliding window,” *Mech. Syst. Signal Process.*, vol. 36, no. 2, pp. 240–255, Apr. 2013, doi: 10.1016/J.YMSSP.2012.12.004.

[87] S. Sun, Y. Guo, and X. Wu, “Double impulse phenomenon extraction of outer race spalled rolling element bearings based on acoustic emission signals,” *Zhendong yu Chongji/Journal Vib. Shock*, vol. 36, no. 4, pp. 1931–1935, 2017, doi: 10.13465/j.cnki.jvs.2017.04.001.

[88] D. Wang, X. Zhao, L.-L. Kou, Y. Qin, Y. Zhao, and K.-L. Tsui, “A simple and fast guideline for generating enhanced/squared envelope spectra from spectral coherence for bearing fault diagnosis,” *Mech. Syst. Signal Process.*, vol. 122, pp. 754–768, May 2019, doi: 10.1016/J.YMSSP.2018.12.055.

[89] P. Borghesani, P. Pennacchi, and S. Chatterton, “The relationship between kurtosis- and envelope-based indexes for the diagnostic of rolling element bearings,” *Mech. Syst. Signal Process.*, vol. 43, no. 1–2, pp. 25–43, Feb. 2014, doi: 10.1016/J.YMSSP.2013.10.007.

[90] P. Gupta and M. K. Pradhan, “Fault detection analysis in rolling element bearing: A review,” in *Materials Today: Proceedings*, Jan. 2017, vol. 4, no. 2, pp. 2085–2094. doi: 10.1016/j.matpr.2017.02.054.

[91] W. A. Smith and R. B. Randall, “Rolling element bearing diagnostics using the Case Western Reserve University data: A benchmark study,” *Mech. Syst. Signal Process.*, vol.

64–65, no. May 2018, pp. 100–131, 2015, doi: 10.1016/j.ymssp.2015.04.021.

[92] J. Antoni, "Cyclostationarity by examples," *Mech. Syst. Signal Process.*, vol. 23, no. 4, pp. 987–1036, May 2009, doi: 10.1016/J.YMSSP.2008.10.010.

[93] R. B. Randall and J. Antoni, "Rolling element bearing diagnostics-A tutorial," *Mech. Syst. Signal Process.*, 2011, doi: 10.1016/j.ymssp.2010.07.017.

[94] J. Antoni and P. Borghesani, "A statistical methodology for the design of condition indicators," *Mech. Syst. Signal Process.*, vol. 114, pp. 290–327, 2019, doi: 10.1016/j.ymssp.2018.05.012.

[95] G. Zak, A. Wylomanska, and R. Zimroz, "Alpha-stable distribution based methods in the analysis of the crusher vibration signals for fault detection," *IFAC-PapersOnLine*, vol. 50, no. 1, 2017, doi: 10.1016/j.ifacol.2017.08.697.

[96] G. Zak, A. Wyłomańska, and R. Zimroz, "Periodically impulsive behavior detection in noisy observation based on generalized fractional order dependency map," *Applied Acoustics*, 2017. doi: 10.1016/j.apacoust.2017.05.003.

[97] J. Antoni and R. B. Randall, "Unsupervised noise cancellation for vibration signals: part I—evaluation of adaptive algorithms," *Mech. Syst. Signal Process.*, vol. 18, no. 1, pp. 89–101, Jan. 2004, doi: 10.1016/S0888-3270(03)00012-8.

[98] N. Sawalhi and R. B. Randall, "Spectral kurtosis optimization for rolling element bearings," *Proc. - 8th Int. Symp. Signal Process. its Appl. ISSPA 2005*, vol. 2, no. February, pp. 839–842, 2005, doi: 10.1109/ISSPA.2005.1581069.

[99] J. Antoni and R. B. Randall, "The spectral kurtosis: application to the vibratory surveillance and diagnostics of rotating machines," *Mech. Syst. Signal Process.*, vol. 20, no. 2, pp. 308–331, Feb. 2006, doi: 10.1016/J.YMSSP.2004.09.002.

[100] A. Rai and S. H. Upadhyay, "A review on signal processing techniques utilized in the fault diagnosis of rolling element bearings," *Tribol. Int.*, vol. 96, pp. 289–306, Apr. 2016, doi: 10.1016/J.TRIBOINT.2015.12.037.

[101] J. Antoni and R. B. Randall, "Unsupervised noise cancellation for vibration signals: part

II—a novel frequency-domain algorithm," *Mech. Syst. Signal Process.*, vol. 18, no. 1, pp. 103–117, Jan. 2004, doi: 10.1016/S0888-3270(03)00013-X.

[102] N. Sawalhi, R. B. Randall, and H. Endo, "The enhancement of fault detection and diagnosis in rolling element bearings using minimum entropy deconvolution combined with spectral kurtosis," *Mech. Syst. Signal Process.*, vol. 21, no. 6, pp. 2616–2633, 2007, doi: 10.1016/j.ymssp.2006.12.002.

[103] R. B. Randall and J. Antoni, "Rolling element bearing diagnostics-A tutorial," *Mech. Syst. Signal Process.*, vol. 25, no. 2, pp. 485–520, 2011, doi: 10.1016/j.ymssp.2010.07.017.

[104] P. Borghesani, R. Ricci, S. Chatterton, and P. Pennacchi, "A new procedure for using envelope analysis for rolling element bearing diagnostics in variable operating conditions," *Mech. Syst. Signal Process.*, vol. 38, no. 1, pp. 23–35, Jul. 2013, doi: 10.1016/j.ymssp.2012.09.014.

[105] W. A. Smith and R. B. Randall, "Rolling element bearing diagnostics using the Case Western Reserve University data: A benchmark study," *Mech. Syst. Signal Process.*, vol. 64–65, pp. 100–131, Dec. 2015, doi: 10.1016/J.YMSSP.2015.04.021.

[106] J. Zheng, H. Pan, and J. Cheng, "Rolling bearing fault detection and diagnosis based on composite multiscale fuzzy entropy and ensemble support vector machines," *Mech. Syst. Signal Process.*, vol. 85, no. January 2015, pp. 746–759, 2017, doi: 10.1016/j.ymssp.2016.09.010.

[107] Q. Ni, J. C. Ji, K. Feng, and B. Halkon, "A novel correntropy-based band selection method for the fault diagnosis of bearings under fault-irrelevant impulsive and cyclostationary interferences," *Mech. Syst. Signal Process.*, vol. 153, p. 107498, 2021, doi: 10.1016/j.ymssp.2020.107498.

[108] J. Antoni, "Fast computation of the kurtogram for the detection of transient faults," *Mech. Syst. Signal Process.*, vol. 21, no. 1, pp. 108–124, Jan. 2007, doi: 10.1016/J.YMSSP.2005.12.002.

[109] K. R. Fyfe and E. D. S. Munck, "Analysis of computed order tracking," *Mech. Syst.*

*Signal Process.*, vol. 11, no. 2, pp. 187–205, Mar. 1997, doi: 10.1006/MSSP.1996.0056.

[110] P. Borghesani, P. Pennacchi, R. B. Randall, and R. Ricci, "Order tracking for discrete-random separation in variable speed conditions," *Mech. Syst. Signal Process.*, vol. 30, pp. 1–22, 2012, doi: 10.1016/j.ymssp.2012.01.015.

[111] M. D. Coats, N. Sawalhi, and R. B. Randall, "Extraction of tacho information from a vibration signal for improved synchronous averaging," 2009.

[112] D. Siegel, H. Al-Atat, V. Shauche, L. Liao, J. Snyder, and J. Lee, "Novel method for rolling element bearing health assessment—A tachometer-less synchronously averaged envelope feature extraction technique," *Mech. Syst. Signal Process.*, vol. 29, pp. 362–376, May 2012, doi: 10.1016/J.YMSSP.2012.01.003.

[113] C. Peeters, J. Helsen, and J. Antoni, "Blind vibration filtering using envelope linear prediction for fault detection without knowledge of machine kinematics", Accessed: Jul. 31, 2019. [Online]. Available: https://www.researchgate.net/publication/334481144

[114] D. Wang, P. W. Tse, and K. L. Tsui, "An enhanced Kurtogram method for fault diagnosis of rolling element bearings," *Mech. Syst. Signal Process.*, vol. 35, no. 1–2, pp. 176–199, 2013, doi: 10.1016/j.ymssp.2012.10.003.

[115] Y. Lei, J. Lin, Z. He, and Y. Zi, "Application of an improved kurtogram method for fault diagnosis of rolling element bearings," *Mech. Syst. Signal Process.*, vol. 25, no. 5, pp. 1738–1749, Jul. 2011, doi: 10.1016/J.YMSSP.2010.12.011.

[116] T. Barszcz and A. Jabłoński, "A novel method for the optimal band selection for vibration signal demodulation and comparison with the Kurtogram," *Mech. Syst. Signal Process.*, 2011, doi: 10.1016/j.ymssp.2010.05.018.

[117] W. A. Smith, P. Borghesani, Q. Ni, K. Wang, and Z. Peng, "Optimal demodulation-band selection for envelope-based diagnostics: A comparative study of traditional and novel tools," *Mech. Syst. Signal Process.*, vol. 134, 2019, doi: 10.1016/j.ymssp.2019.106303.

[118] A. K. S. Jardine, D. Lin, and D. Banjevic, "A review on machinery diagnostics and prognostics implementing condition-based maintenance," *Mechanical Systems and*

*Signal Processing*, vol. 20, no. 7. pp. 1483–1510, Oct. 2006. doi: 10.1016/j.ymssp.2005.09.012.

[119] Y. Lei, N. Li, L. Guo, N. Li, T. Yan, and J. Lin, "Machinery health prognostics: A systematic review from data acquisition to RUL prediction," *Mech. Syst. Signal Process.*, vol. 104, pp. 799–834, May 2018, doi: 10.1016/J.YMSSP.2017.11.016.

[120] A. Heng, S. Zhang, A. C. C. Tan, and J. Mathew, "Rotating machinery prognostics: State of the art, challenges and opportunities," *Mech. Syst. Signal Process.*, vol. 23, no. 3, pp. 724–739, 2009, doi: 10.1016/j.ymssp.2008.06.009.

[121] N. Gebraeel, M. Lawley, R. Liu, and V. Parmeshwaran, "Residual Life Predictions From Vibration-Based Degradation Signals: A Neural Network Approach," *IEEE Trans. Ind. Electron.*, vol. 51, no. 3, pp. 694–700, Jun. 2004, doi: 10.1109/TIE.2004.824875.

[122] A. H. Elwany and N. Z. Gebraeel, "Sensor-driven prognostic models for equipment replacement and spare parts inventory," *IIE Trans. (Institute Ind. Eng.*, vol. 40, no. 7, pp. 629–639, Jul. 2008, doi: 10.1080/07408170701730818.

[123] M. Gaperin, D. Juriić, P. Bokoski, and J. Viintin, "Model-based prognostics of gear health using stochastic dynamical models," *Mech. Syst. Signal Process.*, vol. 25, no. 2, pp. 537–548, Feb. 2011, doi: 10.1016/j.ymssp.2010.07.003.

[124] E. Brusa, F. Bruzzone, C. Delprete, L. Gianpio, D. Maggio, and C. Rosso, "A Proposal of a Technique for Correlating Defect Dimensions to Vibration Amplitude in Bearing Monitoring," pp. 1–14, 2011.

[125] A. Malhi, R. Yan, and R. X. Gao, "Prognosis of defect propagation based on recurrent neural networks," *IEEE Trans. Instrum. Meas.*, vol. 60, no. 3, pp. 703–711, 2011, doi: 10.1109/TIM.2010.2078296.

[126] J. Yu, "Bearing performance degradation assessment using locality preserving projections and Gaussian mixture models," *Mech. Syst. Signal Process.*, vol. 25, no. 7, pp. 2573–2588, 2011, doi: 10.1016/j.ymssp.2011.02.006.

[127] L. Ma, J. S. Kang, and C. Y. Zhao, "Research on condition monitoring of bearing health

using vibration data," *Appl. Mech. Mater.*, vol. 226–228, pp. 340–344, 2012, doi: 10.4028/www.scientific.net/AMM.226-228.340.

[128] Yuning Qian, R. Yan, and Mengxiao Shan, "Damage assessment of mechanical systems based on recurrence quantification analysis," in *Proceedings of the IEEE 2012 Prognostics and System Health Management Conference (PHM-2012 Beijing)*, May 2012, pp. 1–5. doi: 10.1109/PHM.2012.6228835.

[129] Y. Wang, S. Kang, Y. Jiang, G. Yang, L. Song, and V. I. Mikulovich, "Classification of fault location and the degree of performance degradation of a rolling bearing based on an improved hyper-sphere-structured multi-class support vector machine," in *Mechanical Systems and Signal Processing*, May 2012, vol. 29, pp. 404–414. doi: 10.1016/j.ymssp.2011.11.015.

[130] F. Camci, K. Medjaher, N. Zerhouni, and P. Nectoux, "Feature Evaluation for Effective Bearing Prognostics," *Qual. Reliab. Eng. Int.*, vol. 29, no. 4, pp. 477–486, Jun. 2013, doi: 10.1002/qre.1396.

[131] X. Chen, Z. Shen, Z. He, C. Sun, and Z. Liu, "Remaining life prognostics of rolling bearing based on relative features and multivariable support vector machine," *Proc. Inst. Mech. Eng. Part C J. Mech. Eng. Sci.*, vol. 227, no. 12, pp. 2849–2860, Dec. 2013, doi: 10.1177/0954406212474395.

[132] K. Medjaher, N. Zerhouni, and J. Baklouti, "Data-driven prognostics based on health indicator construction: Application to PRONOSTIA's data," in *2013 European Control Conference, ECC 2013*, 2013, pp. 1451–1456. doi: 10.23919/ecc.2013.6669223.

[133] J. Lee, F. Wu, W. Zhao, M. Ghaffari, L. Liao, and D. Siegel, "Prognostics and health management design for rotary machinery systems—Reviews, methodology and applications," *Mech. Syst. Signal Process.*, vol. 42, no. 1–2, pp. 314–334, Jan. 2014, doi: 10.1016/J.YMSSP.2013.06.004.

[134] X. Zhang, J. Kang, E. Bechhoefer, and H. Teng, "Enhanced bearing fault detection and degradation analysis based on narrowband interference cancellation," *Int. J. Syst. Assur. Eng. Manag.*, vol. 5, no. 4, pp. 645–650, Dec. 2014, doi: 10.1007/s13198-014-0217-6.

[135] J. Zhu, T. Nostrand, C. Spiegel, and B. Morton, "Survey of Condition Indicators for Condition Monitoring Systems," *Annu. Conf. Progn. Heal. Manag. Soc.*, vol. 5, pp. 1–13, 2014.

[136] W. S. Siew, "Fault Severity Analysis of Rolling Bearings Using Vibration Techniques," University of New South Wales, 2015.

[137] Z. X. Zhang, X. S. Si, and C. H. Hu, "An Age- and State-Dependent Nonlinear Prognostic Model for Degrading Systems," *IEEE Trans. Reliab.*, vol. 64, no. 4, pp. 1214–1228, 2015, doi: 10.1109/TR.2015.2419220.

[138] W. Zhea, "Rolling bearing fault evolution based on vibration time-domain parameters," *Key Eng. Mater.*, vol. 693, pp. 1412–1418, 2016, doi: 10.4028/www.scientific.net/KEM.693.1412.

[139] Z. Liu, M. J. Zuo, and Y. Qin, "Remaining useful life prediction of rolling element bearings based on health state assessment," *Proc. Inst. Mech. Eng. Part C J. Mech. Eng. Sci.*, vol. 230, no. 2, pp. 314–330, 2016, doi: 10.1177/0954406215590167.

[140] P. Shakya, A. K. Darpe, and M. S. Kulkarni, "Bearing diagnosis using proximity probe and accelerometer," *Meas. J. Int. Meas. Confed.*, vol. 80, pp. 190–200, 2016, doi: 10.1016/j.measurement.2015.11.029.

[141] A. Sharma, M. Amarnath, and P. Kankar, "Feature extraction and fault severity classification in ball bearings," *J. Vib. Control*, vol. 22, no. 1, pp. 176–192, Jan. 2016, doi: 10.1177/1077546314528021.

[142] Y. Lei, N. Li, S. Gontarz, J. Lin, S. Radkowski, and J. Dybala, "A Model-Based Method for Remaining Useful Life Prediction of Machinery," *IEEE Trans. Reliab.*, vol. 65, no. 3, pp. 1314–1326, 2016, doi: 10.1109/TR.2016.2570568.

[143] A. Rohani Bastami and S. Vahid, "A comprehensive evaluation of the effect of defect size in rolling element bearings on the statistical features of the vibration signal," *Mech. Syst. Signal Process.*, vol. 151, 2021, doi: 10.1016/j.ymssp.2020.107334.

[144] A. P. Daga, A. Fasana, S. Marchesiello, and L. Garibaldi, "The Politecnico di Torino

rolling bearing test rig: Description and analysis of open access data," *Mech. Syst. Signal Process.*, vol. 120, pp. 252–273, 2019, doi: 10.1016/j.ymssp.2018.10.010.

[145] Z. Peng, S. Zhuang, and P. Borghesani, "Tribological Investigation on a Degradation Process of Contact Fatigue of Rolling Bearings and Influence of the Shape and Size of Initial Defect," *Tribol. Int.*, 2021.

[146] A. Mauricio, W. Smith, R. Randall, J. Antoni, and K. Gryllias, "Cyclostationary-based tools for bearing diagnostics of helicopter planetary gearboxes," in *AIAC18: 18th Australian international aerospace congress (2019): HUMS-11th defence science and technology (DST) international conference on health and usage monitoring (HUMS 2019): ISSFD-27th international symposium on space flight dynamics (ISSFD)*, 2019, p. 837.

[147] N. Tandon, "A comparison of some vibration parameters for the condition monitoring of rolling element bearings," *Measurement*, vol. 12, no. 3, pp. 285–289, Jan. 1994, doi: 10.1016/0263-2241(94)90033-7.

[148] N. Gebraeel, M. Lawley, R. Liu, and V. Parmeshwaran, "Residual life predictions from vibration-based degradation signals: A neural network approach," *IEEE Trans. Ind. Electron.*, vol. 51, no. 3, pp. 694–700, Jun. 2004, doi: 10.1109/TIE.2004.824875.

[149] W. Smith, C. Hu, R. B. Randall, and Z. Peng, "Vibration-Based spall size tracking in rolling element bearings," *Mech. Mach. Sci.*, vol. 21, pp. 587–597, 2015, doi: 10.1007/978-3-319-06590-8.

[150] P. Borghesani, P. Pennacchi, R. B. Randall, N. Sawalhi, and R. Ricci, "Application of cepstrum pre-whitening for the diagnosis of bearing faults under variable speed conditions," *Mech. Syst. Signal Process.*, vol. 36, no. 2, pp. 370–384, 2013, doi: 10.1016/j.ymssp.2012.11.001.

[151] A. Chen and T. R. Kurfess, "A new model for rolling element bearing defect size estimation," *Measurement*, vol. 114, pp. 144–149, Jan. 2018, doi: 10.1016/J.MEASUREMENT.2017.09.018.

[152] G. Kogan, J. Bortman, and R. Klein, "A new model for spall-rolling-element interaction,"

*Nonlinear Dyn.*, vol. 87, no. 1, pp. 219–236, Jan. 2017, doi: 10.1007/s11071-016-3037-1.

[153] N. Sawalhi, W. Wang, and A. Becker, "Vibration signal processing using cepstrum editing technique to enhance spall-related vibration features in rolling element bearings," *Int. J. Mech. Eng. Robot. Res.*, vol. 8, no. 1, pp. 65–68, 2019, doi: 10.18178/ijmerr.8.1.65-68.

[154] M. A. Ismail, A. Bierig, and N. Sawalhi, "Automated vibration-based fault size estimation for ball bearings using Savitzky–Golay differentiators," *J. Vib. Control*, vol. 24, no. 18, pp. 4297–4315, Sep. 2018, doi: 10.1177/1077546317723227.

[155] W. Wang, N. Sawalhi, and A. Becker, "Size estimation for naturally occurring bearing faults using synchronous averaging of vibration signals," *J. Vib. Acoust.*, vol. 138, no. 5, p. 051015, Jul. 2016, doi: 10.1115/1.4033776.

[156] M. A. A. Ismail and N. Sawalhi, "Vibration response characterisation and fault-size estimation of spalled ball bearings," *Insight Non-Destructive Test. Cond. Monit.*, vol. 59, no. 3, pp. 149–154, 2017, doi: 10.1784/insi.2017.59.3.149.

[157] G. Kogan, R. Klein, and J. Bortman, "A physics-based algorithm for the estimation of bearing spall width using vibrations," *Mech. Syst. Signal Process.*, vol. 104, pp. 398–414, May 2018, doi: 10.1016/J.YMSSP.2017.11.011.

[158] P. Feng, P. Borghesani, W. A. Smith, R. B. Randall, and Z. Peng, "A Review on the Relationships Between Acoustic Emission, Friction and Wear in Mechanical Systems," *Appl. Mech. Rev.*, vol. 72, no. 2, Mar. 2020, doi: 10.1115/1.4044799.

[159] M. Elforjani and D. Mba, "Accelerated natural fault diagnosis in slow speed bearings with Acoustic Emission," *Eng. Fract. Mech.*, vol. 77, no. 1, pp. 112–127, Jan. 2010, doi: 10.1016/j.engfracmech.2009.09.016.

[160] M. Elforjani and D. Mba, "Monitoring the onset and propagation of natural degradation process in a slow speed rolling element bearing with acoustic emission," *J. Vib. Acoust. Trans. ASME*, vol. 130, no. 4, Aug. 2008, doi: 10.1115/1.2948413.

[161] D. Mba, "The use of acoustic emission for estimation of bearing defect size," *J. Fail. Anal. Prev.*, vol. 8, no. 2, pp. 188–192, 2008, doi: 10.1007/s11668-008-9119-8.

[162] A. B. Ming, W. Zhang, Z. Y. Qin, and F. L. Chu, "Dual-Impulse Response Model for the Acoustic Emission Produced by a Spall and the Size Evaluation in Rolling Element Bearings," *IEEE Trans. Ind. Electron.*, vol. 62, no. 10, pp. 6606–6615, 2015, doi: 10.1109/TIE.2015.2463767.

[163] F. Hemmati, W. Orfali, and M. S. Gadala, "Roller bearing acoustic signature extraction by wavelet packet transform, applications in fault detection and size estimation," *Appl. Acoust.*, vol. 104, pp. 101–118, 2016, doi: 10.1016/j.apacoust.2015.11.003.

[164] A. M. Al-Ghamd and D. Mba, "A comparative experimental study on the use of acoustic emission and vibration analysis for bearing defect identification and estimation of defect size," *Mech. Syst. Signal Process.*, vol. 20, no. 7, pp. 1537–1571, Oct. 2006, doi: 10.1016/j.ymssp.2004.10.013.

[165] A. B. Ming, W. Zhang, Z. Y. Qin, and F. L. Chu, "Dual-Impulse Response Model for the Acoustic Emission Produced by a Spall and the Size Evaluation in Rolling Element Bearings," *IEEE Trans. Ind. Electron.*, vol. 62, no. 10, pp. 6606–6615, Oct. 2015, doi: 10.1109/TIE.2015.2463767.

[166] W. Caesarendra, B. Kosasih, A. K. Tieu, H. Zhu, C. A. S. Moodie, and Q. Zhu, "Acoustic emission-based condition monitoring methods: Review and application for low speed slew bearing," *Mech. Syst. Signal Process.*, vol. 72–73, pp. 134–159, May 2016, doi: 10.1016/J.YMSSP.2015.10.020.

[167] Y. Li, F. Gu, G. Harris, A. Ball, N. Bennett, and K. Travis, "The measurement of instantaneous angular speed," *Mech. Syst. Signal Process.*, vol. 19, no. 4, pp. 786–805, Jul. 2005, doi: 10.1016/j.ymssp.2004.04.003.

[168] M. Feldman, "Hilbert transform in vibration analysis," *Mechanical Systems and Signal Processing*, vol. 25, no. 3. Academic Press, pp. 735–802, Apr. 01, 2011. doi: 10.1016/j.ymssp.2010.07.018.

[169] R. B. Randall and W. A. Smith, "Uses and mis-uses of energy operators for machine

diagnostics," *Mech. Syst. Signal Process.*, vol. 133, p. 106199, 2019, doi: 10.1016/j.ymssp.2019.06.017.

[170] A. Bourdon, S. Chesné, H. André, and D. Rémond, "Estimation of the size of a spall defect on a rolling bearing outer ring using Instantaneous Angular Speed measurements," Aug. 2014. doi: https://hal.archives-ouvertes.fr/hal-01074976.

[171] A. Bourdon, S. Chesné, H. André, and D. Rémond, "Reconstruction of angular speed variations in the angular domain to diagnose and quantify taper roller bearing outer race fault," *Mech. Syst. Signal Process.*, vol. 120, pp. 1–15, Apr. 2019, doi: 10.1016/J.YMSSP.2018.09.040.

[172] J. L. Gomez, A. Bourdon, H. André, and D. Rémond, "Modelling deep groove ball bearing localized defects inducing instantaneous angular speed variations," *Tribol. Int.*, vol. 98, pp. 270–281, Jun. 2016, doi: 10.1016/J.TRIBOINT.2016.02.032.

[173] L. Renaudin, F. Bonnardot, O. Musy, J. B. Doray, and D. Rémond, "Natural roller bearing fault detection by angular measurement of true instantaneous angular speed," in *Mechanical Systems and Signal Processing*, Oct. 2010, vol. 24, no. 7, pp. 1998–2011. doi: 10.1016/j.ymssp.2010.05.005.

[174] G. A. Skrimpas, K. S. Marhadi, and B. B. Jensen, "Automatic mechanical fault assessment of small wind energy systems in microgrids using electric signature analysis," *2013 4th IEEE/PES Innov. Smart Grid Technol. Eur. ISGT Eur. 2013*, pp. 1–5, 2013, doi: 10.1109/ISGTEurope.2013.6695293.

[175] X. Wu, C. Qiu, M. Xia, G. Cheng, and Z. Xue, "Research on the current feature of induction motor bearing fault based on phase modulation," *5th Int. Conf. Intell. Control Inf. Process. ICICIP 2014 - Proc.*, pp. 181–186, 2015, doi: 10.1109/ICICIP.2014.7010336.

[176] R. B. Randall, *Vibration-based Condition Monitoring*. Wiley, 2011. doi: 10.1002/9780470977668.ch1.

[177] Y. Peng, M. Dong, and M. J. Zuo, "Current status of machine prognostics in condition-based maintenance: A review," *Int. J. Adv. Manuf. Technol.*, vol. 50, no. 1–4, pp. 297–

313, 2010, doi: 10.1007/s00170-009-2482-0.

[178] Y. Li, S. Billington, C. Zhang, T. Kurfess, S. Danyluk, and S. Liang, "Dynamic prognostic prediction of defect propagation on rolling element Bearings," *Tribol. Trans.*, vol. 42, no. 2, pp. 385–392, Jan. 1999, doi: 10.1080/10402009908982232.

[179] P. Rycerz, A. Olver, and A. Kadiric, "Propagation of surface initiated rolling contact fatigue cracks in bearing steel," *Int. J. Fatigue*, vol. 97, pp. 29–38, Apr. 2017, doi: 10.1016/j.ijfatigue.2016.12.004.

[180] S. Marble and B. P. Morton, "Predicting the remaining life of propulsion system bearings," in *2006 IEEE Aerospace Conference*, pp. 1–8. doi: 10.1109/AERO.2006.1656121.

[181] M. Behzad, H. A. Arghan, A. R. Bastami, and M. J. Zuo, "Prognostics of rolling element bearings with the combination of Paris law and reliability method," *2017 Progn. Syst. Heal. Manag. Conf. PHM-Harbin 2017 - Proc.*, vol. 9, 2017, doi: 10.1109/PHM.2017.8079187.

[182] W. Caesarendra and T. Tjahjowidodo, "A review of feature extraction methods in vibration-based condition monitoring and its application for degradation trend estimation of low-speed slew bearing," *Machines*, vol. 5, no. 4, 2017, doi: 10.3390/machines5040021.

[183] J. Ben Ali, B. Chebel-Morello, L. Saidi, S. Malinowski, and F. Fnaiech, "Accurate bearing remaining useful life prediction based on Weibull distribution and artificial neural network," *Mech. Syst. Signal Process.*, vol. 56, pp. 150–172, May 2015, doi: 10.1016/j.ymssp.2014.10.014.

[184] B. Samanta and K. R. Al-Balushi, "Artificial neural network based fault diagnostics of rolling element bearings using time-domain features," *Mech. Syst. Signal Process.*, vol. 17, no. 2, pp. 317–328, Mar. 2003, doi: 10.1006/MSSP.2001.1462.

[185] N. Gebraeel, M. Lawley, R. Liu, and V. Parmeshwaran, "Residual life predictions from vibration-based degradation signals: A neural network approach," *IEEE Trans. Ind. Electron.*, vol. 51, no. 3, pp. 694–700, 2004, doi: 10.1109/TIE.2004.824875.

[186] Y. Lu, Z. Wang, R. Xie, J. Zhang, Z. Pan, and S. Y. Liang, "Bayesian optimized deep convolutional network for bearing diagnosis," *Int. J. Adv. Manuf. Technol.*, vol. 108, no. 1–2, pp. 313–322, 2020, doi: 10.1007/s00170-020-05390-y.

[187] X. Chen, Z. Shen, Z. He, C. Sun, and Z. Liu, "Remaining life prognostics of rolling bearing based on relative features and multivariable support vector machine," *Proc. Inst. Mech. Eng. Part C J. Mech. Eng. Sci.*, vol. 227, no. 12, pp. 2849–2860, 2013, doi: 10.1177/0954406212474395.

[188] D. A. Tobon-Mejia, K. Medjaher, N. Zerhouni, and G. Tripot, "A data-driven failure prognostics method based on mixture of gaussians hidden markov models," *IEEE Trans. Reliab.*, vol. 61, no. 2, pp. 491–503, 2012, doi: 10.1109/TR.2012.2194177.

[189] A. Kumar, Y. Zhou, C. P. Gandhi, R. Kumar, and J. Xiang, "Bearing defect size assessment using wavelet transform based Deep Convolutional Neural Network (DCNN)," *Alexandria Eng. J.*, vol. 59, no. 2, pp. 999–1012, 2020, doi: 10.1016/j.aej.2020.03.034.

[190] R. Zhao, R. Yan, Z. Chen, K. Mao, P. Wang, and R. X. Gao, "Deep learning and its applications to machine health monitoring," *Mech. Syst. Signal Process.*, vol. 115, pp. 213–237, Jan. 2019, doi: 10.1016/J.YMSSP.2018.05.050.

[191] M. R. Shahriar, P. Borghesani, and A. C. C. Tan, "Electrical Signature Analysis-Based Detection of External Bearing Faults in Electromechanical Drivetrains," *IEEE Trans. Ind. Electron.*, vol. 65, no. 7, pp. 5941–5950, 2018, doi: 10.1109/TIE.2017.2782240.

[192] J. Antoni, "On the benefits of the Wigner–Ville spectrum for analysing certain types of vibration signals," 2003.

[193] J. Antoni, "Cyclic spectral analysis in practice," *Mech. Syst. Signal Process.*, vol. 21, no. 2, pp. 597–630, Feb. 2007, doi: 10.1016/J.YMSSP.2006.08.007.

[194] H. Chang, P. Borghesani, W. A. Smith, and Z. Peng, "Application of surface replication combined with image analysis to investigate wear evolution on gear teeth – A case study," *Wear*, vol. 430–431, pp. 355–368, Jul. 2019, doi: 10.1016/J.WEAR.2019.05.024.

[195] I. K. Epps and H. McCallion, “An investigation into the characteristics of vibration excited by discrete faults in rolling element bearings,” 1994.

[196] F. Larizza, C. Q. Howard, S. Grainger, and W. Wang, “Modelling and defect size estimation of a defective bearing,” *Proc. Acoust.*, vol. 7, no. 9, 2018.

[197] F. Larizza, C. Q. Howard, and S. Grainger, “Defect size estimation in rolling element bearings with angled leading and trailing edges,” *Struct. Heal. Monit.*, p. 147592172093829, Aug. 2020, doi: 10.1177/1475921720938296.

[198] J. Qiu, B. B. Seth, S. Y. Liang, and C. Zhang, “Damage mechanics approach for bearing lifetime prognostics,” *Mech. Syst. Signal Process.*, vol. 16, no. 5, pp. 817–829, 2002, doi: 10.1006/mssp.2002.1483.

[199] S. Singh, U. G. Köpke, C. Q. Howard, and D. Petersen, “Analyses of contact forces and vibration response for a defective rolling element bearing using an explicit dynamics finite element model,” *J. Sound Vib.*, vol. 333, no. 21, pp. 5356–5377, 2014, doi: 10.1016/j.jsv.2014.05.011.

[200] L. Cohen, *Time-frequency analysis*, vol. 778. Prentice hall, 1995.

[201] J. Antoni, “Cyclostationarity by examples,” *Mech. Syst. Signal Process.*, vol. 23, no. 4, pp. 987–1036, May 2009, doi: 10.1016/J.YMSSP.2008.10.010.

[202] F. Bonnardot, M. El Badaoui, R. B. Randall, J. Danière, and F. Guillet, “Use of the acceleration signal of a gearbox in order to perform angular resampling (with limited speed fluctuation),” *Mech. Syst. Signal Process.*, vol. 19, no. 4, pp. 766–785, Jul. 2005, doi: 10.1016/j.ymssp.2004.05.001.

[203] B. Eftekharnejad, M. R. Carrasco, B. Charnley, and D. Mba, “The application of spectral kurtosis on Acoustic Emission and vibrations from a defective bearing,” *Mech. Syst. Signal Process.*, vol. 25, no. 1, pp. 266–284, Jan. 2011, doi: 10.1016/j.ymssp.2010.06.010.

[204] N. Tandon and A. Choudhury, “A review of vibration and acoustic measurement methods for the detection of defects in rolling element bearings,” *Tribol. Int.*, vol. 32,

no. 8, pp. 469–480, Aug. 1999, doi: 10.1016/S0301-679X(99)00077-8.

[205] P. Feng, P. Borghesani, H. Chang, W. A. Smith, R. B. Randall, and Z. Peng, "Monitoring gear surface degradation using cyclostationarity of acoustic emission," *Mech. Syst. Signal Process.*, vol. 131, pp. 199–221, Sep. 2019, doi: 10.1016/j.ymssp.2019.05.055.